THE APPLICATION OF HIGH-RESOLUTION LIDAR DEM DATA TO LANDSCAPE EVOLUTION: AN EXAMPLE FROM THE FUNDY BASIN, NOVA SCOTIA, CANADA

by

Tim L. Webster

Submitted in partial fulfillment of the requirements
For the degree of

Doctor of Philosophy

Dalhousie University
Halifax, NS
November 2005

DALHOUSIE UNIVERSITY

DEPARTMENT OF EARTH SCIENCES

The undersigned hereby certify that they have read and recommend to the Faculty of Graduate Studies for acceptance a thesis entitled "THE APPLICATION OF HIGH-RESOLUTION LIDAR DEM DATA TO LANDSCAPE EVOLUTION: AN EXAMPLE FROM THE FUNDY BASIN, NOVA SCOTIA, CANADA" by Tim L. Webster in partial fulfillment of the requirements for the degree of Doctor of Philosophy.

Dated: November 25, 2005

Supervisor: ______________________________

Readers: ______________________________

____

____

____

DALHOUSIE UNIVERSITY

DATE: November 25, 2005

AUTHOR: Tim L. Webster

TITLE: THE APPLICATION OF HIGH-RESOLUTION LIDAR DEM DATA TO LANDSCAPE EVOLUTION: AN EXAMPLE FROM THE FUNDY BASIN, NOVA SCOTIA, CANADA

DEPARTMENT OR SCHOOL: Department of Earth Sciences

DEGREE: Ph.D. CONVOCATION: May YEAR: 2006

Permission is herewith granted to Dalhousie University to circulate and to have copied for non-commercial purposes, at its discretion, the above title upon the request of individuals or institutions.

Signature of Author

The author reserves other publication rights, and neither the thesis nor extensive extracts from it be printed or otherwise reproduced without the author's written permission.

The author attests that permission has been obtained for the use of any copyrighted material appearing in the thesis (other than the brief excerpts requiring only proper acknowledgement in scholarly writing), and that all such use is clearly acknowledged.

Distribution License

DalSpace requires agreement to this non-exclusive distribution license before your item can appear on DalSpace.

NON-EXCLUSIVE DISTRIBUTION LICENSE

You (the author(s) or copyright owner) grant to Dalhousie University the non-exclusive right to reproduce and distribute your submission worldwide in any medium.

You agree that Dalhousie University may, without changing the content, reformat the submission for the purpose of preservation.

You also agree that Dalhousie University may keep more than one copy of this submission for purposes of security, back-up and preservation.

You agree that the submission is your original work, and that you have the right to grant the rights contained in this license. You also agree that your submission does not, to the best of your knowledge, infringe upon anyone's copyright.

If the submission contains material for which you do not hold copyright, you agree that you have obtained the unrestricted permission of the copyright owner to grant Dalhousie University the rights required by this license, and that such third-party owned material is clearly identified and acknowledged within the text or content of the submission.

If the submission is based upon work that has been sponsored or supported by an agency or organization other than Dalhousie University, you assert that you have fulfilled any right of review or other obligations required by such contract or agreement.

Dalhousie University will clearly identify your name(s) as the author(s) or owner(s) of the submission, and will not make any alteration to the content of the files that you have submitted.

If you have questions regarding this license please contact the repository manager at dalspace@dal.ca.

Grant the distribution license by signing and dating below.

Name of signatory

Date

DEDICATION

This thesis is dedicated to the most important people in my life, my family. I dedicate this work to my wife, Angela Templin, who has supported me in all of my academic pursuits, and to my children Christopher and Lauren who have heard their father say many times during the last 5 years “we will do that when the PhD is finished”.

TABLE OF CONTENTS

LIST OF TABLES

LIST OF FIGURES

ABSTRACT

High-resolution laser altimetry (LIDAR) is applied to geological problems such as bedrock and surficial mapping and local surface processes in the Fundy Basin of Nova Scotia. Two GIS-based validation methods were developed to compare points and derived "bald earth" DEM from two LIDAR acquisition methods with checkpoints from GPS and traditional surveys. A systematic height error between flight lines for one of the LIDAR acquisition methods was detected that related to the calibration procedures used in the survey. As a result, an area of 350 km^2 is the focus of this thesis where DEM errors are less than 0.2 m (1σ) in open areas and less than 1.3 m (1σ) in densely vegetated terrain.

Subtle topographical differences among three flow units of the Jurassic North Mountain Basalt (NMB) are clearly visible on a LIDAR DEM. Boundaries between flow units extracted from the DEM were verified by field mapping. The variable resistance of the flow units to erosion, documented by shatterbox experiments and down-core fracture density data, has a measurable control on incision by post-glacial consequent streams. Several ring structures in the lower flow unit, distinguishable only in the LIDAR data, are interpreted to be the remnants of rootless phreatomagmatic cones. Two new sets of surficial landforms have been identified that indicate ice was directed northwestward into the Bay of Fundy during the late stages of glaciation depositing a blanket of till over half of the catchments draining the NMB into the bay. In catchments where till cover is thick, greater surface run-off and weaker infiltration increases incision by as much as 43% for a given flow unit. Till cover therefore is expected to impede the achievement of steady state conditions and may also delay the onset of stream power law relationships in larger catchments until till cover has been effectively stripped. This thesis demonstrates through a range of examples that the high-precision and resolution of LIDAR can improve our understanding of how landscapes form and evolve.

ACKNOWLEDGMENTS

I would like to thank my family for their support, understanding, and sacrifices they have made to allow this degree and thesis to be completed. I would also like to thank my supervisory committee for whom I have great respect and from whom I have learned much. Thanks to Brendan Murphy, my supervisor, who has assisted me greatly in scientific writing and financial support and in all aspects of the project, especially the bedrock components. Thanks to John Gosse who guided me through my studies at Dalhousie and introduced me to quantitative geomorphology utilizing elevation models and who has taught me to get to the scientific point in writing and not make it boring. To Ian Spooner who assisted me in understanding the glacial history and geomorphology of the region and related aspects of the thesis. I would like to thank Bob Maher, David Colville, and the staff and students at the Applied Geomatics Research Group for all their support and assistance during this study, and David Woolnough and Paul LaFlesche for the NSCC financial assistance during the first 2 years of the degree. Dan Kontak and Ralph Stea of the N.S. Department of Natural Resources for discussions and field trips in the study area. Cliff Stanley and Rob Raeside of Acadia University for access to drill core and computer facilities and John Greenough of University of Okanagan University for providing reprints and geochemical data on the North Mountain.

CHAPTER 1. INTRODUCTION

1.1. INTRODUCTION

This thesis is written as a series of individual manuscripts that have been submitted to different peer reviewed journals. At the time of writing, chapter 2 has been accepted for publication in GeoCarto International, chapter 3 has been accepted for publication in Computers & Geoscience, chapter 4 has been accepted for publication in the Canadian Journal of Earth Sciences, chapter 5 is intended to be submitted to Geomorphology, and new research presented in sections of chapter 6 along with a synthesis of the rest of the thesis has been incorporated into a manuscript that is under review in the Canadian Journal of Remote Sensing. Chapters 2-5 therefore are four separate manuscripts, each with their own introduction and conclusion. The result of this approach is some repetition between the chapters. For example, the LIDAR (laser altimetry) system specifics and geology of the study area are described in each manuscript at a level appropriate for that paper. Chapter 6 represents some sections of new research and the conclusions of the thesis.

Landscapes are influenced by several factors including geology, climate, glaciations, and vegetation cover, among others. Our understanding of landscape formation and evolution is hampered in forested areas by the resolution and precision of topographic maps that earth scientists rely on in order to quantify the morphometry of a region.

Digital elevation models (DEMs) derived from aerial photography or other remote sensing systems such as the Shuttle Radar Topography Mission (SRTM) have degraded accuracies in forested areas and have resolutions of ca. 20 – 30 m. LIDAR – Light Detection and Ranging - is a remote sensing technique to precisely measure the earth's topography at high-resolutions compared to traditional methods. The narrow divergence of the laser beam employed with LIDAR allows penetration of the forest canopy and allows "bald earth" DEM resolutions of 2 – 4 m or better with 15 cm vertical precision to be constructed. The ability to remove the noise of the forest and land cover from the terrain offers the potential for more detailed geomorphic investigations than previously possible with traditional DEMs derived from aerial photography.

The hypothesis tested in this thesis is that the enhanced precision and resolution of LIDAR translates into improved knowledge of landscape formation and evolution. The objective of this thesis is to investigate DEMs derived from LIDAR and conventional methods in a forested region to understand how the landscape formed and what surface processes have influenced its evolution. Through this process the potential benefits of LIDAR for improving our understanding of landscape formation and evolution are evaluated.

Many landscapes within the Appalachians are forest covered and are characterized by ridge-and-valley physiography, with the central and northern regions having the added complications of glaciation (Randall et al., 1988). These landscapes have evolved over millennia and have been overprinted in some instances by multiple glaciations that manifest themselves in subtle landforms that are commonly obscured by the forest. In addition to these problems inland, coastal landscapes have been modified by post-glacial fluctuations in sea level which are not well constrained. To meet the objectives of this thesis, Geographic Information System (GIS) and image processing software have been used to manipulate LIDAR data for a region in the Fundy Basin of Nova Scotia, Canada in order to examine landscape evolution processes.

The Annapolis Valley region is within the Fundy Basin and was selected for this study for the following reasons: (1) it represents the typical ridge-and-valley terrain of the northeastern Appalachians that is underlain by a variety of rock types (Randall et al., 1988), (2) it occurs at an ice margin and has a complicated glacial history of multiple ice flows that have overprinted the landscape (Stea et al., 1998), (3) the landscape has experienced the same changes in base level, and (4) high-resolution LIDAR surveys have been conducted in the region and the data are available.

The Nova Scotia Community College (NSCC) was funded under a Canadian Foundation for Innovation grant to acquire high-resolution elevation data along the coastal zone of the Bay of Fundy (Figure 1.1). As a result of this grant, the NSCC established the Applied Geomatics Research Group (AGRG) which acquired the LIDAR data and have made it available along with access to computer hardware and geomatics software for the analysis of these data.

A LIDAR system is comprised of three components: (1) a laser ranging unit to determine the range to the target from the aircraft, (2) a high-precision GPS to map the trajectory of the aircraft, and (3) an inertial measurement unit (IMU) to record the trajectory and attitude of the aircraft. The LIDAR is mounted in an aircraft and the laser fires thousands of shots per second that are directed across a swath toward the earth's surface by an oscillating mirror. The laser pulses are reflected back to the sensor, which records the two-way travel time that is converted into a range distance based on the speed of light and combined with the angular and trajectory data from the scan mirror, GPS, and IMU to determine the position of the targets in space. LIDAR surveys are typically acquired in swaths along overlapping flight lines or strips. The results of a LIDAR survey are a set of high-density points known as a 'point cloud' that represent the ground and other targets, such as vegetation or anthropogenic features e.g. roads, buildings, bridges. The LIDAR point cloud is classified into 'ground' or 'non-ground' features using specialized software. The classified points for each strip are merged together and output as a series of tiles based on a map projection grid system. The two sets of LIDAR points are integrated into a GIS that can be used to interpolate different types of surfaces from the combination of 'ground' and 'non-ground' points. Of specific interest in geomorphic applications, a "bald earth" DEM can be constructed from the LIDAR 'ground' points, at a high spatial resolution ca. 2-4 m. Using only the 'ground' points effectively removes the vegetation and other land cover features (e.g. buildings) from the terrain.

The manipulation of LIDAR DEMs in a GIS allows for the construction of maps that can preferentially highlight subtle geomorphic features (e.g. artificial sun illumination and vertical exaggeration). Such features are often not readily observed in traditional DEMs, or from stereoscopic inspection of aerial photographs, because of their low relief and obstructions from vegetation. Because of the scale of the many geological features being studied, regional-scale LIDAR surveys are required in order to assess its applicability to geomorphic research, such that features with a topographic expression can be detected and traced over long distances.

Although the effect of DEM resolution on measuring different hydrologic and geomorphic properties has been examined (e.g. Wolock and Price, 1994; Zhang and Montgomery, 1994; Goa, 1997; Zang et al., 1999; Walker and Willgoose, 1999), most of these studies focussed on the effects of different grid cell size interpolated from similar source data. This study is different in that its focuses on enhanced DEM resolution and precision as a result of advances in laser altimetry data acquisition technology.

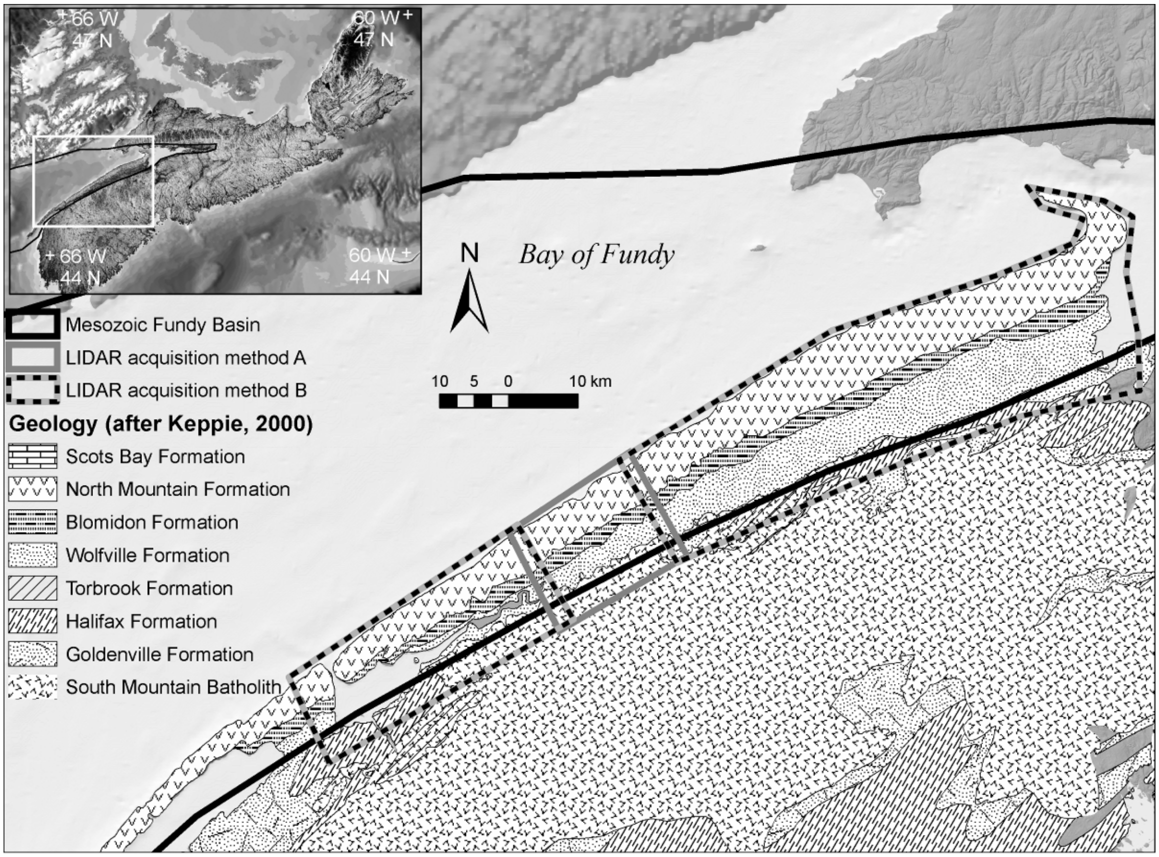

Figure 1.1 Geological map of the study area. Inset map in the upper left shows the extent of the Fundy Basin (heavy black line) in Maritime Canada and the location of the geology map. Geological boundaries (after Keppie, 2000) with the Fundy Basin (heavy black line) with the extent of the LIDAR coverage from the two acquisition methods (solid and dashed grey lines).

LIDAR has been used in a limited number of geoscience applications, including the analysis of river networks (Stock et al., 2005), the generation of cross-sections across rivers (Charlton et al., 2003), in general glaciology (Krabill et al., 1995, 2000; Abdalati and Krabill, 1999), groundwater monitoring (Harding and Berghoff, 2000), investigation of landslides (McKean and Roering, 2003), and in the mapping of tectonic fault scarps and geomorphic features (Haugerud et al., 2003).

In this study, the application of high-resolution LIDAR for geomorphology is separated into four categories: (1) LIDAR height validation (chapters 2 and 3), (2) mapping bedrock contacts and structures (chapter 4), (3) mapping surficial cover and related landforms (chapters 4 and 5), and (4) deriving the morphometry of erosional landforms including streams and catchment basins (chapter 5). Taken together, the overall results demonstrate the usefulness of LIDAR in improving our understanding of landscape form and evolution (chapter 6).

1.2. LIDAR STUDY AREA: BEDROCK AND SURFICIAL GEOLOGY

The study area is located within the Annapolis Valley region of Nova Scotia, Canada and is part of the Mesozoic Fundy Basin. The LIDAR data cover over 2500 km^2 of the basin and include the basin’s three physiographic features; the North Mountain, South Mountain and the intervening Annapolis Valley. The Annapolis Valley is predominantly underlain by Triassic sedimentary rocks (Blomidon and Wolfville formations), flanked by the Jurassic North Mountain Basalt (NMB) to the north and Devonian South Mountain Batholith to the south (Keppie, 2000; MacDonald and Ham, 1994) (Figure 1.1).

The NMB represents the northernmost extent of the Central Atlantic Magmatic Province (CAMP) that is characterized by predominantly tholeiitic basaltic magmatism erupted during the early stages of the rifting that eventually led to the opening of the Atlantic Ocean and the formation of a passive margin (Marzoli et al., 1999). The NMB dips gently to the northwest, forms the southeast limb of a regional syncline (Withjack et al., 1995), and is crosscut by north to northeast-trending faults and fractures that exhibit dextral displacement (Olsen and Schlische, 1990; Schlische and Ackermann, 1995). Hudgins (1960) identified several individual lava flows that extend along most of the length of the NMB and Kontak (2001) defined three dominant flow units. The lower flow unit (LFU) forms the cuesta of the valley and consists of a thick (40 - 150 m) massive single flow that is columnar jointed. The middle flow unit (MFU) conformably overlies the LFU, and consists of multiple thin flows that are highly vesicular and amygdaloidal. Zeolites are most common in the MFU of the NMB where they occur as amygdules and also in veins, pipes and "bubble trains" (Kontak, 1999; Pe-Piper, 2000). The upper flow unit (UFU) conformably overlies the MFU and outcrops along the shore, and consists of 1-2 massive flows. The Scots Bay Formation overlies the NMB, consists of lacustrine deposits and is exposed only in the northeast of the study area (Wade et al., 1996).

The South Mountain forms the southern margin of the Annapolis Valley and is underlain by ca. 370 Ma granitoid rocks of the South Mountain Batholith (SMB) and by the Cambrian-Ordovician Meguma Supergroup (Keppie, 2000; MacDonald and Ham, 1994). The LIDAR data coverage extends onto the South Mountain margin of the Annapolis Valley but does not include the full extent of significant watersheds draining this area (Figure 1.1).

The study area lies at the margin of the Wisconsinan Laurentide ice sheet and has been affected by repeated episodes of glaciation until ca. 12 ka (Stea and Mott, 1998). The earliest ice flows were eastward and southeastward from an Appalachian or Laurentide ice source (Stea et al., 1998). NMB erratics were transported southeastward up to 120 km to the Atlantic Coast (Stea et al., 1992; Lewis et al., 1998). The second major ice-flow was southward and southwestward from the Escuminac Ice Centre in the Prince Edward Island (PEI) region and is recorded by southward-trending striae crossing earlier southeastward-trending striae (Stea et al., 1998). The Carboniferous red beds of PEI were eroded and transported southward and deposited in the Lawrencetown Till. Ice then flowed northwestward and southward from the Scotian Ice Divide across the axis of Nova Scotia (Stea et al., 1998). Locally ice flowed from the Scotian Divide northwestward over the NMB into the Bay of Fundy. With the late-glacial rise of relative sea level, ice margins were probably destabilized, with ice flow increasingly directed into the Bay of Fundy to merge with southwestward ice streams from New Brunswick (Stea et al., 1998). Locally, ice flowed westward from the eastern end of the Annapolis Valley (Lewis et al., 1998; Stea and Mott, 1998). The relative sea level (RSL) history of the region is complicated and varies spatially along the Bay of Fundy. Raised beaches and deltas dated at 14 to 12 ka occur along the shoreline of the bay (Stea and Mott, 1998).

1.3. LIDAR ACQUISITION AND GEOMORPHIC APPLICATIONS INVESTIGATED

Two different acquisition methods using two different LIDAR systems were used to acquire data for the study area in the summer of 2000 (Figure 1.1). Independent validation of the data using GPS and traditional surveying methods was done in order to ensure the data met the specifications and to characterize the standard error. The validation process showed that only one set of LIDAR data met the specifications, covering a surface area of 350 km^2. As a result, this area is the focus of the geomorphic investigation in this thesis (Method A, Figure 1.1). Of this area, the North Mountain is the focus of the analysis of the LIDAR data in order to assess the following geomorphic problems.

(1) The sensitivity of high-resolution LIDAR to the determination of geological contacts is investigated. Topographic expression of geological contacts is most readily seen in regions of contrasting bedrock types where the contacts are steep. The North Mountain study area, however, is underlain by one dominant rock type and is shallowly dipping. Nevertheless, even in this unfavorable scenario, LIDAR DEM, combined with field investigations can precisely constrain the location of geological contacts between flow units. Although Kontak (2001) subdivided the NMB into three flow units (lower, middle, upper) they had not been systematically mapped in this area. The location and extent of the flow units are important for economic and environmental issues (MFU – has zeolites deposits of potential economic grade, and the UFU and LFU are aggregate

resources). Subtle landforms within the flow units can be extracted from the LIDAR based on their topographic expressions. These include individual flows of the MFU and a linear sequence of craters that occur within the LFU.

(2) In glaciated terrains such as this region of the Fundy Basin, unconsolidated sediments commonly mask bedrock features. Since LIDAR systems measure surface topography, their applicability in mapping surficial deposits and glacial landforms is an important part of this study. The terrain roughness and texture observed on the LIDAR DEM can be used to determine areas of thick and thin till cover. The surficial geology of the area had recently been mapped using traditional methods of interpreting landforms from aerial photography by Stea and Kennedy (1998) and provides an opportunity to test if new landforms can be identified using high-resolution LIDAR.

(3) The relationship between stream incision and rock-uplift, climate, base level changes, and bedrock resistance to erosion is important to understand landscape evolution. The resolution of the LIDAR allows the terrain to be examined at a sufficiently small scale to isolate individual factors (e.g. bedrock resistance to erosion) that may control incision. In this region, the streams incise into a single bedrock formation tilted towards the bay and have all experienced the same changes in base level. The LIDAR data are used to calculate stream incision depth curves that are related to the different flow units of the NMB. These flow units have different physical and chemical characteristics that affect their resistance to erosion as confirmed in the laboratory. More generally, the relationship between bedrock resistance to erosion and stream incision is relevant to our basic understanding of how streams erode and landscapes evolve.

(4) Catchments are the spatial domains at which many surface and ecological processes operate. The accuracy of catchment basin boundaries derived using automated GIS routines is dependent on the quality of the DEM data. The high-resolution and precision of LIDAR provides an opportunity to construct a more precise DEM, enabling a potentially more accurate definition of catchment basins and a more detailed examination of surface processes. The resolution of the LIDAR highlights the anthropogenic influences on the surface drainage characteristics and modifications to the DEM are required to accurately construct catchment boundaries. The catchments examined in this study draining off the NMB into the bay are entirely within the LIDAR coverage thus allowing basin morphometry to be determined. Differences in morphometry of these catchments are compared to variations in till cover thickness and bedrock geology to determine their influence on landscape evolution.

(5) The effects of glacial till cover on surface-groundwater interaction have important implications for stream discharge which influences surface processes and water resources. The catchments draining NMB in this study consist of thin till covering scoured bedrock in the west and a thicker till cover (ca. 5 m) in the east. This provides an opportunity to determine the effects of till cover on fluvial processes by measuring the surface-groundwater interaction between catchments with contrasting till thickness. In this study, stream discharge and water chemistry were measured from two catchments with contrasting till thickness.

1.4. METHODOLOGY

Prior to applying the LIDAR data to geomorphic investigations, the accuracy of the LIDAR data was investigated using a combination of GIS processing, field GPS and traditional surveying of height validation data. This allowed the errors associated with these data to be characterized in open areas and under the forest canopy. The LIDAR data were further processed in a GIS and maps were constructed that were interpreted for bedrock contacts and landforms. After validation and interpretation of the LIDAR maps, field mapping of bedrock and surficial deposits was followed by bedrock sampling for geochemical, petrographic, and microprobe analysis. Laboratory experiments were conducted to measure the resistance to abrasion of the different NMB flow units. Instrumentation of streams allowed the measurement of discharge and determination of water chemistry parameters in catchments with contrasting thickness of till cover. These data were compared to basin and stream morphometry determine from the LIDAR DEM.

All geospatial data were integrated into a common database utilizing the ESRI suite of ArcGIS™ software. Surfaces, such as the DEM using the ‘ground’ LIDAR points and a Digital Surface Model (DSM) using all of the LIDAR points (including those representing vegetation), were constructed using the interpolation routines available within the ArcGIS™ software. PCI Geomatica™ software was used for enhancement and visualizing the LIDAR surfaces.

GPS validation data were acquired using dual frequency survey grade Leica receivers, and a Leica total station was used for validation data collection under the forest canopy. An accuracy assessment of the error of the LIDAR DEM was conducted in order to quantify the error associated with geological process rates inferred from these data. A Trimble™ code-based GPS receiver was used for positioning during the geological mapping fieldwork. A combination of Rivertools™ and PCI Geomatica™ software was used to extract the morphometric parameters from the drainage basins and stream longitudinal profiles. Colour-shaded relief and other maps were constructed from the LIDAR surfaces and other traditional DEMs including those derived from 1:10,000 (province of Nova Scotia), 1:50,000 and 1:250,000 (Natural Resources Canada, CDED – Canadian Digital Elevation Data) scale contours using the PCI Geomatica™ software.

Bedrock samples of the NMB were characterized petrographically and geochemically. Major and selected trace elements were analyzed by X-Ray Fluorescence at the Nova Scotia Regional Geochemical Centre at St. Mary's University. Representative minerals were analyzed with an electron microprobe at Dalhousie University using a JOEL 733 Superprobe.

Bedrock resistance to erosion by abrasion was investigated using a shatterbox consisting of a cylindrical container that holds a central disk and an outer ring at Dalhousie University. Drill core of the NMB (GAV-77-3) located at the Geology Department in Acadia University was used to quantify the fracture density and the distribution of vesicles and zeolite-bearing amygdules of the NMB flow units.

In order to assess the influence of glacial till on hydrologic processes Hydrolab datasonde™ water chemistry sensors and Level Logger™ pressure transducers were supplied by the AGRG and deployed near the outlet of two catchments with contrasting till cover thickness to measure stream discharge and water chemistry parameters.

Campbell Scientific meteorological stations operated by the AGRG were used to measure precipitation events and related to the stream discharge and water chemistry data.

1.5. THESIS LAYOUT

Chapters 2-5 consist of manuscripts that have been submitted for publication in refereed journals and copyright permission has been granted to those accepted for publication (Appendix 1). Chapters 2 and 3 deal with the height validation, accuracy and limitations of the data, and therefore underpin the interpretations derived from those data presented in chapters 4 and 5. Although there is some overlap between the chapters 2 and 3, the validation approaches and results from both complement one another. Chapter 2 focuses on (i) the comparison between the two LIDAR acquisition methods and (ii) the comparison between the interpolated DEM surface and the validation checkpoints for the acquisition method that met the specifications. The results of using both validation approaches are presented, and highlight the benefits of using both approaches to determine LIDAR classification errors. This chapter is broad in scope and discusses issues related to different LIDAR acquisition methods as they relate to the sensor, local terrain, land cover, climate, and ground conditions.

Chapter 3 presents a rigorous discussion of the error between LIDAR strips or flight lines. Validation methods and errors between adjacent strips or flight lines of LIDAR data are discussed. The validation approach compares the LIDAR points with checkpoints using an automated GIS procedure that is written in the Arc Macro Language (AML) and is designed for use within the Arc/Info GIS environment. The detail on the various input and output GIS files and associated tables that are used to determine the summary error statistics associated with the LIDAR point data are described. Data from the two LIDAR acquisition methods are used to show how the systematic errors between adjacent flight lines or strips can be determined. The accuracy of the LIDAR ground points under the vegetation canopy for the region in the vicinity of the NMB circular structures (see chapter 2) provides complementary information on some of the errors that can occur within these data. It was determined that a systematic range error between strips was present in the LIDAR data derived using one of the acquisition methods. The cause of this error is identified to be related to the calibration procedures used during the survey, and the general implications of this conclusion to LIDAR-based geomorphic studies are discussed.

After the validation analysis, specific geomorphic applications (chapters 4 and 5) were restricted to the aerial extent of the LIDAR data (350 km^2) that met the accuracy specifications. In order to effectively use the LIDAR DEM to study surface processes associated with landscape evolution, details on the bedrock lithologies are required. Although other studies have subdivided the basalt into three flow units (LFU, MFU, and UFU) in the field, they had not been systematically mapped in the study area. In chapter 4, the sensitivity of high spatial resolution and vertical precision of the LIDAR DEM in constraining geological contacts between map units is tested by combining LIDAR DEM with field investigations. The relief of the contact between units is measured by GPS and compared to the LIDAR and conventional DEMs. The combined approach (LIDAR and field mapping) enabled the mapping of the flow units, and several new circular “ring” structures were identified in the LFU. Petrographic analysis of samples collected adjacent to and within the rings reveal that the topographic highs forming the rings are comprised of quenched melt. A model is proposed for their origin that involves the development of “rootless cones” formed as a result of phreatomagmatic explosions as the lava interacted with surface water or saturated sediments. Chapter 4 summarizes the basalt flow unit mapping and the analysis and model for the development of these ring structures. More generally, this study shows that high resolution LIDAR and field mapping can assist mapping of geologic contacts, even in regions underlain by shallowly dipping strata of similar bedrock.

The bedrock map deduced in Chapter 4 allows a detailed study of the morphometry of the catchment basins and stream incision as they relate to the flow units. Chapter 5 summarizes the analysis of the LIDAR DEM for fluvial and glacial erosion surface processes. Catchment basins and stream longitudinal profiles are extracted from the LIDAR DEM. Stream incision depths are calculated and related to the variable resistance to erosion of the basalt flow units. Variations in till thickness of the catchments are related to the basin morphometry. The hypsometries of catchments underlain by scoured bedrock and underlain by till blanket are computed and indicate that the respective basins are quantifiably different. The effect of glacial till on fluvial processes is investigated by comparing stream discharge and water chemistry parameters between two catchments with contrasting till thickness and related to the variations in catchment’s morphometry.

Chapter 6 is a combination of new analysis and the conclusions of the thesis. The new material includes an analysis of error of different DEM grid cell sizes, stream profile and cross section validation, a new method for visualizing the terrain utilizing principal component analysis, and the identification of additional wave-cut terrace profiles along the coast. A composite image from the principal components of multiple shaded relief maps derived from the LIDAR DEM is presented in order to highlight topographic features regardless of their orientation. New landforms associated with local ice dynamics of the area are identified. Stream profile and cross section elevations obtained from LIDAR are validated by comparison with a total station survey and identify overhanging vegetation as a problem. The characterization of the error associated with LIDAR DEMs for variable land cover is summarized. Several terraces along the shoreline have been extracted and compared to previously published elevations. The LIDAR enables more terraces to be extracted and traced along the shore revealing patterns of variable relative sea level (RSL) change. The chapter concludes with a list of contribution to knowledge that the analysis of high-resolution LIDAR has provided. With these improvements to mapping, our understanding of processes controlling landscape development will be advanced in different environments in similar ways as we have demonstrated in this study.

1.6. MANUSCRIPT CONTRIBUTIONS

The following section describes the chapters that represent submitted manuscripts and includes a discussion of the contributions of the various co-authors for each manuscript.

1.6.1. “Chapter 2 LIDAR VALIDATION USING GIS: A CASE STUDY COMPARISON BETWEEN TWO LIDAR COLLECTION METHODS”

T.L. Webster authored, "LIDAR VALIDATION USING GIS: A CASE STUDY COMPARISON BETWEEN TWO LIDAR COLLECTION METHODS", which was submitted to GeoCarto International and accepted with minor revisions. The revised manuscript was accepted for publication on July 6, 2005 and a letter of permission to include the copyright material in this thesis has been signed by the director of Geocarto International and is included in the appendix of the thesis. The readership of this journal consists dominantly of GIS and remote sensing specialists from all fields including the earth sciences. T.L. Webster did the analysis associated with this work; he used and interpreted data that were acquired with the assistance of staff and students from the Applied Geomatics Research Group that have been acknowledged in the manuscript.

1.6.2. "Chapter 3 AN AUTOMATED GIS PROCEDURE FOR COMPARING GPS AND PROXIMAL LIDAR GROUND ELEVATIONS"

T.L. Webster and G. Dias co-authored "AN AUTOMATED GIS PROCEDURE FOR COMPARING GPS AND PROXIMAL LIDAR GROUND ELEVATIONS" was submitted to Computers & Geoscience. The manuscript was peer reviewed and required revisions. The revised manuscript was accepted for publication on August 30, 2005 and a letter of permission to include the copyright material in this thesis has been signed by the editor of Computers & Geoscience and is included in the appendix of the thesis. The readership of this journal are earth scientists who apply computer technology including GIS and remote sensing to solve geological problems.

The manuscript describes an automated routine written in the Arc Macro Language (AML) that is executed within the Arc/Info GIS environment to validate LIDAR points using GPS and traditional survey points. The computer code introduced in the paper is available for download from that journal's ftp site (HTTP://WWW.IAMG.ORG/CGEDITOR/INDEX.HTM).

T.L. Webster was the originator of the GIS procedure concept and statistical calculation requirements and G. Dias, an Applied Geomatics Research Group (AGRG) student at the time, wrote the majority of the AML computer code to implement the concept. T.L. Webster did the analysis of the LIDAR data using the two LIDAR acquisition methods. The validation data that were used in the analysis were acquired with the assistance of staff and students from the AGRG that have been acknowledged in the manuscript.

1.6.3. "Chapter 4 MAPPING SUBTLE STRUCTURES WITH LIDAR: FLOW UNITS AND PHREATOMAGMATIC ROOTLESS CONES IN THE NORTH MOUNTAIN BASALT, NOVA SCOTIA"

T.L. Webster, J.B. Murphy, and J.C. Gosse co-authored the manuscript entitled "MAPPING SUBTLE STRUCTURES WITH LIDAR: FLOW UNITS AND PHREATOMAGMATIC ROOTLESS CONES IN THE NORTH MOUNTAIN BASALT, NOVA SCOTIA" that was submitted to the Canadian Journal of Earth Sciences. The manuscript has been accepted subject to minor revisions. The revised manuscript was accepted for publication on September 29, 2005.

T.L. Webster did the LIDAR DEM analysis and fieldwork related to the flow unit mapping and ring structure sampling. T.L. Webster was the originator of the conceptual model for the ring structures. J.B. Murphy gave advice and assisted in the interpretation of the petrographic and geochemical analysis. J.B. Murphy and J.C. Gosse gave advice on the ring structure model and revising the manuscript.

1.6.4. "Chapter 5 MEDIUM-SCALE (5 KM^2) FLUVIAL MORPHOMETRIC ANALYSIS IN A GLACIATED TERRAIN"

T.L. Webster, J.C. Gosse, I. Spooner, and J.B. Murphy co-authored the manuscript entitled "MEDIUM-SCALE (5 KM^2) FLUVIAL MORPHOMETRIC ANALYSIS IN A GLACIATED TERRAIN", which is to be submitted to Geomorphology after the thesis review and defence.

T.L. Webster did the LIDAR DEM analysis and fieldwork related mapping the bedrock and surficial materials. T.L. Webster did the fieldwork and calculations associated with measuring the stream discharge and water chemistry measurements in addition to the measurements of the drill core and shatterbox experiments. J.C. Gosse gave advice on the stream incision and basin morphometry work and the provided some useful references on topography and fractals and directed the focus of the initial manuscript and revisions. I. Spooner gave advice related to the possible effects the glacial till cover could have on the fluvial processes and the glacial history of the area and revising the manuscript. J.B. Murphy supplied some useful references related to hypsometry and gave general advice on the project and revisions to the manuscript.

1.6.5. "Chapter 6 SUMMARY AND CONCLUSIONS"

The new analysis that is presented in chapter 6 has been incorporated into a synthesis manuscript summarizing the thesis, not included as a chapter because of the redundant material in the synthesis. T.L. Webster, J.B. Murphy, J.C. Gosse, and I. Spooner co-authored the manuscript entitled "COUPLING LIDAR-DERIVED LANDSCAPE METRICS AND SURFACE PROCESSES: AN EXAMPLE FROM THE FUNDY BASIN, NOVA SCOTIA, CANADA" that was submitted to the Canadian Journal of Remote Sensing on September 29, 2005. This paper was submitted to a special issue of presentations during a special session on LIDAR at the 26th Canadian Remote Sensing Symposium held at Wolfville, Nova Scotia in June 2005.

T.L. Webster did the fieldwork to acquire the validation total station survey of the stream profile and cross sections with assistance of staff and students from the AGRG that have been acknowledged in the manuscript. T.L. Webster did all the analysis of the LIDAR DEM including the terrace profiles. J.B. Murphy, J.C. Gosse, and I. Spooner all contributed to the manuscript by suggesting organizational changes and improvements to the figures. This was especially true in order for sections of this manuscript to also serve as a summary and conclusions chapter in this thesis.

CHAPTER 2. LIDAR VALIDATION USING GIS: A CASE STUDY COMPARISON BETWEEN TWO LIDAR COLLECTION METHODS

Tim L. Webster

Department of Earth Sciences, Dalhousie University

and

Applied Geomatics Research Group

Centre Of Geographic Sciences, Nova Scotia Community College

50 Elliot Road, RR#1

Lawrencetown, NS, Canada, B0S 1M0

2.1. ABSTRACT

In the summer of 2000, the Annapolis Valley of Nova Scotia, Canada was selected for a high-resolution elevation survey utilizing LIDAR (Light Detection And Ranging). Two different LIDAR systems were used to acquire data for the area. The vertical accuracy specification for the survey called for heights to be within an average of 15 cm of measured GPS heights and 95% of the data to be within 30 cm. Prior to the application of these data to geoscientific problems, extensive validation procedures were employed. High precision GPS and traditional surveys were conducted to collect height validation checkpoints. Two validation methods were developed in a GIS environment that involved comparing the checkpoints to the original LIDAR points and to an interpolated “bald earth” DEM. A systematic height error between flight lines for one of the LIDAR methods was detected that related to the calibration procedures used in the survey. This study highlights the differences between laser systems, calibration and deployment methodologies and emphasizes the necessity for independent validation data.

2.2. INTRODUCTION

LIDAR (Light Detection and Ranging) has been used for engineering, flood risk mapping (Webster et al., 2004*a*, *b*) and its utility has been demonstrated in forestry (Maclean and Krabill, 1986), and glacier mass balance investigations (Krabill et al., 1995, 2000; Abdalati and Krabill, 1999). A general overview of airborne laser scanning technology and principles is provided by Flood and Gutelius (1997) and Wehr and Lohr (1999). Applications to coastal process studies in the USA have been reported by Sallenger et al. (1999), Brock et al. (2002), and Stockdon et al. (2002), among others. Preliminary trials in Atlantic Canada were reported by O'Reilly (2000) and subsequent studies were described by Webster et al. (2004*a*, *b*). Various studies have been reported on the calibration and systematic errors of LIDAR systems (Kilian et al., 1996; Filin, 2003*a*, *b*) and the accuracy of laser altimetry data (Huising and Gomes Pereira, 1998; Crombaghs et al., 2000; Maas, 2000, 2002,). Although LIDAR technology has steadily improved since the mid-1990s, these studies highlight the requirement for height validation.

This paper describes a recent study where two data acquisition companies operating two different LIDAR sensors were contracted to acquire data for a large region of variable relief and land cover (Figure 2.1). These LIDAR surveys provide an opportunity to compare two different acquisition methods using two different LIDAR systems. The vertical accuracy specification for the LIDAR surveys called for heights to be within an average of 15 cm of measured GPS heights and 95% of the data to be within 30 cm.

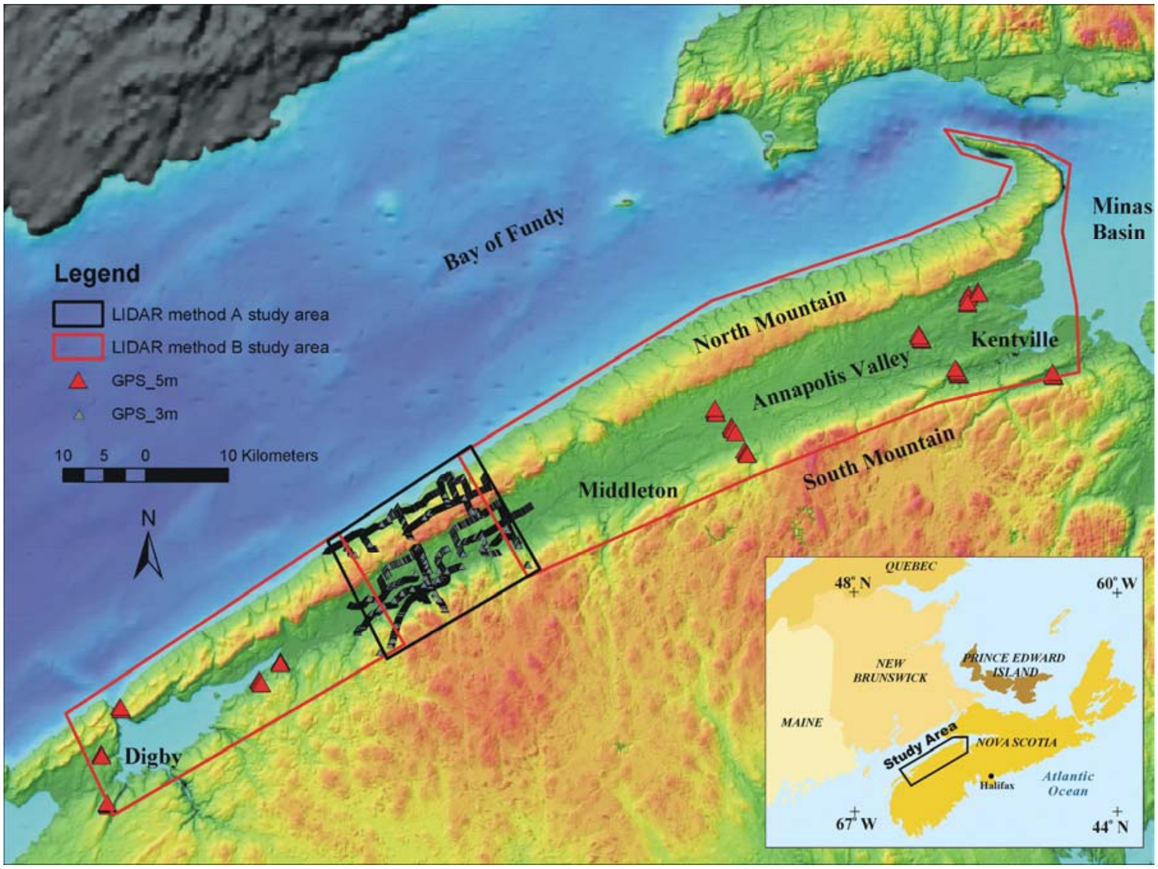

Figure 2.1 Colour shaded relief of 20 m DEM for the Annapolis Valley, Nova Scotia, highlighting the study areas of LIDAR acquisition methods A and B. The DEM colours range from sea level (blue) to 265 m (red). Vehicle mounted real time kinematic GPS measurements were used for study area A (grey triangles with black outlines) and static GPS measurements (red triangles) were used for study area B validation. The original 20 m DEM was produced by the Nova Scotia Geomatics Center, Service Nova Scotia & Municipal Relations. Location map inset in lower right shows the study area location in Maritime Canada.

The LIDAR data from the two methods and validation data were integrated into a GIS where two validation techniques were used for the analysis. The validation approaches for both LIDAR methods consisted of comparing checkpoints to both the original LIDAR points proximal to the checkpoints and to the derived “bald earth” DEM. The program code and details of the validation technique that compares the checkpoints to the proximal LIDAR points are described in detail elsewhere (see Webster and Dias, in press; Chapter 3) and are summarized here. The focus of this paper will be on the LIDAR acquisition, GIS processing, and validation methods and results of LIDAR data acquired from the two different methods.

The results indicate that one LIDAR method did not meet the specifications and had height discrepancies between flight lines as a result of a range bias that was related to the calibration procedures used. Although the other method met the specifications, LIDAR classification errors were identified that affected the validation results and the final DEM representation. This study demonstrates that differences in LIDAR systems and deployment methods yield different results that could affect geoscience interpretations, and implies that for any study, familiarity with the terrain, land cover, and climate is required in order to match the right LIDAR system to the right ground conditions. The requirement for independent validation data and the development of validation techniques in the GIS environment proved to be critical in determining the accuracy of the different systems and the occurrence of a systematic range bias for one of the LIDAR methods.

2.3. LIDAR ACQUISITION METHODS A AND B

The study area is located on the southeast shore of the Bay of Fundy of Maritime Canada and includes the North Mountain and the South Mountain that bound the Annapolis Valley (Figure 2.1). In addition to the acquisition of LIDAR, a variety of other remotely sensed data have been acquired and analyzed for this study area and are reported in Webster et al. (2004*b*). The land use of the valley floor consists of agriculture and urban, while the North and South Mountains are mainly covered with dense mixed coniferous and deciduous forest.

2.3.1. METHOD A SURVEY

For LIDAR acquisition method A, the study area consisted of 350 km^2 (Figure 2.1). An Optech ALTM1020 sensor mounted in a Navajo P31 twin-engine fixed-wing aircraft was used in the survey. The LIDAR operated at a 5000 Hz laser repetition rate along with the scanning mirror operating at 15 Hz to direct the laser pulses across the swath. The system used a near-infrared laser operating at 1047 nm and has a beam divergence of 0.25 mrad (Figure 2.2, A). The survey was conducted between July 6 and July 13, 2000 and consisted of 64 flight lines oriented parallel to the coast with two check lines running transverse to the coast. Since a “bald earth” DEM was one of the desired outcomes of the survey, the LIDAR unit was set to record the last return pulse. This increased the probability of getting a return from the ground or close to it in forested areas. The latest LIDAR sensors are capable of recording multiple returns, typically at least the first and last pulse with some sensors recording up to 4 intermediate returns, and in most cases can record the intensity of the reflected pulses (Toth, 2004).

2.3.2. METHOD B SURVEY

For LIDAR acquisition method B, the study area consisted of 2,217 km^2 (Figure 2.1). Unlike the Optech LIDAR system that combines the laser, GPS and IMU components into one package, this LIDAR system was originally designed for corridor data collection on a helicopter and was built from the individual components. The sensor was mounted on a pod that hung from a Bell Ranger 206 helicopter. The LIDAR operated at a 10,000 Hz laser repetition rate along with the scanning mirror operating at 15 Hz to direct the laser pulses across the swath. The mission was to be flown at an altitude of 900 m Above Ground Level (AGL), but due to an unforeseen reduction in laser power it was flown at 600 m AGL (Figure 2.2, B). The survey was conducted between July 11 and August 31, 2000. This LIDAR system was only capable of recording the first return pulse.

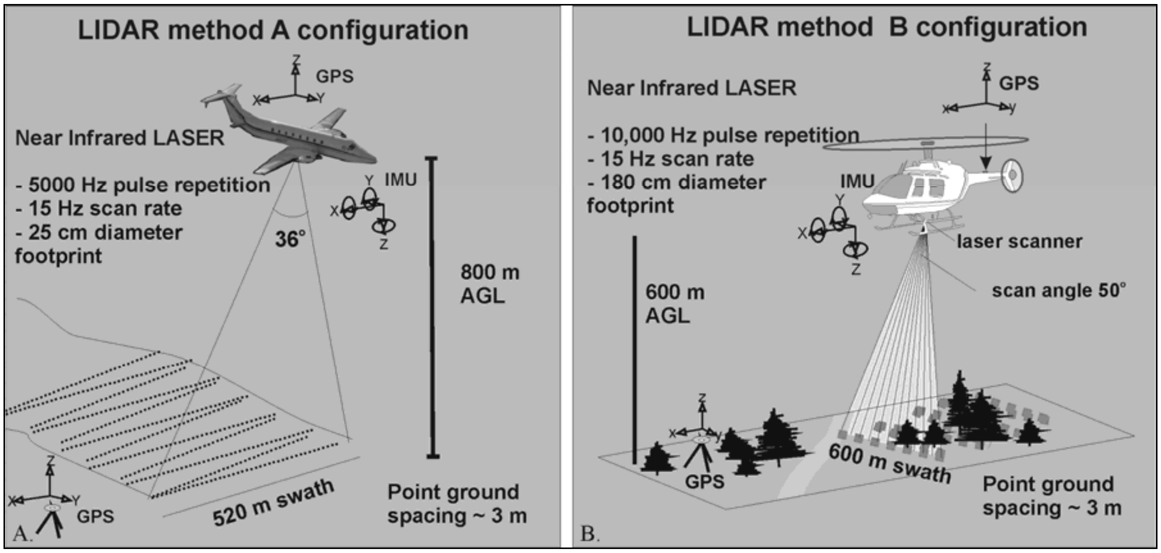

Figure 2.2 (A) LIDAR configuration for acquisition method A. (B) LIDAR configuration for LIDAR acquisition method B.

2.4. GIS PROCESSING AND LIDAR VALIDATION METHODS

In both acquisition methods A and B, the LIDAR data were delivered in ASCII files consisting of *x,y,z* data. The elevations were converted from ellipsoidal to orthometric heights above the geoid. In this case the HT_101 model supplied by the Canadian

Geodetic Survey of Natural Resources Canada was used to relate WGS84 ellipsoidal heights to Canadian Geodetic Vertical Datum of 1928 (CGVD28). In addition to these fields we also acquired the GPS time stamp for every LIDAR return. This gives the ability to examine the LIDAR data by GPS time or flight line. Each survey method involved classifying the LIDAR point cloud into ‘ground’ and ‘non-ground’ points. Currently there is no standard format for LIDAR data, however the American Society of Photogrammetric Engineering and Remote Sensing (ASPRS) recently published a proposed binary format that had several additional parameters such as scan angle for each LIDAR point (Schuckman, 2003).

The LIDAR points and ground validation points were imported into an Arc/Info GIS workstation running on a Unix platform. For LIDAR method A, each tile typically had in excess of 3 million points, of which over 1 million would typically be ‘ground’ points. A “bald earth” DEM was constructed from the ‘ground’ points of method A and used in part of the validation process. The 2 m resolution DEM was constructed by using a quintic (5th order polynomial) interpolation method from the triangular irregular network (TIN) of the ground points. Several other interpolation methods were investigated such as spline techniques, inverse distance weighting, and kriging, in addition to the TIN method. Because of the relative uniform density of the ground points, although much higher in open areas than in the forest, the TIN and quintic interpolation method was selected because it best represented the ground surface with the fewest artifacts.

For acquisition method B however, there was a distinct lack of LIDAR points over low to moderate reflective near-infrared targets such as asphalt and coniferous forest as a result of the power reduction, although LIDAR returns with a ground spacing of 3 m were available for cleared grass-covered areas. As a result of this, GPS collection concentrated on areas of grass fields where a dense coverage of LIDAR returns was guaranteed. The DEM constructed from the 'ground' points from method B was not used in the validation because of the unreliability of the surface as a result of the sparse data points in many areas.

The absolute accuracy of LIDAR data depends on the removal of the systemic errors associated with the system. Filin (2003*a*, *b*) provides an overview of the types and treatment for these sources of error in LIDAR systems. Kilian et al. (1996) described the methods of determining the local coordinates of LIDAR points by combining GPS, Inertial Measurement Unit (IMU), and the laser ranges, and measuring differences between strips. Maas (2000, 2002) improved this technique by implementing a method based on a Triangular Irregular Network (TIN) constructed from the LIDAR points for overlapping strips. Huising and Gomes Pereira (1998) reported on errors and accuracy of LIDAR data of the Netherlands collected by a variety of vendors using different systems. They observed height errors between strips that they attributed to GPS errors. Crombaghs et al. (2000) also observed errors near strip boundaries. Latypov and Zosse (2002) used overlapping strips to calibrate the parameters of the aircraft motion between strips, however ground control is required in order to perform a range calibration. These previous studies have dealt with relatively small study areas, compared to this study, and have been concerned with developing methods to resolve the relative differences between strips. As a result of that research, the issue of strip adjustment in LIDAR data has been highlighted as a potential source of error. In order to evaluate the possible error sources between strips, the GPS time tag for each LIDAR shot was used in the validation procedure as will be discussed in the next section.

The validation of the LIDAR was carried out in the GIS environment using two methods:

1. Ground validation points were compared to proximal LIDAR points, and
2. Ground validation points were compared to the DEM derived from LIDAR ground points.

For all validation datasets the orthometric heights have been computed using the HT1_01 model to allow direct comparison with the LIDAR orthometric heights. For validation method 1, an automated procedure was coded in the Arc Macro Language (AML) that involved a user specified horizontal search radius, typically less than 5 m, around the validation point and all LIDAR ground points within that area were selected and orthometric heights were compared to that of the validation point. The details of the program are described elsewhere and the AML code is available for download (see Webster and Dias, in press). For LIDAR method A, Real Time Kinematic (RTK) GPS validation points were collected from a moving vehicle on the road and the search radius was restricted to 3 m (Figure 2.1). A Leica system 530 was used to collect the RTK GPS data with points collected within a maximum of 12 km from base stations to minimize errors. In general the carrier phase differential GPS real time data had a height precision smaller than 5 cm (1σ). For LIDAR method B, static carrier phase differential GPS validation points were collected in flat grass fields and a search radius of 5 m was used to ensure a sufficient sample of LIDAR points (Figure 2.1). Trimble single frequency (4600) and dual frequency (4000) GPS receivers were used in this survey and baselines were kept below 10 km with observation times greater than 1 hour. The reported vertical error of these GPS data was smaller than 3 cm (1σ). With the validation method that compares proximal LIDAR points to GPS points, two types of tables are produced within the GIS. One table summarized the statistics of the LIDAR points for each GPS validation point and the second table contains information for each LIDAR point that occurs within the specified radius of the validation point and includes the difference in height and horizontal distance between the points.

For validation method 2, the validation points are overlain on the gridded DEM surface and the cell value of the DEM is compared to the validation point's orthometric height. This method rapidly gives an assessment of the accuracy of the DEM product that was derived from the LIDAR ground points.

The combination of using both validation methods to determine possible LIDAR 'ground' point classification errors is described in the results section.

2.5. RESULTS

2.5.1. LIDAR METHOD A

For LIDAR method A, both validation techniques were used to analyze the LIDAR 'ground' points and the interpolated DEM. Only RTK GPS points with reported height precision less than 5 cm (1σ) were used in the error analysis. A total of 12,675 GPS RTK points were collected on the road and used with a 3 m search radius to extract LIDAR ground points. The summary statistics for the LIDAR 'ground' points within 3 m of the

GPS points is presented in Figure 2.3, A. The summary statistics indicate that these data have met the vertical specification, with a mean (Δz = GPS – LIDAR heights) less than 15 cm, however only 93.5 % of the LIDAR data are within 30 cm of GPS points. Of the original 12,675 GPS points, only 11,853 points had LIDAR 'ground' points within 3 m. Averaging the Δz values of proximal LIDAR points for each of the GPS points results in 98.9% of the GPS data being within 30 cm (Figure 2.3, B).

Derivative products from the LIDAR points, such as DEMs, are commonly used for subsequent analysis and deriving information about geologic and geomorphic features. Therefore an analysis of the LIDAR-derived DEM is useful and ensures every GPS point is used in the comparison because a continuous surface is constructed from the LIDAR 'ground' points. The 12,675 GPS points were overlain on the DEM and the corresponding cell values extracted and compared. The summary statistics for this analysis is presented in Figure 2.3, C. Many of the GPS locations that have a $\Delta z > 30$ cm, which are indicated in Figure 2.3, C, were not included in the previous analysis because no LIDAR 'ground' points were within 3 m of the GPS points. This situation commonly occurs at small bridges and other steep rises of the roadbed where the LIDAR points have been misclassified as 'non-ground' (Figure 2.4).

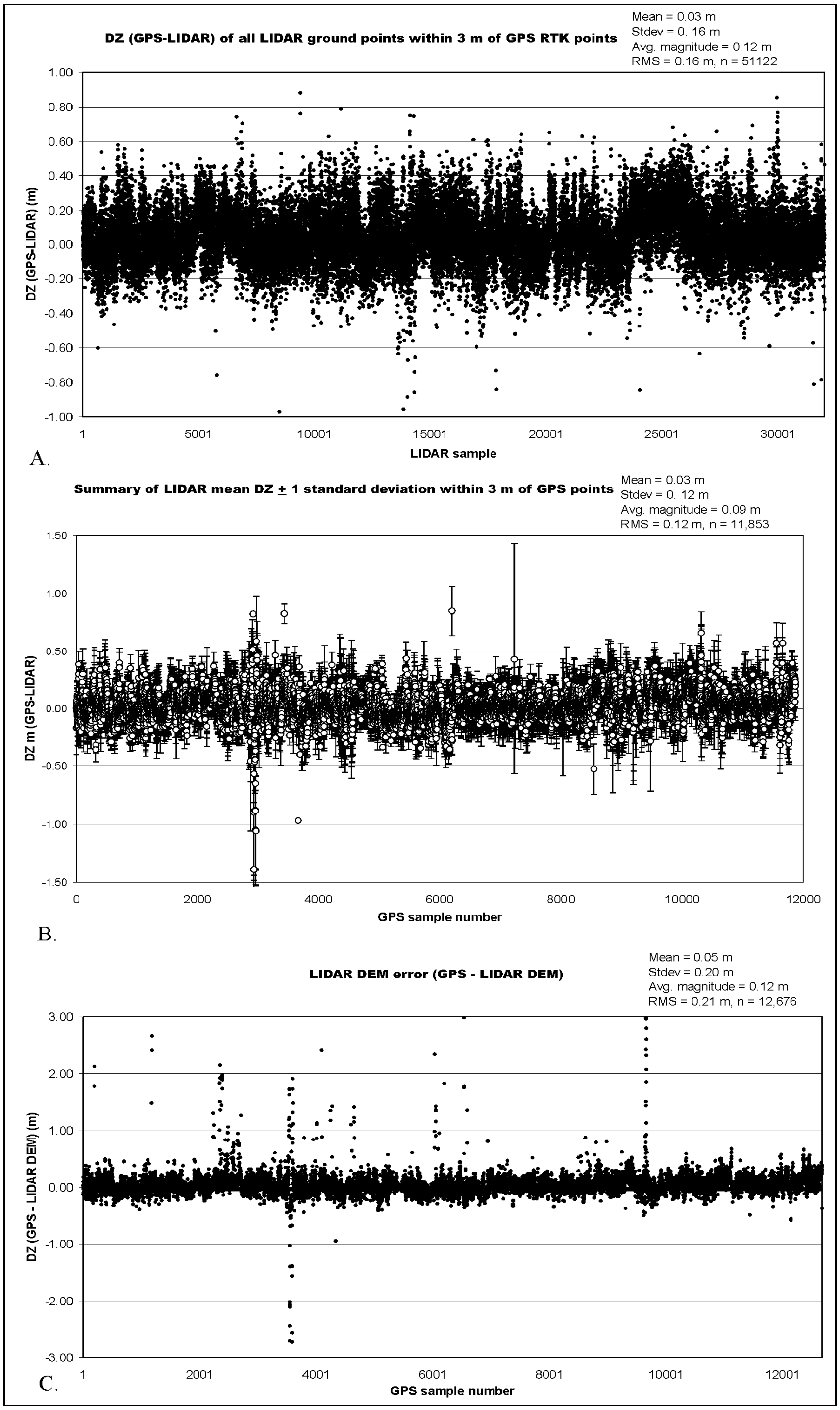

Figure 2.3 (A) Graph of Δ *z* for all the LIDAR ‘ground’ points within 3 m of GPS RTK points for LIDAR method A. (B) Graph of the mean value of Δ *z* ± 1σ error bars for each GPS validation point for LIDAR method A. (C) Graph of Δ *z* (GPS-LIDAR DEM) for the GPS validation points compared to the LIDAR method A DEM. Note Δ *z* is denoted DZ on the graph.

As a result, the DEM is too low for these areas and the roadbed is not properly represented because LIDAR points either side of the road have been misclassified as ‘ground’ and erroneously used to construct the DEM (Figure 2.4). The top map in Figure 2.4 shows the GPS points colour-coded by Δz (GPS-LIDAR DEM), and the lower map shows the GPS points colour-coded by the mean Δz (GPS-LIDAR points within 3 m of GPS points). The red points in the top map (Figure 2.4, A) are absent from the bottom map because no LIDAR ground points were within 3 m of those GPS points (Figure 2.4, B). This means that the Δz statistics generated from the first validation method did not include these errors (Figure 2.3, A). Thus, the combination of both validation methods (GPS compared to LIDAR points within a radius and GPS compared to the DEM surface) also highlight where the LIDAR classification algorithm may have misclassified LIDAR points as ‘non-ground’ when they truly represented ground features such as the elevated roadbed. By comparing all the GPS points to the DEM cell values (Figure 2.5), 95% of the GPS points have a Δz less than 30 cm. In Figure 2.5 the red GPS points highlight possible LIDAR point classification errors and correspond to the large positive values in Δz (Figure 2.3, C), where the DEM surface is too low. The graph of Δz for all LIDAR ground points within 3 m of GPS points (Figure 2.3, A) is symmetric about zero, with no significant large Δz values, because no LIDAR points classified as ‘ground’ occur

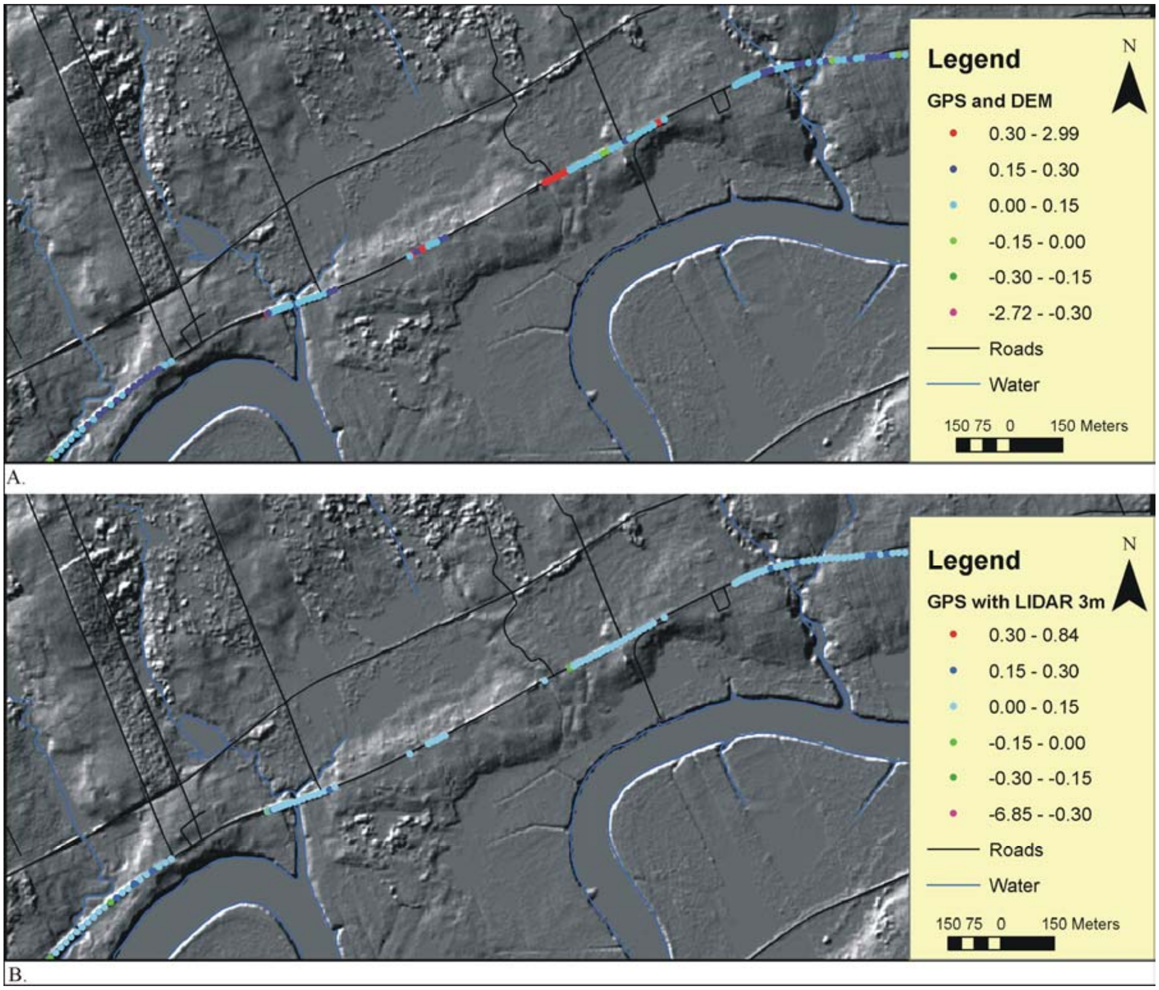

Figure 2.4 (A) The GPS points colour-coded based on Δ *z* (GPS-LIDAR DEM) overlaid on the shaded relief LIDAR DEM. (B) The GPS points that have LIDAR 'ground' points within 3 m and are colour-coded based on the mean Δ *z* (GPS-LIDAR) overlaid on the shaded relief LIDAR DEM. Note the points that exceed 30 cm in the top map (A) are absent in the lower map (B) as a result of the LIDAR points in these areas being classified as non-ground. Note Δ *z* is denoted DZ on the graph.

around those GPS points.

The issue of 'ground' points being classified as 'non-ground' occurs in other cases that are important from a geologic and geomorphic interpretation of the LIDAR-derived DEMs. Two cases encountered with this dataset included the roofs of large buildings being classified as ground and the tops of cliffs both along the coast and the cuesta of the North Mountain being classified as non-ground. Both situations can result in a DEM that does not accurately represent the landscape and can lead to possible erroneous interpretations. These types of misclassification errors for structures with steep slopes must be found and correctly classified prior to building the DEM.

High precision GPS cannot produce accurate results under the forest canopy and validation of the LIDAR-derived DEM in this environment is more difficult. A topographic survey consisting of two transects utilizing a Leica total station was conducted under the canopy. The site for the survey was selected in order to investigate a geomorphic ring structure that is visible on the "bald earth" DEM (Figures 2.5, 2.6). The structure is completely covered by forest with the exception of a small wetland on the eastern edge and a forest clear–cut to the west (Figure 2.6, A). From these open areas GPS control was established for the transects. The southwest-northeast trending transect consisted of 146 points with a mean Δz between the survey heights and the interpolated DEM heights of -0.1 m, a mean magnitude of error of 0.24 m, a standard deviation of 0.3 m, and a RMS error of 0.32 m (Figure 2.7, A). The southeast-northwest trending transect consisted of 102 points and had a mean Δz of –0.13 m, a standard deviation of 0.37 m, and a RMS error of 0.39 m (Figure 2.7, B). In general, both transects had LIDAR-derived DEM values slightly higher than the survey heights. These differences are interpreted to be a result of LIDAR returns from shrubs being classified as 'ground', thus causing the DEM surface to be a few decimeters higher in places than the actual ground (see Webster and Dias, in press for details of LIDAR point analysis).

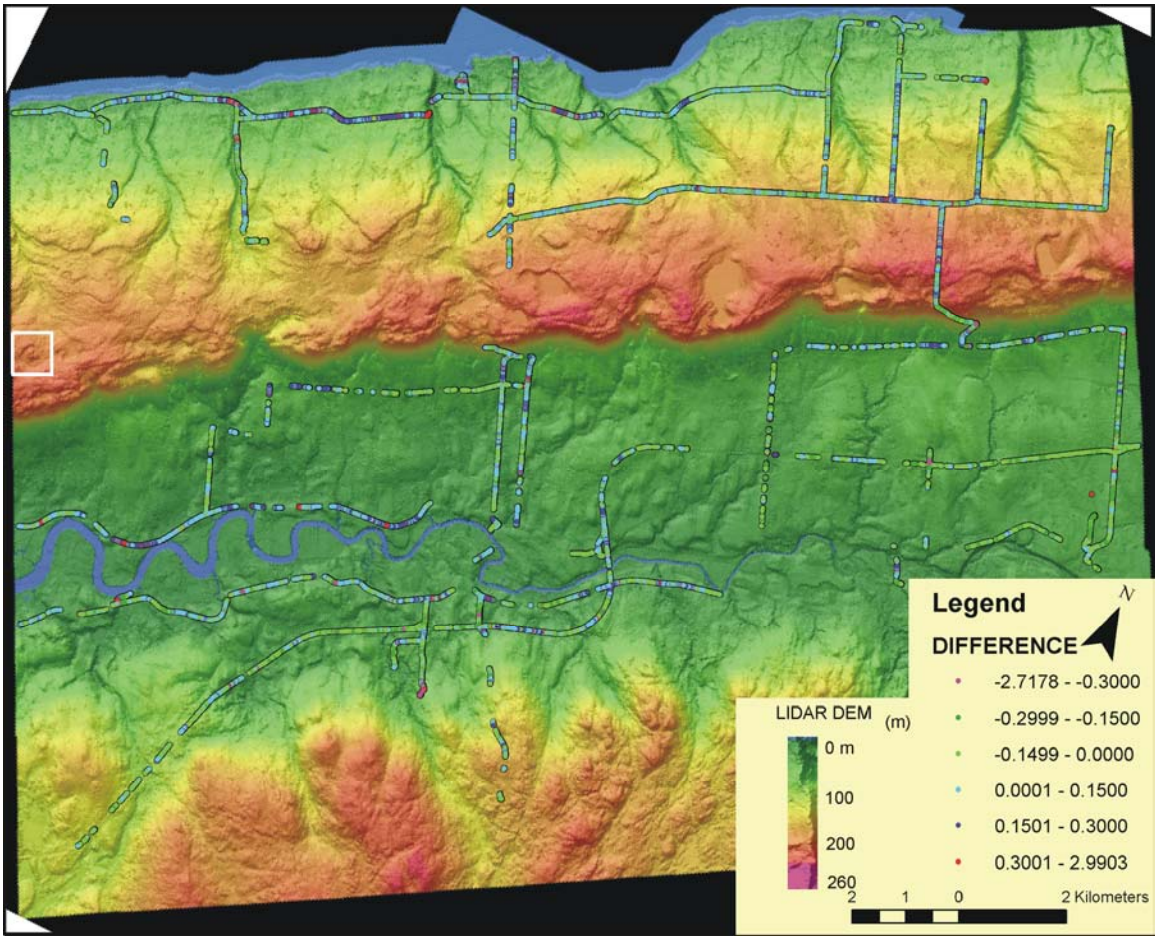

Figure 2.5 GPS points colour-coded by Δ *z* (GPS-LIDAR DEM) overlaid on the colour shaded relief LIDAR DEM. The white square inset in the upper left section of the map indicates the location of the transects under the forest canopy (Figure 2.6). The graph of Δ *z* and associated statistics of these GPS points is presented on Figure 2.3.

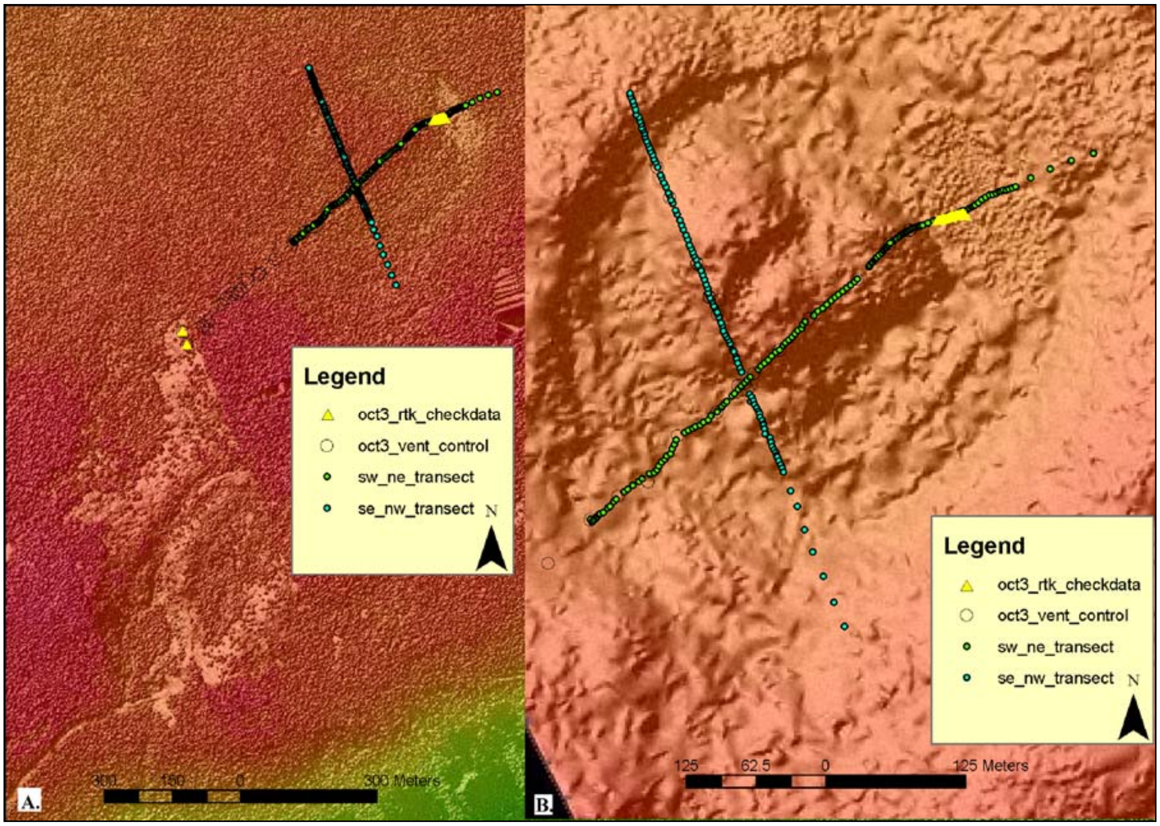

Figure 2.6 Location of the ring structure and transects. (A) This map represents a Digital Surface Model (DSM) derived from all the LIDAR points (‘ground’ and ‘non-ground’). A road leading to a forest clear-cut is present near the center of the map. This clear cut allowed for GPS data to be collected and used as control for the two forested transects utilizing a total station survey. (B) Larger scale “bald-earth’ DEM of the ring structure and associated transect locations. The yellow triangles represent the GPS control (west in the clear cut) and check data (east in the wetland) and the other dots represent the total station survey data.

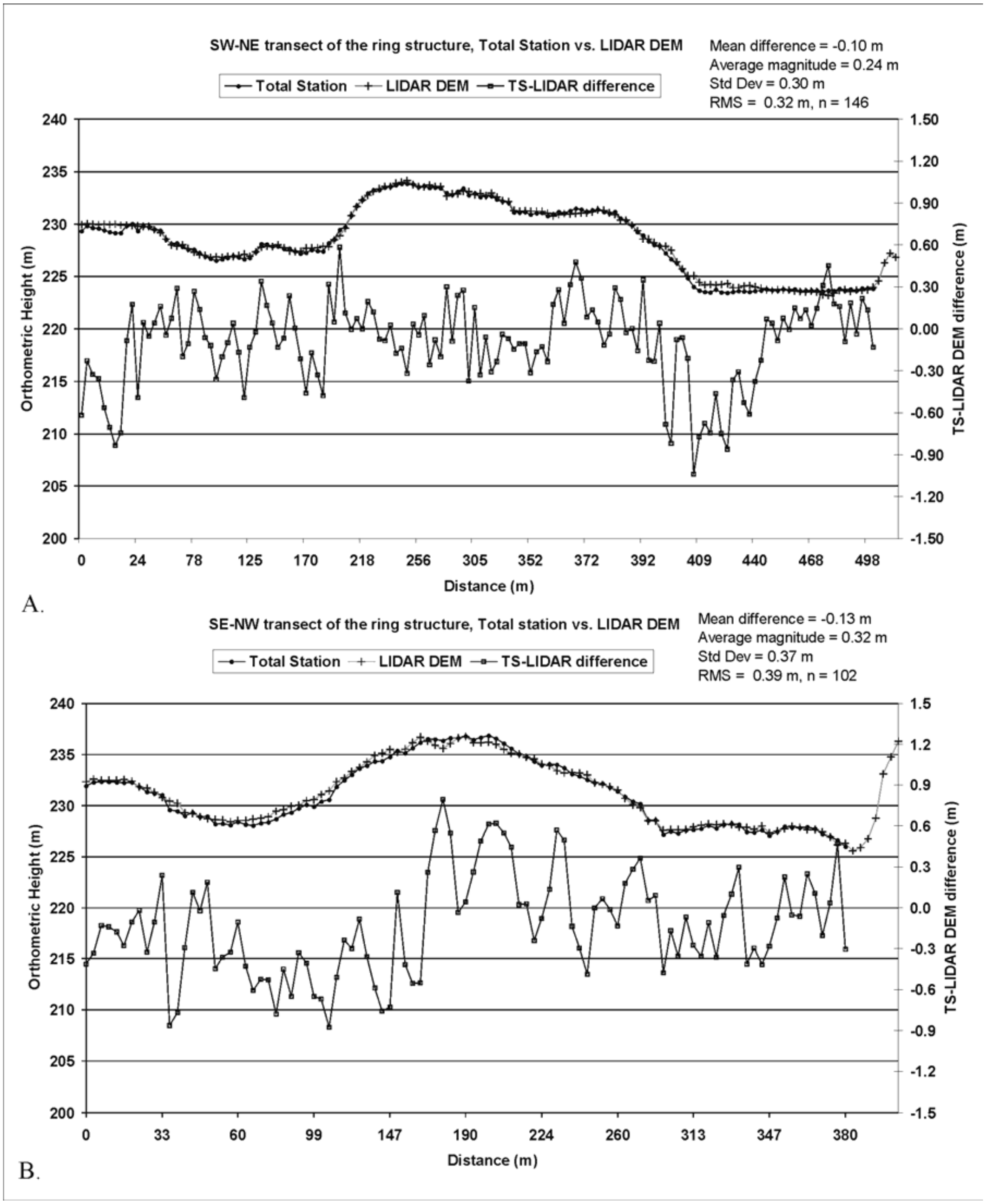

Figure 2.7 (A) Plot of the southwest-northeast trending transect across the ring structure. Total station survey points (black dots) and the LIDAR DEM points (black crosses). Height difference (open squares) corresponds to the scale on the right y-axis of the graph. (B) Plot of the southeast-northwest trending transect across the ring structure (same symbols). Note Δ *z* is denoted DZ on the graph.

2.5.2. LIDAR METHOD B

The reduced laser power during this survey resulted in LIDAR returns only from highly reflective targets such as deciduous trees and grass. As a result, most roads, buildings, and coniferous forest stands were absent from the dataset. To ensure a large sample of LIDAR ground returns for the validation analysis, GPS data were acquired in a systematic pattern across the LIDAR swaths in open flat grass-covered fields (Figure 2.1). As a result of the missing ground points over dark targets the resultant DEM was of limited use, therefore only validation method 1 was used with these data. A total of 51 post processed phase differential static GPS points were used and a 5 m horizontal search radius was specified around these points, resulting in 970 ground LIDAR points for comparison (Figures 2.1, 2.8).

The mean difference in orthometric heights between the LIDAR and validation points was 1.18 m with a standard deviation of 0.64 m and a RMS error of 1.34 m (Figure 2.8). As can be seen in Figure 2.8, there is a large spread in Δz and the values appear clustered for different elevations with variable ranges but no systematic pattern. The summary statistics indicate these LIDAR data do not meet the vertical specifications. The GPS Δz (GPS-LIDAR) standard deviation focuses attention on where the LIDAR data shows the most differences with the validation data and can be further examined (Figure 2.9).

For example, GPS sample number 19 has a ΔZ standard deviation of 1.35 m. The relationship between the height differences (ΔZ) of GPS point 19 and the 38 surrounding LIDAR points within 5 m appears random (Figure 2.10, A). However, if Δz is plotted

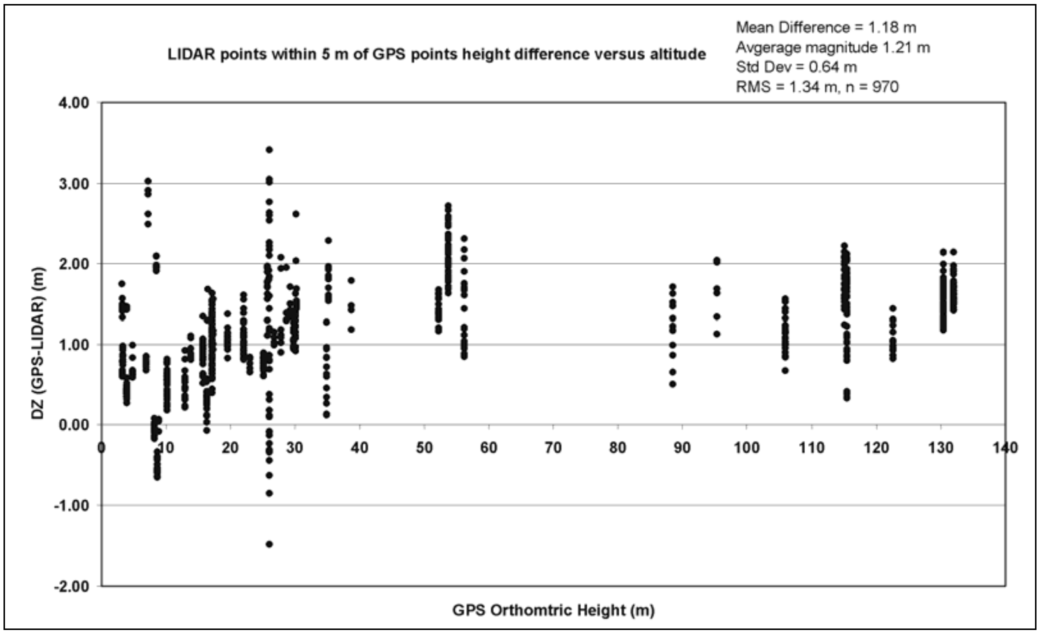

Figure 2.8 Graph of Δ *z* (GPS-LIDAR) of all LIDAR 'ground' points for method B within 5 m of GPS points versus the orthometric height. The mean Δ *z* is 1.18 m, with an average magnitude of 1.21 m, a standard deviation of 0.64 m and a RMS error of 1.34 m. Note Δ *z* is denoted DZ on the graph.

against GPS time, the time the LIDAR was collected, there are two distinct populations of Δ *z*, from -1.47 to 1.20 m and from 1.44 m to 3.4 m (Figure 2.10, B). Each distinct range of Δ *z* is associated with a different LIDAR GPS collection time that is in turn related to different flight lines. The time between LIDAR point acquisitions for this case is on the order of 1903 seconds or 30 minutes indicating the LIDAR points were collected in two different flight lines. When the LIDAR points are colour-coded by the GPS time tag the two flight lines are evident, and when the LIDAR points are colour-coded by Δ *z*, the spatial relationship between Δ *z* and each flight line becomes apparent. This systematic height bias between flight lines was evident in all of the GPS checkpoints

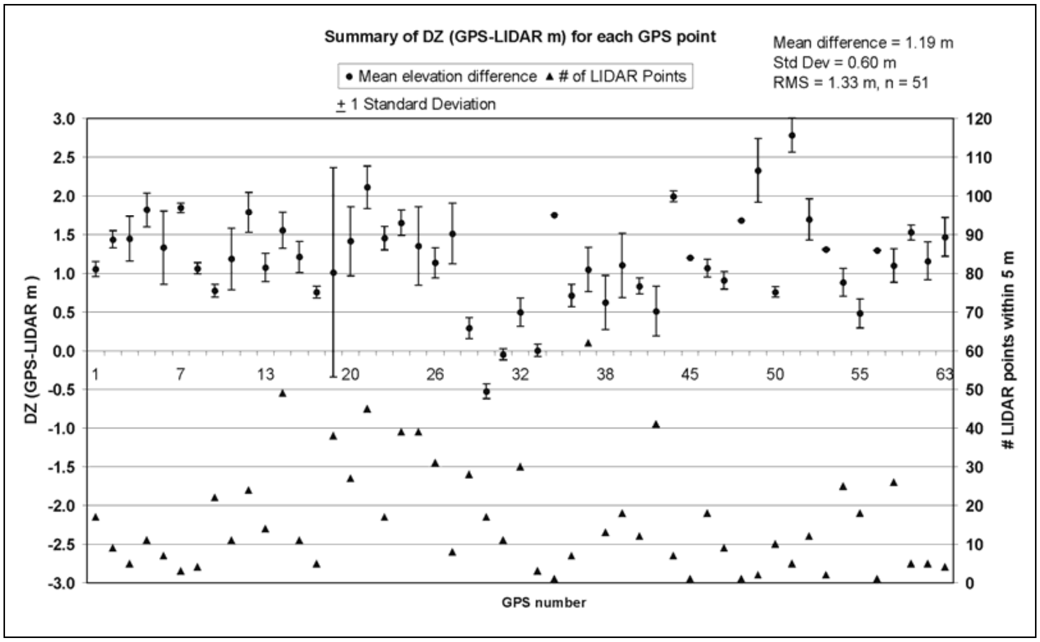

Figure 2.9 Graph of GPS points summary statistics of elevation differences with the surrounding LIDAR 'ground' points for LIDAR method B. The mean Δ *z* for each GPS point is denoted by black dots ± 1σ error bars. Number of LIDAR points within 5 m of each GPS point (black triangles) corresponds to the right y-axis of the graph. The mean Δ *z* is 1.19 m, a standard deviation of 0.60 m and a RMS error of 1.33 m. Notice GPS point 19 (Digby area) has a large standard deviation of 1.35 m and 38 associated LIDAR points. Note Δ *z* is denoted DZ on the graph.

that were collected. It was determined that the source of the vertical error was related to a range bias. This range bias was not correctly compensated for in the calibration procedures used during the survey. The LIDAR calibration procedure employed at that time involved flying at the planned survey height of 900 m and acquiring LIDAR points over the GPS base station located at the airport. From this procedure the raw laser ranges of the unit were calibrated. However, as a result of the power reduction of the laser, the actual flying height was reduced to approximately 600 m altitude during the actual survey, introducing a range bias that was not compensated for.

To verify this, several lines of LIDAR data were reprocessed with the appropriate scale factor and offset for the lower altitudes and matched the validation data more closely. Since the dataset was of limited value because of the sparse distribution of the points over dark targets as a result of the power reduction, the remainder of the data was not reprocessed; rather the study area was resurveyed in 2003-2004 with leaf-off conditions using a LIDAR with several improvements. A collimator was attached to the head of the laser having the effect of narrowing the beam divergence to smaller than 0.3 mrad. This resulted in the laser footprint being reduced from 180 cm to 18 cm. Although not tested directly, the smaller ground footprint of the laser beam should improve the horizontal accuracy of the system as well. Preliminary analysis indicates that these data meet the vertical specifications.

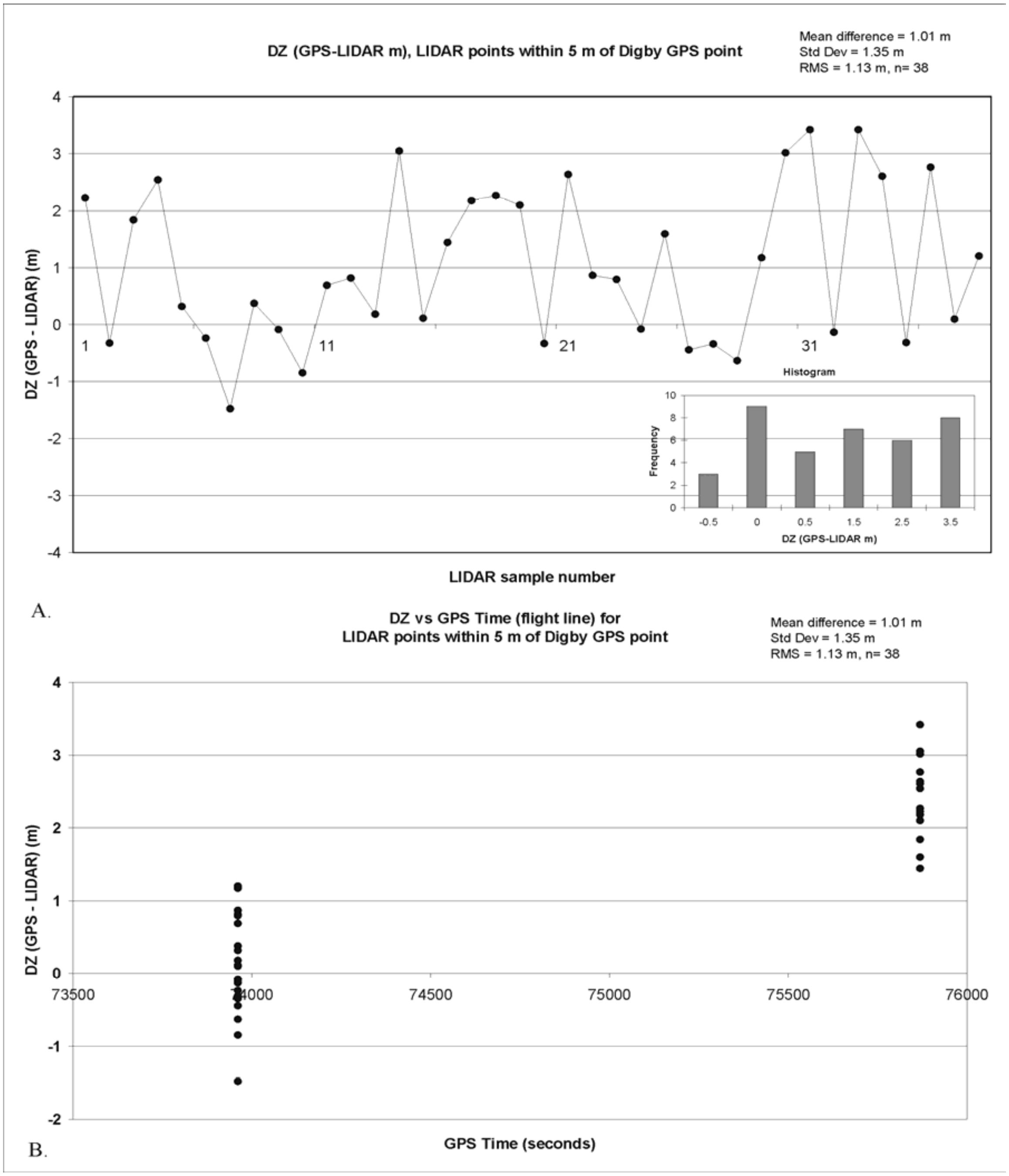

Figure 2.10 A. Graph of the 38 LIDAR points Δ *z* associated with GPS sample point number 19 for the Digby area. There is no apparent systematic pattern to Δ *z*. The lower right inset histogram shows a near equal distribution of Δ *z* from -0.5 to 3.5 m. B. Graph of the LIDAR points Δ *z* versus GPS acquisition time associated with GPS validation point number 19. The Δ *z* values appear to be related to the GPS time, each flight line has a different Δ *z* range associated with it. Note Δ *z* is denoted DZ on the graph.

2.6. SUMMARY AND CONCLUSIONS

This study demonstrates the importance of independent detailed validation data in order to ensure the LIDAR data meet the high accuracy specifications. With LIDAR vertical specification requirements of 15 cm on average and 95% of the data to be within 30 cm of measured GPS points requires validation data that exceeds this accuracy. The data from both LIDAR methods had extra data fields consisting of the GPS time tag for each LIDAR shot. This proved to be a very valuable attribute to enable the LIDAR points to be separated based on time and flight line, thereby facilitating comparisons with the vertical characteristics of the data between flight lines. In the case of method A, the vertical accuracy specifications were met, although misclassification errors were observed. In the case of method B, problems were encountered during the survey that resulted in a power reduction of the laser system and LIDAR ground points were absent for many dark targets. Method B did not meet the vertical accuracy specifications and the source of the vertical error related to a range bias that was not compensated for in the calibration procedures. The original survey was planned at an altitude of 900 m, however as a result of the power loss, the actual survey was flown at altitudes closer to 600 m. The change in flying height introduced range errors that were not accounted for. A range bias and scaling factor were computed and applied to some of the flight lines for confirmation.

A total station topographic survey was conducted in a mixed forest area where a ring structure with topographic relief on the order of about 10 m over a distance of 500 m was observed. Overall the RMS error under the canopy was about 10 cm larger than the validation results on the roadbed and was attributed to ground vegetation returns. However, the details of the profile generated from the DEM match that of the survey data sufficiently to consider the information from the DEM reliable for use in geological mapping and interpretation.

Specific conclusions that can be drawn from this study include:

1. When planning a LIDAR survey, familiarity with the terrain and land cover characteristics of the study area is necessary in order to select the most appropriate LIDAR system. This study shows that not all LIDAR systems are suited for all terrain conditions. For example, in the case of single return systems, a first return only system is suitable for areas of sparse vegetation, while a last return system is more appropriate for densely vegetated areas. The beam divergence and pulse repetition rate must also be considered in this context. For a first return system to measure the ground in vegetated terrain, a very narrow ground laser footprint is desired. The beam divergence will also influence the strength of the returning signal. This was evident during the repeat survey of method B when the beam divergence was reduced from a ground footprint of 180 cm to 18 cm diameter. However, if a last return system is used, a moderate beam footprint is desired so that some of the incident energy will make it past holes in the canopy and be reflected off the ground. In both cases the higher the laser pulse repetition rate the more total points there are, thus more points will make it to the ground, although this will increase the data volume.

2. Accurate classification of the LIDAR point cloud into ‘ground’ and ‘non-ground’ points is important for detailed geomorphic analysis. In this study the problem of misclassification was demonstrated with the raised roadbed. Current classification algorithms code points as being ‘non-ground’ if they exceed a variance threshold for a neighbourhood of points. Natural terrain breaks such as cliffs and nick points in stream profiles are subject to misclassification because of this. The data must be examined critically to check for such classification errors. The combination of the two validation methods facilitated the identification of these problems along the road. Improved point classification is an area of current research in the LIDAR community.
3. The selection of the season to conduct the survey is important for vegetated terrain and depends on the local climate. The detection of the ground in conditions of leaf-on and dense shrub and ground vegetation are problems for LIDAR systems. Leaf-off conditions are desired if a “bald-earth” DEM is the main purpose of a LIDAR survey. However, winter acquisitions present the problem of variable snow depths due to drifting. Thus the spring and fall time periods present the best alternatives. Of these periods, the spring has the added benefit of reduced shrub and under story vegetation height as a result of flattening by the winter snow pack. In this study the problem of shrub vegetation representing ground elevations was demonstrated in the validation work under the forest canopy for the ring structure.
4. Independent high precision validation data is required in order to check the vertical accuracy of the LIDAR data. Proper LIDAR sensor calibration

procedures must be employed in order to remove systematic errors that are present in the data when it is collected. As demonstrated in this study, insufficient calibration procedures resulted in a range bias that manifested itself as height differences between flight lines.

5. The use of GIS for automated validation procedures. In this study a large area of LIDAR data was collected resulting in a voluminous amount of data to be processed. The ability to automate validation procedures that examine the check data against the original LIDAR points and the derived DEM facilitates the identification of errors. As demonstrated here, the two techniques complement one another in identifying errors related to misclassification (e.g. roadbed surface classified as ‘non-ground’) and range bias.
6. The addition of the GPS time tag or a flight line identifier in the LIDAR data is extremely useful for validation purposed. Without such a field it would be very difficult to identify systematic errors between flight lines such as the range bias identified and described in this study.

2.7. ACKNOWLEDGEMENTS

This study benefited from the contribution of several people. I would like to thank the financial assistance of Brendan Murphy, St. FX University and the Nova Scotia Community College (NSCC) towards my PhD. I would like to thank the support of my thesis committee consisting of Brendan Murphy, John Gosse, and Ian Spooner. I would also like to thank Dennis Kingston and the AGRG students involved in some of the validation data collection: Paul Fraser and Dan Deneau for the 2001 rapid static GPS survey, and Trevor Milne and the students from the AGRG class of 2003-2004 for the total station survey. Also, George Dias for writing the AML code for the first validation procedure and Lisa Markham and Dan Deneau for assisting in parts of the AML. Special thanks to Bob Maher and David Colville of the AGRG, and Don Forbes of the Geological Survey of Canada for their support and constructive comments during the project. The LIDAR data for this project was funded by an infrastructure grant to NSCC from the Canadian Foundation for Innovation, Industry Canada. I would like to thank an anonymous reviewer who’s suggestions and comments have improved the manuscript.

CHAPTER 3. AN AUTOMATED GIS PROCEDURE FOR COMPARING GPS AND PROXIMAL LIDAR ELEVATIONS

Tim L. Webster

Department of Earth Sciences, Dalhousie University

and

Applied Geomatics Research Group

Centre Of Geographic Sciences, Nova Scotia Community College

50 Elliot Road, RR#1

Lawrencetown, NS, Canada, B0S 1M0

George Dias

Applied Geomatics Research Group

Centre Of Geographic Sciences, Nova Scotia Community College

50 Elliot Road, RR#1

Lawrencetown, NS, Canada, B0S 1M0

Keywords: LIDAR; height validation; GPS; GIS; Digital Elevation Model

3.1. ABSTRACT

High-resolution elevation surveys utilizing LIDAR (Light Detection And Ranging) are becoming available to the geoscience community to derive high resolution DEMs that are used in a variety of application areas. However, prior to the application of these data to geomorphic interpretation, extensive validation procedures should be employed. The vertical accuracy specification for the survey called for heights to be within an average of 15 cm of measured GPS heights and 95% of the data to be within 30 cm. Two different LIDAR systems and collection methods were employed to collect data for the study area located in the Mesozoic Fundy Basin in eastern Canada. High precision GPS surveys were conducted to measure the ground elevations in open areas and a traditional topographic survey was carried out in order to assess the accuracy of the laser data under the forest canopy. The LIDAR and validation data were integrated into a GIS where an automated procedure was developed that allows the user to specify a search radius out from the validation points in order to compare proximal LIDAR points. This procedure facilitates examining the LIDAR points and the validation data to determine if there are any systematic biases between flight lines in the LIDAR data. The results of the validation analysis of the two LIDAR methods and a description of the automated procedure are presented in this paper.

3.2. INTRODUCTION

LIDAR (Light Detection and Ranging) is a remote sensing technology to derive very accurate elevation measurements of the earth's surface. Flood and Gutelius (1997) and Wehr and Lohr (1999) provide a general overview of airborne laser scanning (LIDAR) technology and principles. LIDAR has been used for engineering, flood risk mapping (Webster et al. 2004*a, b*) and its utility has been demonstrated in glacier mass balance investigations (Krabill et al., 1995, 2000; Abdalati and Krabill, 1999). Applications to coastal process studies in the USA have been reported by Brock et al. (2002), Sallenger et al. (1999), Krabill et al. (1999), and Stockdon et al. (2002), among others. Harding and Berghoff (2000) have demonstrated the use of LIDAR for mapping groundwater infiltration and runoff. Harding and Berghoff (2000) and Haugerud et al. (2003) have reported on using LIDAR to map recent tectonic fault scarps and geomorphic features in Washington State. Various studies have been reported on the calibration and systematic errors of LIDAR systems (Kilian et al., 1996; Burman, 2000; Filin, 2001, 2003*a, b*; Katzenbeisser, 2003) and the accuracy of laser altimetry data (Huising and Gomes Pereira, 1998; Kraus and Pfeifer, 1998; Crombaghs et al., 2000; Schenk et al., 2001; Maas 2000, 2002; Artuso et al., 2003; Bretar et al., 2003; Elberink et al., 2003; Kornus and Ruiz, 2003; Hodgson et al., 2003; Hodgson and Bresnahan, 2004; Hodgson et al., 2005; Hopkinson et al., 2005). Some of these studies examined the relative accuracy between LIDAR strips and in some cases the absolute accuracy was evaluated if sufficient control was available (e.g. Huising and Gomes Pereira, 1998; Ahokas et al., 2003). Thus, prior to interpreting geomorphic features highlighted by the enhanced resolution provided by LIDAR, the accuracy of the LIDAR datasets should first be analyzed.

Two data acquisition companies were contracted to acquire LIDAR data during leaf-on conditions in 2000 using two different LIDAR systems for the study area located on the southeast shore of the Mesozoic Fundy Basin of Maritime Canada (Figure 3.1). The area includes the North Mountain and the South Mountain that bound the Annapolis Valley and has relief on the order of 265 m (Figure 3.1). The valley floor consists of agriculture and urban landuse, and the North and South Mountains are mainly covered with dense forest. In order to test the accuracy of the LIDAR data, high-precision Global Positioning System (GPS) and traditional surveying measurements were acquired over a variety of landcover types both in the open and under the vegetation canopy. The LIDAR and validation check data were integrated into a GIS where an automated validation algorithm was coded and used for the analysis. Height validation procedures often involve comparing checkpoints to the interpolated DEM surface. While this approach is fast and reports the overall accuracy of the final DEM, it is limited in providing details on the actual LIDAR points and does not facilitate testing for systematic errors between flight lines. In this study an algorithm was developed in a GIS environment to compare checkpoints to proximal LIDAR points within a specified search radius. A companion paper (see Webster, in press) describes the results from the validation of the two different LIDAR survey methods using this proximal point technique and comparing the GPS data to the interpolated LIDAR DEM. The focus of this paper will be on the automated validation algorithm and the height variance between flight lines (strips) will be

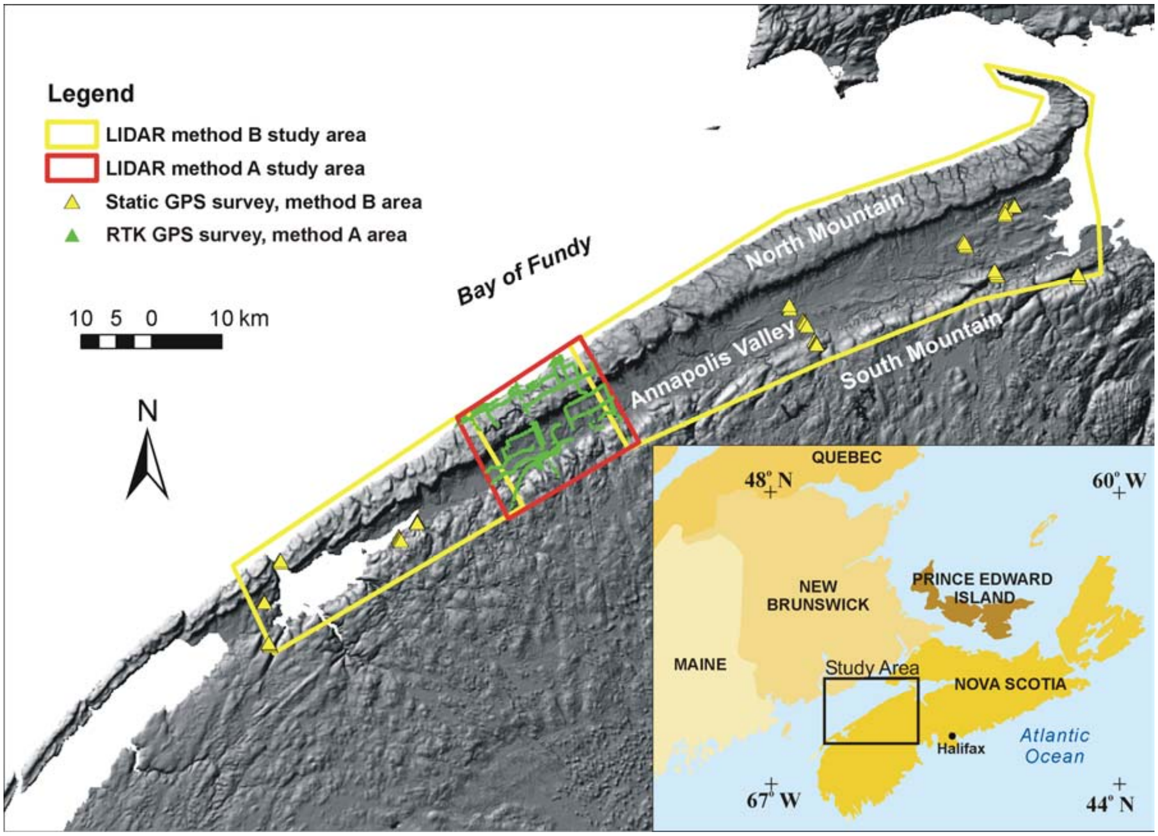

Figure 3.1 Shaded relief map for the Annapolis Valley, Nova Scotia, highlighting the study areas of LIDAR methods A and B and GPS points used in the validation process. There are over 12,000 GPS points used for validating method A (green triangles) and 51 GPS points used for validating method B clustered in 5 locations throughout the valley, many symbols (yellow triangles) overlap at the scale of this map. Location map inset in lower right is depicting the study area in Maritime Canada. The shaded relief map is derived from 20 m DEM produced by the Nova Scotia Geomatics Center, Service Nova Scotia & Municipal Relations.

demonstrated by presenting the results of the analysis from two different LIDAR survey methods.

3.3. LIDAR SYSTEMS AND SURVEYS

LIDAR systems are a convergence of three separate technologies to enable decimeter-level accuracy in surface elevation measurements from an aircraft (Kilian et al.

1996). The system consists of a Global Positioning System (GPS), an Inertial Measurement Unit (IMU) or an Inertial Reference System (IRS), and the laser ranging system. The GPS is used to map the aircraft trajectory precisely (at cm level) and the IMU is used to measure the attitude of the aircraft (roll, pitch, and yaw or heading). The laser ranging system is used to emit a pulse of coherent radiation, near-infrared in the case of terrestrial LIDAR, toward the earth's surface and measures the travel time of the transmitted and reflected pulse. The Time Interval Meter (TIM) records the laser pulse travel time and converts it into a range based on the speed of light. This range is then adjusted for scan angle and aircraft attitude in combination with the position of the aircraft derived by GPS. The resultant three-dimensional position of each reflected LIDAR pulse is based on the GPS coordinate system (latitude, longitude, and ellipsoidal height using the WGS84 reference ellipsoid).

There is no standard format for LIDAR data. However, a proposed binary format has recently been published that had several additional parameters such as scan angle for each LIDAR point (Schuckman, 2003). In 2000, LIDAR data were typically delivered in ASCII files consisting of *x,y,z* data. In addition to the typical *x,y,z* data fields for the LIDAR, the GPS time for every laser shot was also included. This gives the ability to examine the LIDAR data by GPS time or flight line (strip). The elevations were converted from ellipsoidal (smooth mathematical surface representing the earth) to orthometric heights above the geoid (equipotential surface based on the earth's gravity field) based on the HT1_01 model available from the Geodetic Survey of Canada, and both sets of heights were included. Each LIDAR method classified the processed LIDAR point cloud into two categories: 'ground' and 'non-ground' points. An overview of the general classification procedure used by many of the automated routines is provided in Hodgson et al. (2005). They point out that most LIDAR data providers consider the details of this process proprietary and do not report the specifics of the parameters used for the classification. The ground and non-ground LIDAR point data were delivered in 4 km by 4 km tiles based on a UTM grid.

LIDAR method A used an Optech ALTM1020 sensor mounted in a Navajo P31 twin engine fixed-wing aircraft. The LIDAR operated at a 5000 Hz laser repetition rate along with the scanning mirror operating at 15 Hz to direct the laser pulses across the swath. At a flying altitude of 800 m the laser beam had a ground footprint diameter of 25 cm. Since a “bald earth” DEM was one of the desired outcomes of the survey, the LIDAR unit was set to record the last return pulse. This increased the probability of getting a return from the ground or close to it in forested areas. The survey was conducted during a two-week period in July 2000. The LIDAR provider classified the point cloud into ‘ground’ and ‘non-ground’ points using the REALM program from Optech (Toronto, Canada) prior to data delivery. The data supplier did not provide the details of the parameters used in this process.

LIDAR method B used a system that integrated the individual components (GPS, IMU, laser) described above. This first return LIDAR system was originally designed for corridor mapping and was mounted on a pod that was fixed to the underside of a Bell Ranger 206 helicopter. The LIDAR operated at a 10,000 Hz laser repetition rate along with the scanning mirror operating at 15 Hz to direct the laser pulses across the swath. At a flying altitude of 600 m the laser beam had a ground footprint diameter of 180 cm. The survey was conducted during a three-week period during August 2000. The LIDAR provider classified the point cloud into ‘ground’ and ‘non-ground’ points using proprietary software prior to data delivery. The data supplier did not provide the details of the parameters used in this process.

3.4. LIDAR VALIDATION BACKGROUND AND TECHNIQUES

The accuracy of LIDAR data depends on the removal of the systematic errors associated with the system (Filin, 2001, 2003*a, b*). Several researchers have examined the issues of LIDAR validation and have highlighted the potential for errors between flight lines or strips (Kilian et al., 1996; Huising and Gomes Pereira 1998; Crombaghs et al. 2000; Maas 2000, 2002; Schenk et al., 2001; Latypov and Zosse 2002; Ahokas et al., 2003; Bretar et al., 2003; Elberink et al., 2003; Kornus and Ruiz, 2003). Many of the studies have dealt with individual flight strips, where the overlapping areas are compared either as points or as interpolated surfaces. As pointed out by Filin (2003*a*), the information that is delivered to the user is not the complete set of system measurements (aircraft trajectory, alignment of the sensor head to the IMU and GPS phase center), but rather the laser points themselves thus making the identification of systematic errors more difficult. The common method of delivery from commercial data providers is for individual strips to be merged and the points delivered as tiles based on a geographic grid system to facilitate data management. In order to evaluate the possible error sources between strips, the GPS time tag for each LIDAR point was used in the validation procedure. In this study the absolute accuracy rather than relative accuracy was desired, therefore extensive ground control using GPS and traditional survey methods were used in the analysis. In all cases the HT1_01 model was used to transform the GPS ellipsoidal heights into orthometric heights for comparison with the LIDAR data.

The vertical accuracy specification for the LIDAR surveys called for heights to be within an average of 15 cm of measured GPS heights and 95% of the data to be within 30 cm. The LIDAR 'ground' and 'non-ground' points and validation checkpoints were imported into an Arc/Info GIS workstation running on a Unix platform. A "bald earth" DEM was constructed from the 'ground' points from LIDAR method A and used in part of the validation process. A Delaunay-triangular irregular network (TIN) was constructed and a 2 m grid was interpolated from the TIN to build the DEM. The validation of the LIDAR data was carried out in the GIS environment.

Artuso et al. (2003) described the implementation of semi-automated routines written in Perl and C to verify large volumes of LIDAR data for parts of Switzerland. In this study, an automated routine was coded in the Arc Macro Language (AML) in the ESRI GIS environment. The validation technique involves a user-specified horizontal search radius, typically less than 5 m, around the validation point for comparison with LIDAR ground points. All LIDAR ground points within that search area are selected and orthometric heights are compared to that of the validation point. In the case of real time kinematic (RTK) GPS validation points collected from a moving vehicle on the road, the search radius was restricted to 3 m in order to minimize comparing LIDAR points in the ditch with validation points on the road. One must also consider the source of the validation data and type of terrain, for example if the slope of a road exceeds a 10% grade (rare for this study area) then a 3 m radius can bias the resultant statistics and a smaller radius should be used. This is not a problem when the validation data are compared with the DEM because the local trend surface of the proximal LIDAR points has been taken into account with the TIN structure and interpolation process. In the case of validation points collected in horizontal grass fields, a search radius of 5 m was used to ensure a sufficient sample of LIDAR points for method B.

The validation technique that compares proximal points requires four inputs: (1) the location and name of the control points coverage and elevation field; (2) the search radius (assume 5 m) from the control points to select and compare LIDAR points; (3) the location of the workspace where LIDAR point coverages are located and the elevation field in the attribute table to used in the analysis; and (4) the location or a new directory name where the output will be directed (Figure 3.2). The program output consists of two GIS point coverages; the GPS control points (results5.pat) and LIDAR points (mrg_pnts5.pat) within the search radius, and three addition tables (Figure 3.2). The first table summarizes the statistics of the LIDAR points for each GPS validation point (pntstats5gr.dat) and includes: frequency (number of LIDAR points within the specified radius), minimum *z* difference between the validation and LIDAR points, maximum *z* difference, mean *z* difference, and the standard deviation of the *z* value differences. The next table contains information for each LIDAR point (pntdist5.dat) that occurs within the specified radius of the validation point and includes: the original LIDAR point identifier, the GPS point identifier, distance to the closest GPS point, the GPS *z* value, and the difference in *z* values between the LIDAR and GPS validation point. Relating this table back to the original LIDAR points allows one to examine the relationship between

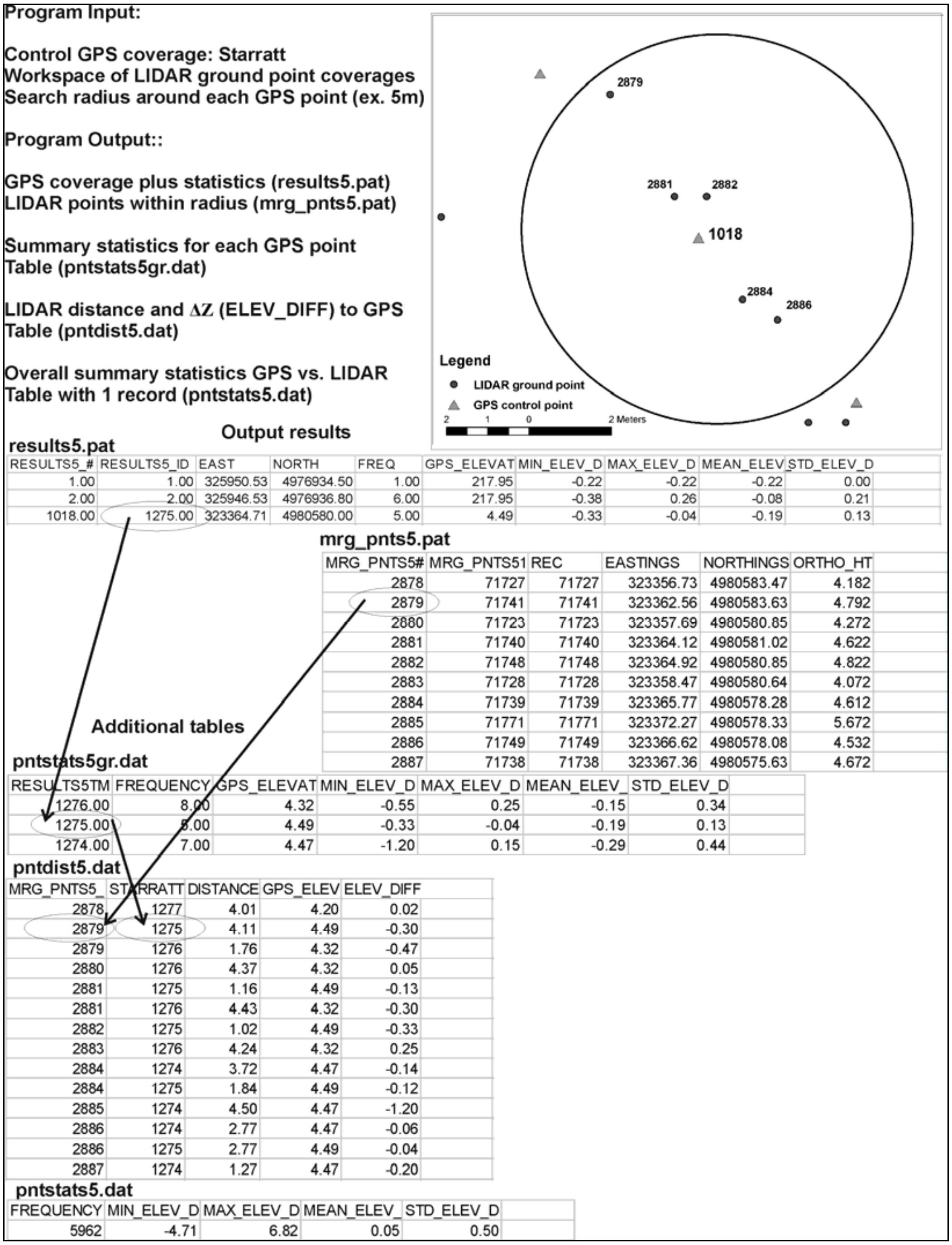

Program Input:

Control GPS coverage: Starratt
Workspace of LIDAR ground point coverages
Search radius around each GPS point (ex. 5m)

Program Output::

GPS coverage plus statistics (results5.pat)
LIDAR points within radius (mrg_pnts5.pat)

Summary statistics for each GPS point
Table (pntstats5gr.dat)

LIDAR distance and ΔZ (ELEV_DIFF) to GPS
Table (pntdist5.dat)

Overall summary statistics GPS vs. LIDAR
Table with 1 record (pntstats5.dat)

Output results

results5.pat

RESULTS5_#	RESULTS5_ID	EAST	NORTH	FREQ	GPS_ELEVAT	MIN_ELEV_D	MAX_ELEV_D	MEAN_ELEV	STD_ELEV_D
1.00	1.00	325950.53	4976934.50	1.00	217.95	-0.22	-0.22	-0.22	0.00
2.00	2.00	325946.53	4976936.80	6.00	217.95	-0.38	0.26	-0.08	0.21
1018.00	1275.00	323364.71	4980580.00	5.00	4.49	-0.33	-0.04	-0.19	0.13

mrg_pnts5.pat

MRG_PNTS5#	MRG_PNTS51	REC	EASTINGS	NORTHINGS	ORTHO_HT
2878	71727	71727	323356.73	4980583.47	4.182
2879	71741	71741	323362.56	4980583.63	4.792
2880	71723	71723	323357.69	4980580.85	4.272
2881	71740	71740	323364.12	4980581.02	4.622
2882	71748	71748	323364.92	4980580.85	4.822
2883	71728	71728	323358.47	4980580.64	4.072
2884	71739	71739	323365.77	4980578.28	4.612
2885	71771	71771	323372.27	4980578.33	5.672
2886	71749	71749	323366.62	4980578.08	4.532
2887	71738	71738	323367.36	4980575.63	4.672

Additional tables

pntstats5gr.dat

RESULTS5TM	FREQUENCY	GPS_ELEVAT	MIN_ELEV_D	MAX_ELEV_D	MEAN_ELEV_	STD_ELEV_D
1276.00	8.00	4.32	-0.55	0.25	-0.15	0.34
1275.00	5.00	4.49	-0.33	-0.04	-0.19	0.13
1274.00	7.00	4.47	-1.20	0.15	-0.29	0.44

pntdist5.dat

MRG_PNTS5_	STARRATT	DISTANCE	GPS_ELEV	ELEV_DIFF
2878	1277	4.01	4.20	0.02
2879	1275	4.11	4.49	-0.30
2879	1276	1.76	4.32	-0.47
2880	1276	4.37	4.32	0.05
2881	1275	1.16	4.49	-0.13
2881	1276	4.43	4.32	-0.30
2882	1275	1.02	4.49	-0.33
2883	1276	4.24	4.32	0.25
2884	1274	3.72	4.47	-0.14
2884	1275	1.84	4.49	-0.12
2885	1274	4.50	4.47	-1.20
2886	1274	2.77	4.47	-0.06
2886	1275	2.77	4.49	-0.04
2887	1274	1.27	4.47	-0.20

pntstats5.dat

FREQUENCY	MIN_ELEV_D	MAX_ELEV_D	MEAN_ELEV_	STD_ELEV_D
5962	-4.71	6.82	0.05	0.50

Figure 3.2 Explanation of the “validate.aml” tool including input and output files and how they relate. A 5 m radius around each GPS point has been used in this example, thus the output names “results5” and “mrg_pnts5” are assigned by the program to denote the 5 m search radius. The inset map shows the GPS point (triangle labeled 1018) with 5 LIDAR points (dots) within a 5 m radius.

the LIDAR GPS time tag or flight line, and the orthometric height difference. From these two tables the relationship between the LIDAR points and the validation points can be summarized and visualized. The last table reports the overall summary statistics between the all the GPS and LIDAR heights (pntstats5.dat).

3.5. VALIDATION RESULTS

3.5.1. LIDAR METHOD A VALIDATION

A total of 12,675 RTK GPS points with a reported standard deviation of height less than 5 cm were collected in 2003 and used in the validation analysis (Figure 3.1). Since the GPS points were collected on the road, a 3 m search radius was selected to extract LIDAR ground points. A total of 51,122 LIDAR points fell within 3 m of 11,853 GPS points. This indicates that 958 GPS points did not have LIDAR 'ground' points within 3 m of them. The summary statistics for the LIDAR points within 3 m of the GPS points show a mean difference in orthometric height (Δz = GPS-LIDAR) of 0.03 m, with a standard deviation of 0.16 m and a root mean square (RMS) error of 0.16 m (Figure 3.3). Because these GPS points were collected on the road and not necessarily on level surfaces, the height difference between the LIDAR and GPS, Δz, increases as one moves away from the validation point (Figure 3.4).

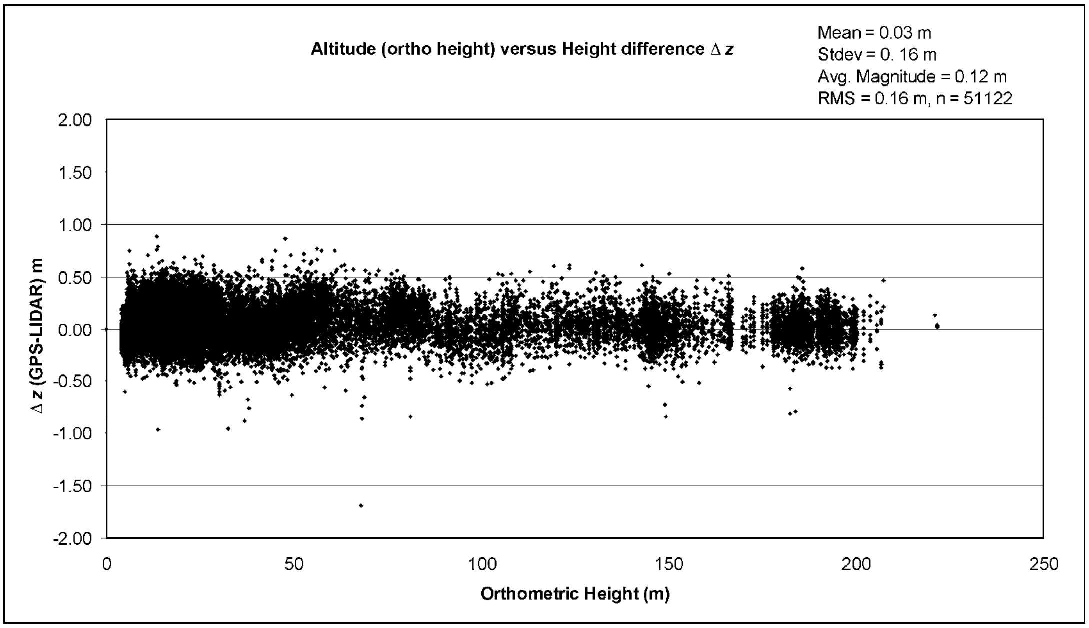

Figure 3.3 Graph of orthometric height and Δ *z* (GPS-LIDAR) and summary statistics for LIDAR method A.

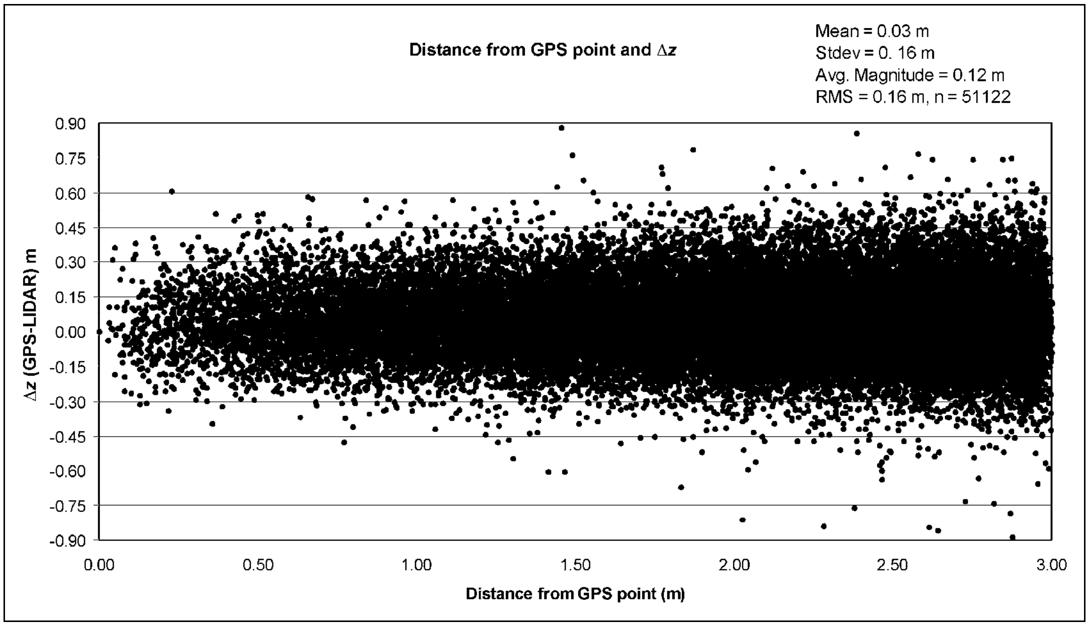

Figure 3.4 Graph of distance from the validation point up to 3 m and Δ *z*. The difference in height Δ *z* increases as a function of distance from the GPS points.

From the summary statistics, these data have met the vertical specification, with a mean Δz less than 15 cm. The number of LIDAR 'ground' points within 3 m of GPS validation points that are within 30 cm is 47,779 or 93.5 % of the data. This indicates that the data does not meet the specification that called for 95% of the LIDAR data to be within 30 cm. An inspection of the points that are outside of the 30 cm range indicates several of them appear on the edge of the road and may represent the slope of the ditch. This observation suggests that a 3 m search radius is too large an area for the road survey GPS points, which is consistent with the information in Figure 3.4, which shows the Δz increasing with distance from the GPS validation points. LIDAR points within 2 m of GPS points were then analyzed and 96.2% of them were within 30 cm, indicating the data met the specifications. Any errors introduced by local surface trends of the LIDAR points within 2 m of the GPS point are resolved when the GPS points are overlain on the interpolated DEM which takes the local trend into account. The Δz was also examined with respect to the LIDAR GPS time to determine if there were any systematic errors related to flight lines (Figure 3.5). This figure shows that the distribution of Δz is consistent between GPS times or flight lines and shows an even distribution either side of the 0 m value. Overall, there does not appear to be any significant systematic height bias between flight lines.

The GPS summary statistics are similar to those of the LIDAR data, however the number of GPS points where the mean Δz is within 30 cm is 11,717 that is 98.9% of the total GPS validation dataset. Averaging the Δz values of the LIDAR points within the 3 m radius indicates the LIDAR data have met the vertical specification of 95% of the data

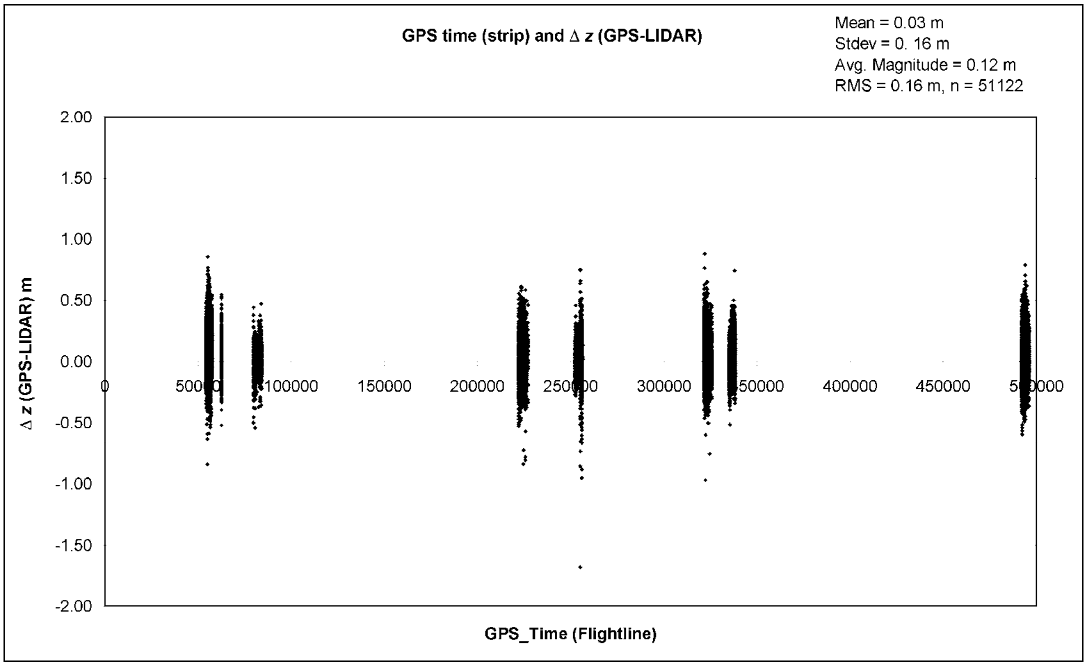

Figure 3.5 Graph of LIDAR GPS time (flight line) and Δ *z*. There is no systematic pattern of Δ *z* with respect to GPS time.

being within 30 cm. The above approach of comparing LIDAR points within a given radius of GPS points works well where LIDAR points exist. However, omission error may be a problem if LIDAR ground points are missing within the search radius of the GPS point. Typically, this occurs when the LIDAR points have been classified as non-ground points, and are thus not included in the validation process.

When the GPS points are overlain on the LIDAR DEM and the cell values are compared (Figures 3.2, 3.6), the vertical specifications are met (for more details see Webster, in press). The summary statistics for the LIDAR DEM show a mean difference in orthometric height (Δ *z* = GPS-LIDAR DEM) of 0.05 m, with a standard deviation of 0.20 m and a RMS error of 0.21 m. When the Δ *z* values of each GPS point are compared between the two validation techniques (mean Δ *z* in the case of the proximal LIDAR points), the differences highlight ground classification errors and the steep slopes along the road.

Validation of the LIDAR data and derived DEM under the vegetation canopy is more difficult as a result of not being able to use high precision GPS in such environments. Ahokas et al. (2003) used a 2 m search radius in a forested area to examine the ground height error between strips and at different flying heights from two different LIDAR systems. They calculated the mean Δz for all the points and Δz for the nearest and interpolated surface and found they all gave similar results. For this study, two detailed transects were measured using traditional survey methods that employed a total station. The site for the survey was selected in order to investigate a geomorphic ring structure within the North Mountain basalt that is visible on the "bald earth" DEM (Figures 3.6, 3.8). The structure is completely covered by mixed forest with the exception of a small wetland on the eastern edge. A forest clear cut exists approximately 300 m west of the structure that was used to collect high-precision GPS coordinates that established control for the total station survey (Figure 3.7). The forest consists of deciduous species of maple (red on Figure 3.7, A), beech (Yellow on Figure 3.7, A), spruce and fir coniferous species (green on Figure 3.7, A). The density of the under story is variable with the largest density of shrubs occurring in low-lying areas. The shrubs are broad leafed and range in height between 50 cm and 1.5 m. In general, both transects had LIDAR-derived DEM values higher than the survey heights. The larger differences in Δz appear to be associated with abrupt changes in ground slope (Figure 3.8). Since the LIDAR data were collected with leaf-on conditions and the area consists of relatively dense forest 10-15 m in height, this difference may be attributed to the effect of interpolation of the LIDAR ‘ground’ points to the DEM. This implies that if the laser beam did not make it to the ground at the foot of the slope, possibly reflecting from shrubs, the terrain will not be accurately represented in the interpolated DEM.

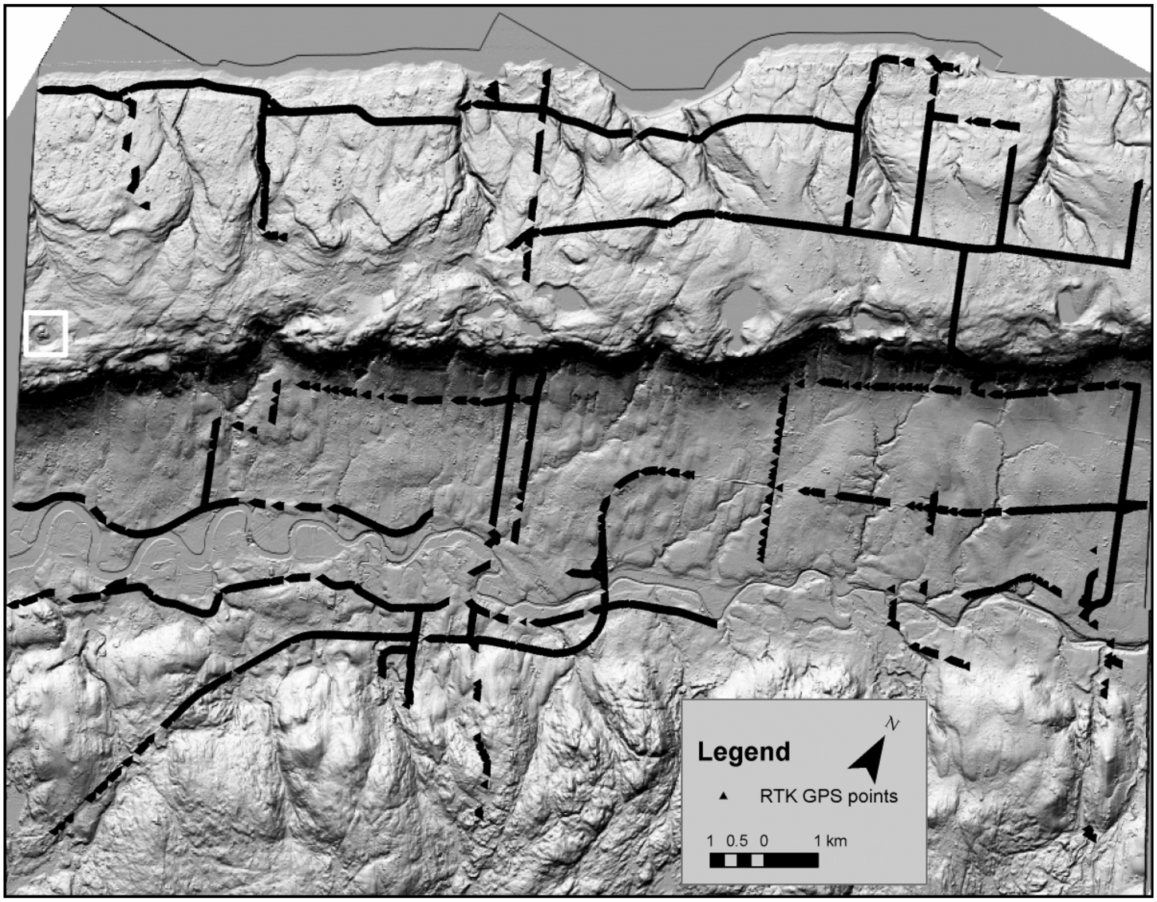

Figure 3.6 RTK GPS points (black triangles) overlaid on a shaded relief image of the LIDAR-derived DEM. The DEM was shaded from 315° at a zenith angle of 45° with a five times vertical exaggeration applied. The white square in the upper left section of the map indicates the location of the ring structure and total station survey under the forest canopy.

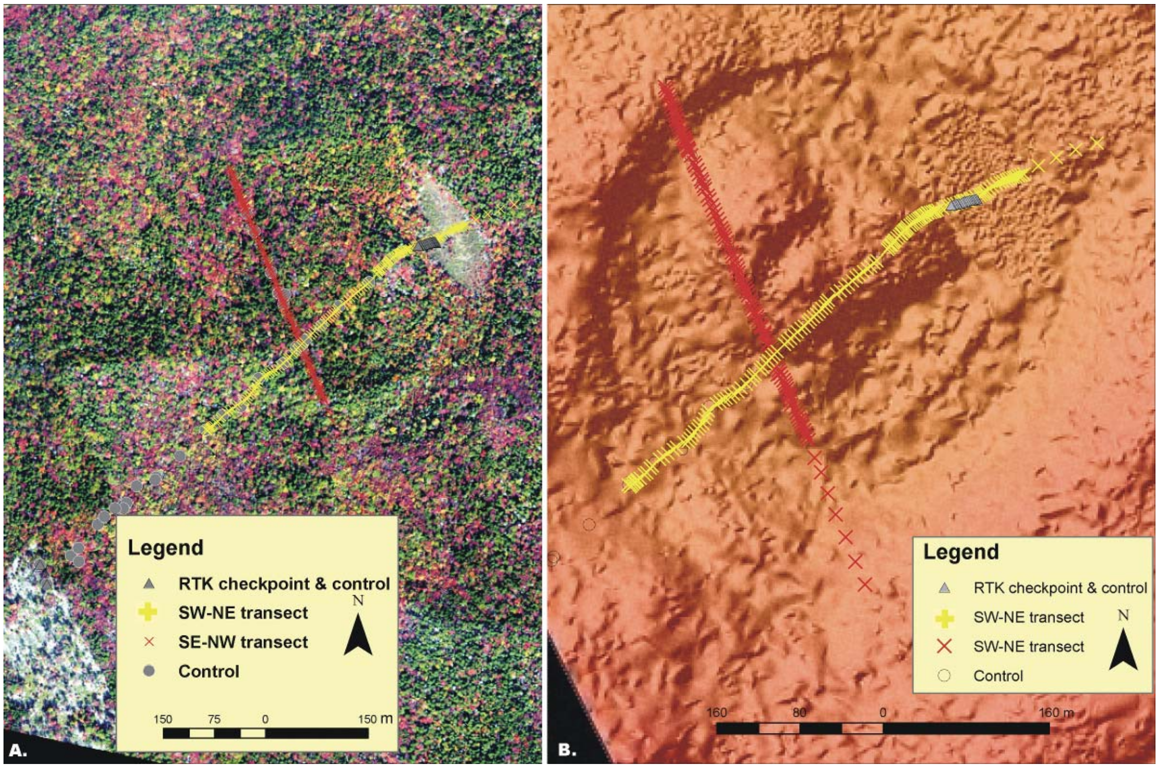

Figure 3.7 Location of the ring structure and transects. The gray triangles represent the GPS control (west in the clear cut) and check data (east in the wetland), other points represent the total station survey data. (A) Mosaic of colour aerial photos taken Oct. 9, 2003, red and yellow denote maple and beech trees and green denotes coniferous trees. White areas highlight a forest clear cut that is present in the lower left corner on the map and a wetland that is present on the right side of the map. These cleared areas allowed for GPS data to be collected and used as control and checkpoints for the total station survey. (B) This is a colour shaded relief map of the “bald-earth’ DEM of the ring structure and associated transect locations at a larger scale than A.

To test these possible sources of height differences, the SW-NE transect survey points were used to extract the original LIDAR ‘ground’ and ‘non-ground’ points using the automated AML procedure. For the ‘ground’ LIDAR points, a 2 m search radius from the survey points was selected in order to obtain points close to the transect, and a 1 m radius was used for the vegetation (‘non-ground’) LIDAR points. These data were plotted along with the LIDAR-derived DEM surface and the total station survey points (Figure 3.8).

For most areas, changes in slope in the LIDAR-derived DEM profile correspond with the occurrence of a ground LIDAR point. In areas where this is not the case, the DEM surface is derived from ground points that are beyond the 2 m radius away from the survey point. The profile near the 500 m distance shows LIDAR ‘ground’ points at the foot of the slope controlling the DEM surface at this location (Figure 3.8). The LIDAR ground points and DEM are approximately 67 cm higher than the survey points in this area (Figure 3.8). This difference between LIDAR ‘ground’ and survey points decreases towards the east, i.e. from the forest and shrubs into the grass covered wetland near the end of the transect where the survey data best matches the LIDAR data (Figures 3.7, 3.8). Based on this observation and field visits, the difference between the LIDAR-derived DEM and that of the survey points for this area is a result of dense shrubs being interpreted as ‘ground’ points.

3.5.2. LIDAR METHOD B VALIDATION

The validation data for LIDAR method B consists of post-processed rapid static GPS data collected in predominantly horizontal grass-covered fields to ensure a sufficient number of LIDAR returns and minimum differences of LIDAR heights within the search radius. A total of 51 GPS points were acquired for this study area (Figure 3.1). The automated validation procedure was used with these GPS points and a 5 m search radius was specified to ensure a sufficient sample of LIDAR points. This radius resulted in 970 ‘ground’ LIDAR points being selected for comparison to the GPS points. The GPS

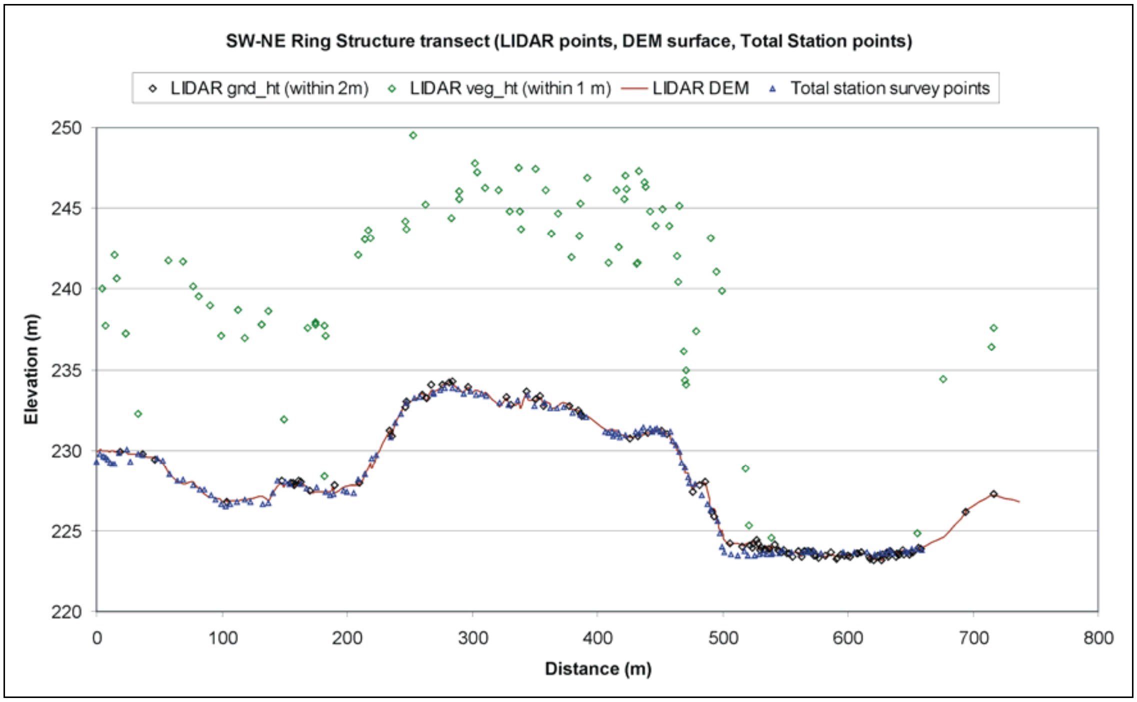

Figure 3.8 Plot of the southwest-northeast trending transect across the ring structure that incorporates the original LIDAR ‘ground’ (black diamonds) and ‘non-ground’ (green diamonds) points as well as the LIDAR DEM surface (red line) and total station survey points (blue triangles). The profile near 500 m indicates LIDAR ‘ground’ points at the foot of the slope are 67 cm to high. This is interpreted to be a result of shrubs that are classified as ‘ground’ points. The survey and LIDAR data agree to the east where short vegetation occurs in the wetland area.

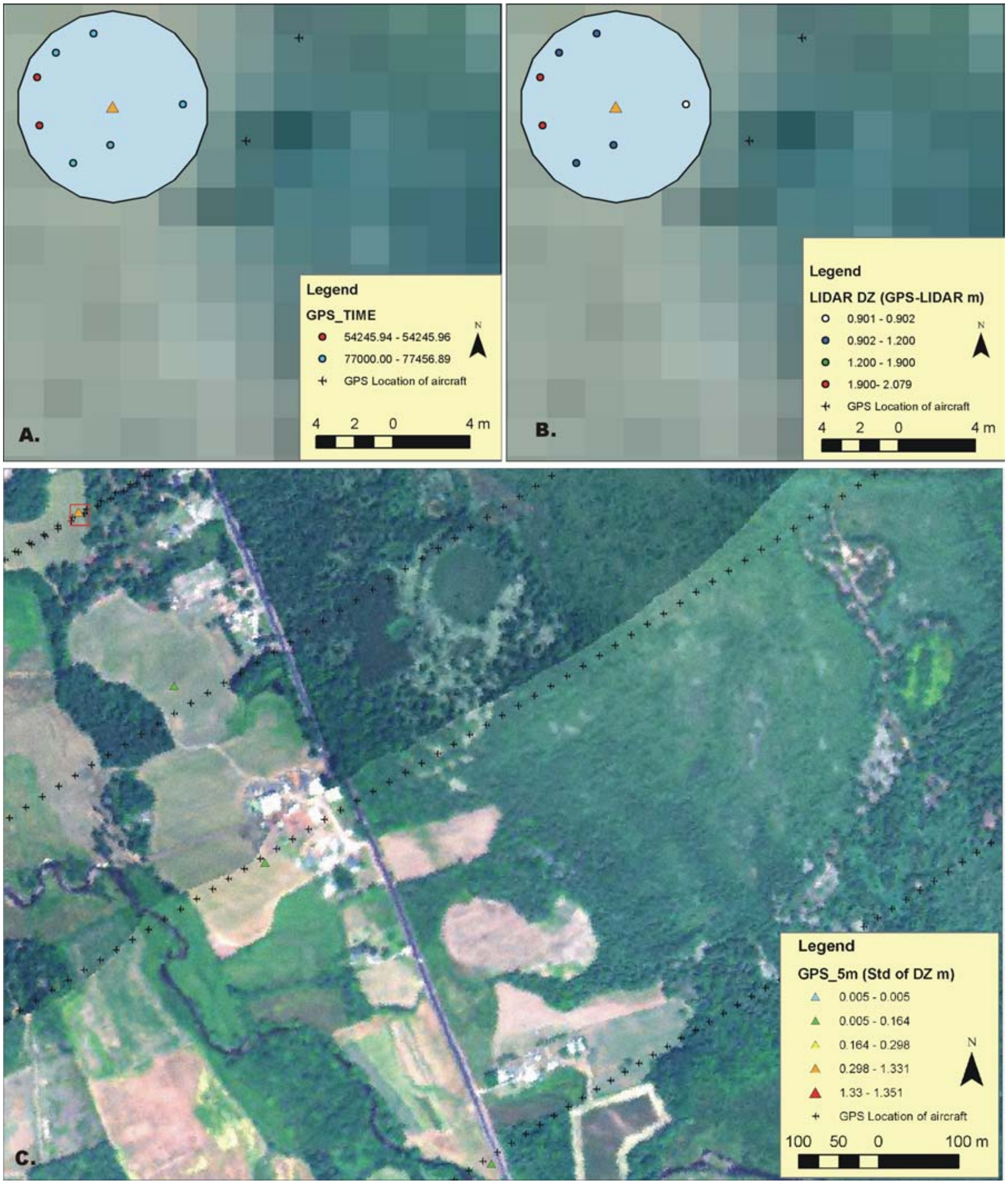

Figure 3.9 (A) LIDAR points colour-coded by GPS time within 5 m of GPS point. The two GPS times correspond to two flight lines. (B) The same LIDAR points colour-coded by Δz magnitude. The range of Δz values is spatially correlated with the GPS time differences or flight lines. (C) Combined map of aircraft flight lines (airplane symbols) and GPS check points. The GPS check points are denoted by triangle and are colour-coded based on the Δ z 1σ.

summary statistics indicate a mean difference in orthometric heights between the LIDAR and validation points of 1.18 m with a standard deviation of 0.64 m and a RMS error of 1.34 m. The summary statistics indicate that these LIDAR data do not meet the vertical specifications.

The ability to examine the GPS Δ *z* standard deviation focuses attention on where the LIDAR data shows significant variance and can be further examined. To investigate the height variation between flight lines, GPS points were colour-coded based on the standard deviation of the Δ *z* value and the positions of the aircraft were plotted (Figure 3.9). The detailed maps (Figure 3.9, A, B) show the LIDAR points within 5 m of the GPS checkpoint with the largest variance (Figure 3.9, C). The LIDAR ground points are colour-coded based on GPS time (Figure 3.9, A) and colour-coded based on the Δ *z* (Figure 3.9, B). The Δ *z* range for one flight line (GPS_Time 54245) is 1.90 – 2.08 m, and the range for the other flight line is 0.9 – 1.18 m (Figure 3.9). It is clear that the magnitude of Δ *z* is related to each flight line defined by GPS time. This is confirmed by examining all 970 of the LIDAR points by plotting Δ *z* against the GPS time for the aircraft (Figure 3.10). As can be seen in this figure, the Δ *z* range and magnitude varies with GPS time or flight line. The source of this error will be discussed in the next section. Without proper LIDAR calibration parameters or extensive ground control, adjustment of individual flight lines to an absolute reference is difficult. Ideally the data provider should carry out such adjustments on the raw LIDAR data prior to the ‘ground/non-ground’ classification and delivery to the end user.

Validation technique 2 was not implemented for these data because of the relative offsets between strips and the sparse distribution of LIDAR points from dark targets. As a result, the derived DEM was considered unreliable and not analyzed further.

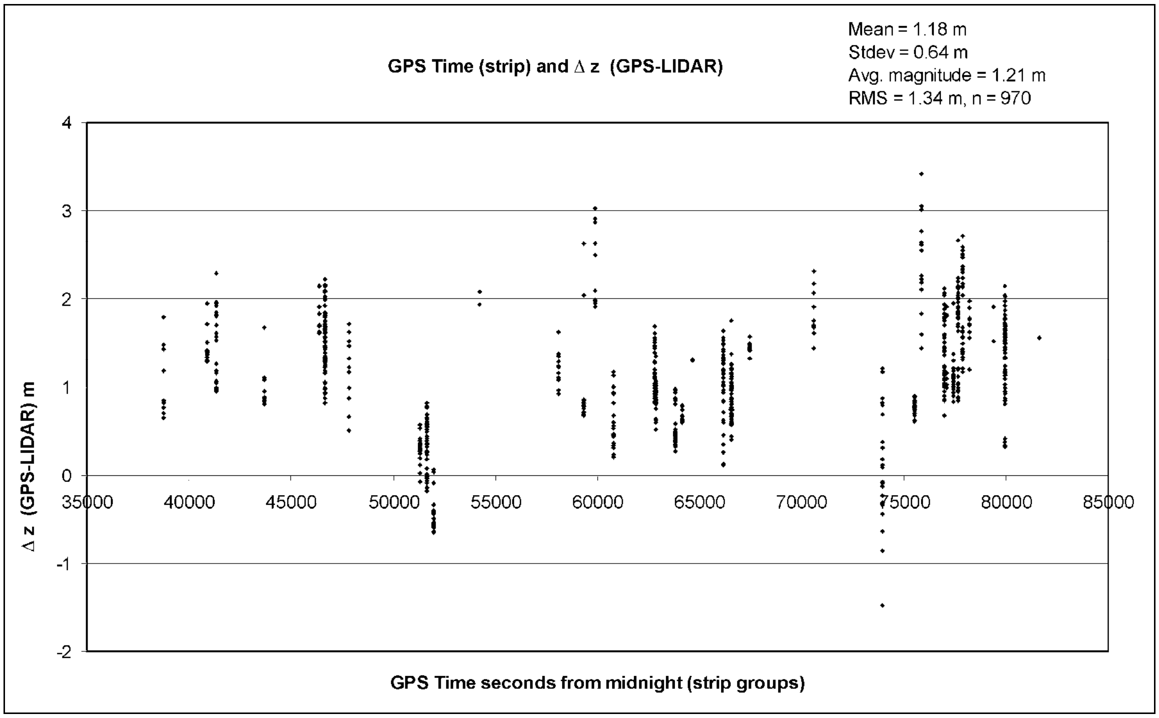

Figure 3.10 Graph of GPS time and Δ z for all 970 LIDAR points within 5 m of the GPS points for LIDAR method B. Note the variability of the range and position of Δ z with respect to the GPS time that corresponds to different flight lines.

3.6. DISCUSSION AND CONCLUSIONS

The results of the vertical accuracy of LIDAR method A in open areas are similar to other findings (e.g. Huising and Gomes Pereira, 1998; Ahokas et al., 2003; Artuso et al. 2003). Although LIDAR method A met the vertical specifications, problems were encountered related to the classification of the LIDAR point cloud into ground and non-ground points along the raised roadbed, thus affecting the validation results when comparing the GPS measurements to the interpolated DEM surface. Steep natural breaks in the terrain such as cliffs and nick points in streams that can have geomorphic significance are problematic in the classification process. The effect of land cover and shrubs on error is consistent with findings from Hodgson and Bresnhan (2004) who quantified the contribution of error from the LIDAR system, interpolation algorithm, terrain slope, land cover, and reference data.

The other issue encountered with this dataset involved the detection of the ground under the forest canopy, where some height errors were as high as 60-70 cm and were attributed to shrubs being classified as ground points. A smaller laser beam footprint may help minimize this problem for single return systems, or if the density of the shrubs is not too great a larger footprint multi-return system may better resolve the true ground position. However, most LIDAR systems that record discrete returns cannot differentiate objects that are less than a few metres apart and record them as a single return. The error of ground elevations under a mixed forest canopy is lower than that reported by Hodgson et al. (2003) which was up to 153 cm for scrub/shrub land cover in leaf-on conditions and similar to that reported by Kraus and Pfeifer (1998) of 57 cm under the canopy. However, the error results are larger than those that reported by Ahokas et al. (2003) that ranged between 24 and 40 cm for a similar flying height in a forested environment.

There were two significant problems with the data from LIDAR method B; the spatial point distribution was sparse for dark targets such as asphalt, and these data did not meet the vertical specifications. Although height variations between strips have been observed in several studies (Huising and Gomes Pereira, 1998; Kraus and Pfeifer, 1998; Crombaghs et al., 2000; Maas 2000, 2002; Ahokas et al., 2003; Elberink et al., 2003;

Kornus and Ruiz, 2003) and have been adjusted using different techniques (block adjustment, TIN surface and least squares adjustment), the objective of this study was to identify the potential errors between strips and report them to the data provider for correction. The application of the automated GIS routine facilitated the identification of the systematic height error observed in these data that was related to each flight line (strip). The LIDAR sensor experienced a power loss at the beginning of the survey and was unable to detect the weaker signals reflected from dark targets. As a result, the original planned survey altitude of 900 m was reduced to approximately 600 m. It was determined that the source of this vertical error was related to a range bias that was not correctly compensated for in the calibration procedures. The LIDAR calibration procedure was done at a flying height of 900 m, however the actual flying height was significantly lower resulting in a range bias. To verify this, appropriate scale factor and offset parameters were applied to the LIDAR data that then more closely matched the validation data.

In conclusion, this study demonstrates the importance of independent detailed validation data in order to ensure the LIDAR data meet the high accuracy specifications. The automated validation technique that compares checkpoints with proximal LIDAR points is useful for identifying systematic errors in the data as well as misclassification of the LIDAR point cloud. The inclusion of the GPS time for each LIDAR point facilitated the investigation of height errors between strips using this automated technique. LIDAR datasets consist of a large number of points and the automated procedure allows a large volume of GPS and LIDAR data to be analyzed quickly within a GIS environment. The combination of analyzing the LIDAR DEM and the LIDAR ‘ground’ and ‘non-ground’ points can lead to a better understanding of the sources of error in LIDAR DEMs in forested areas, as demonstrated in this study by the validation of the ring structure.

3.7. ACKNOWLEDGEMENTS

This study benefited from the contribution of several people. We would like to thank the financial assistance of Brendan Murphy, St. FX University and the Nova Scotia Community College (NSCC) towards Tim Webster's PhD and thesis committee consisting of Brendan Murphy, John Gosse, and Ian Spooner. We would also like to thank the Dennis Kingston and the AGRG students involved in some of the validation data collection: Paul Fraser and Dan Deneau for the 2001 rapid static GPS survey, and Trevor Milne and the students from the AGRG class of 2003-2004 for assisting in the total station survey, and Tim Daly for constructing the aerial photo mosaic. Also, Dan Deneau and Lisa Markham for assisting in writing parts of the AML code for the first validation procedure. Special thanks to Bob Maher and David Colville of the AGRG, and Don Forbes of the Geological Survey of Canada for their support and constructive comments during the project. The LIDAR data for this project was funded by an infrastructure grant to the NSCC from the Canadian Foundation for Innovation, Industry Canada. We would like to thank Bob Maher and anonymous reviewers 3676, 3794, and 3814 for their constructive comments that greatly improved the manuscript.

CHAPTER 4. MAPPING SUBTLE STRUCTURES WITH LIDAR: FLOW UNITS AND PHREATOMAGMATIC ROOTLESS CONES IN THE NORTH MOUNTAIN BASALT, NOVA SCOTIA.

Tim L. Webster

Department of Earth Sciences, Dalhousie University

and

Applied Geomatics Research Group

Centre Of Geographic Sciences, Nova Scotia Community College

50 Elliot Rd. Lawrencetown, NS, B0S 1M0, Canada

J.B. Murphy

Department of Earth Sciences

Saint Francis Xavier University

Antigonish, Nova Scotia, B2G 2W5, Canada

J.C. Gosse

Department of Earth Sciences, Dalhousie University

Edsell Castle Circle, Halifax, NS, B3H 4R2, Canada

4.1. ABSTRACT

LIDAR is an emerging technology to generate high resolution DEMs. Subtle topographical differences among three flow units of the Jurassic North Mountain Basalt (NMB), eastern Canada, are visible on a LIDAR-derived DEM. The boundaries were verified by field mapping and allow a simple projection of the contact planes through the terrain model to provide a 3-D visualization of the flow units. Several ring structures in the lower flow unit, distinguishable only in the LIDAR data, are interpreted to be the remnants of rootless phreomagmatic cones. Glacial erosion has since excavated the highly fractured cone material leaving the more resistant dike and quenched melt to form protruding ring structures. The ability to detect subtle variations in topography using LIDAR may identify previously undetected landscape elements.

4.2. INTRODUCTION

Digital elevation models (DEMs) are used for a variety of geoscience applications at scales ranging from 10^{-1} to 10^{6} m. Some DEMs have been compiled from contours or spot heights derived from traditional photogrammetry. These methods for determining elevations have degraded accuracies in vegetated terrains, where ground elevations are inferred from canopy heights. Other high resolution (m to cm scale) DEMs can be built with ground-based GPS survey equipment, but the coverage area is limited (e.g. individual streams or landforms). The importance of having high resolution DEM data for investigating larger landscapes has been documented in previous investigations. For example, measurements of topographic attributes and hydrograph simulation (Zhang and Montgomery, 1994; Walker and Willgoose, 1999; Schoorl et al., 2000; Kienzle, 2004) or fault rupture length (Haugerud et al., 2003) are strongly dependent on DEM resolution. Increased resolution improves the probability of accurately identifying landforms with subtle relief. Unlike its photographic counterpart, high resolution DEM time series can provide the capacity to remotely monitor slight variations in topography, a powerful geomorphometric tool in the fields of glaciology, seismicity, volcanology, and oceanography.

A new type of elevation data from laser altimetry known as Light Detection and Ranging (LIDAR) provides high-resolution DEMs (ca. 2 m) over large spatial scales. The enhanced spatial resolution of LIDAR facilitates visualization and modeling of surficial features with fewer artifacts than with DEMs based on coarser resolution (Maune, 2001).

Depending on the type and density of trees, LIDAR can penetrate a forest canopy and produce “bald earth” DEMs with 2 m resolution or better and decimetre-level vertical accuracy (Flood and Gutelius, 1997). This is an important advantage over photogrammetry in boreal Canada. LIDAR has been used in a wide variety of applications including flood risk mapping (Webster et al., 2004*a, b*), forestry (Maclean and Krabill, 1986), glaciology (Krabill et al., 1995, 2000; Abdalati and Krabill, 1999) groundwater monitoring (Harding and Berghoff, 2000), identification of tectonic fault scarps and geomorphic features (Haugerud et al., 2003), and investigating landslides (McKean and Roering, 2003).

In this paper, we show that high-resolution LIDAR data from the Fundy Basin in the Annapolis Valley of Nova Scotia significantly improves the precision of bedrock mapping (Figure 4.1). The subtle topographic expressions of the North Mountain Basalt (NMB) flow units visible on the LIDAR-derived DEM provide the basis for mapping their contacts, identifying individual beds within the flow units, and finding and interpreting subtle ring structures within the lower flow unit (LFU) that were previously unrecognized. Although the largest ring structure was previously identified on aerial photographs, it was misinterpreted as a volcanic neck based solely on its geomorphological characteristics (Hudgins, 1960). With the improved resolution of LIDAR data an entire linear sequence of ring structures has been identified. The ring structures are interpreted to be a result of interaction between the partially solidified lava and water based on morphology, petrology, and geochemical data. We compare these Jurassic rings with younger and better understood rings in the Columbia River Basalts (McKee and Stradling, 1970; Hodges, 1978) and Iceland (Thorarinsson, 1953). The results of this study demonstrate the wide applicability of LIDAR to highlight subtle topographic expressions of geological features in densely vegetated regions.

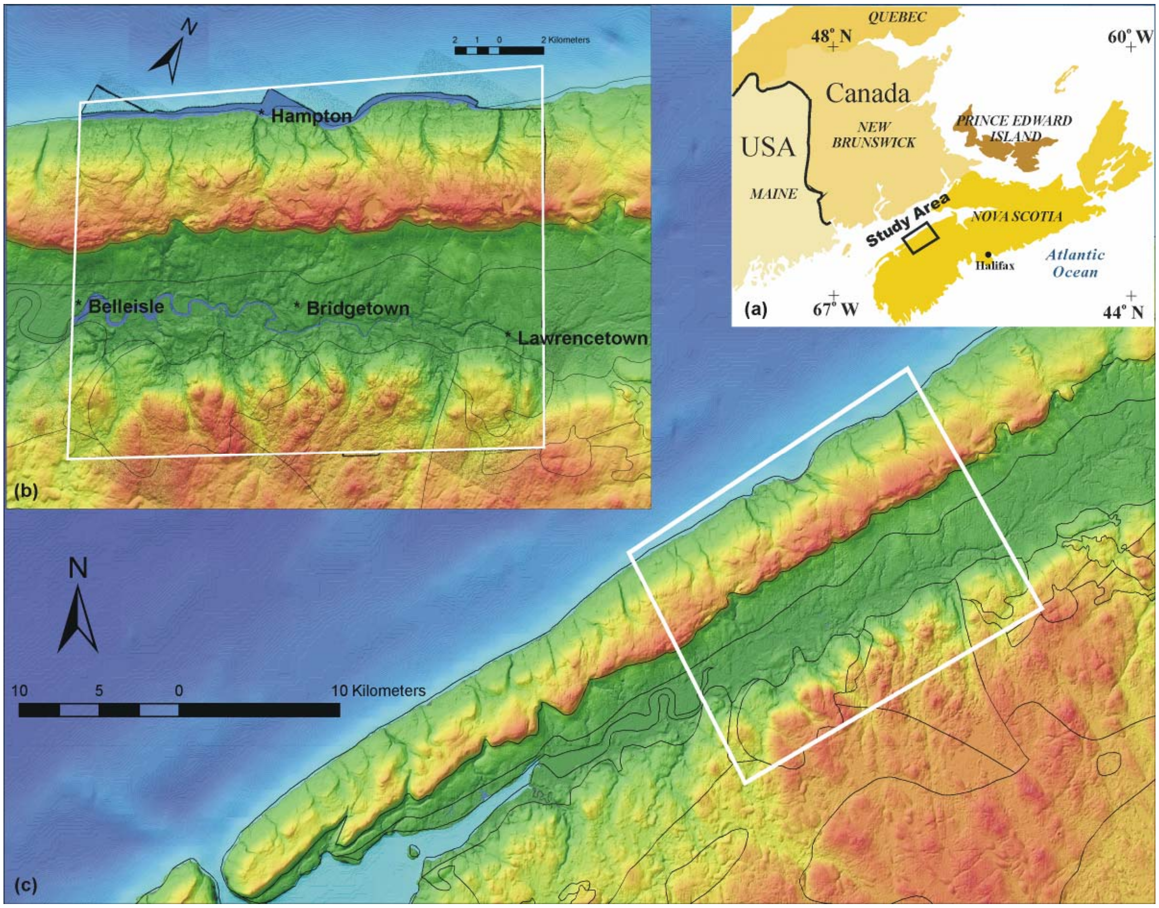

Figure 4.1(A) Study area location within the Fundy Basin of Maritime Canada. (B) LIDAR-derived DEM (white box) with geological boundaries from Keppie (2002) for the detailed study area. See Figure 4.2 for details on the geology. (C) The regional DEM was produced by the Nova Scotia Geomatics Center, Service Nova Scotia & Municipal Relations.

4.3. GEOLOGY OF THE STUDY AREA

The Annapolis Valley lies within the Mesozoic Fundy Basin and is predominantly underlain by Triassic sedimentary rocks (Blomidon and Wolfville formations), flanked by the Jurassic NMB to the north and Paleozoic rocks of the Meguma terrane to the south (Figure 4.2). The Blomidon Formation conformably underlies the NMB and represents a paleoenvironment that alternated between arid and wet conditions, with the climate becoming progressively wetter from the latest Triassic to earliest Jurassic time (Klein, 1962; Nadon and Middleton, 1985; Mertz and Hubert, 1990; Ackermann et al., 1995; Wade et al., 1996). Klein (1962) proposed a lacustrine environment “Lake Blomidon” with fluctuating water levels, implying an elevated water table at the time of the NMB extrusions.

The 202 ± 1 Ma NMB (U/Pb zircon, Hodych and Dunning, 1992) represents the northernmost extent of the Central Atlantic Magmatic Province (CAMP) that is associated with predominantly tholeiitic basaltic magmatism erupted during the early stages of the opening of the Atlantic Ocean (Marzoli et al., 1999). The NMB dips gently to the northwest (Figures 4.1, 4.2), and forms the southeast limb of a regional syncline (Withjack et al., 1995) and is crosscut by north to northeast-trending faults and fractures that exhibit dextral displacement (Olsen and Schlische, 1990; Schlische and Ackermann, 1995). Hudgins (1960) identified several flow units that extend along most of the length of the NMB. Stevens (1980) identified several circular features that occurred along the coast, which he interpreted as possible vents. Kontak (2001) described the internal stratigraphy of the NMB and proposed it be separated into three flow units. The upper flow unit (UFU) outcrops along the shore, consists of 1-2 flows, and is massive and columnar jointed (Figure 4.3). The UFU conformably overlies the middle flow unit (MFU), which consists of multiple thin flows that are highly vesicular and amygdaloidal.

Zeolites are most common in the MFU of the NMB where they occur as amygdules and also in veins, pipes and "bubble trains" (Pe-Piper, 2000) (Figure 4.3). Pe-Piper (2000) and Pe-Piper and Miller (2002) proposed that the zeolites associated with the NMB resulted from the early circulation of hydrothermal fluids and cite evidence from micro-fractures that indicate hydrothermal venting from degassing and an abrupt drop in pressure.

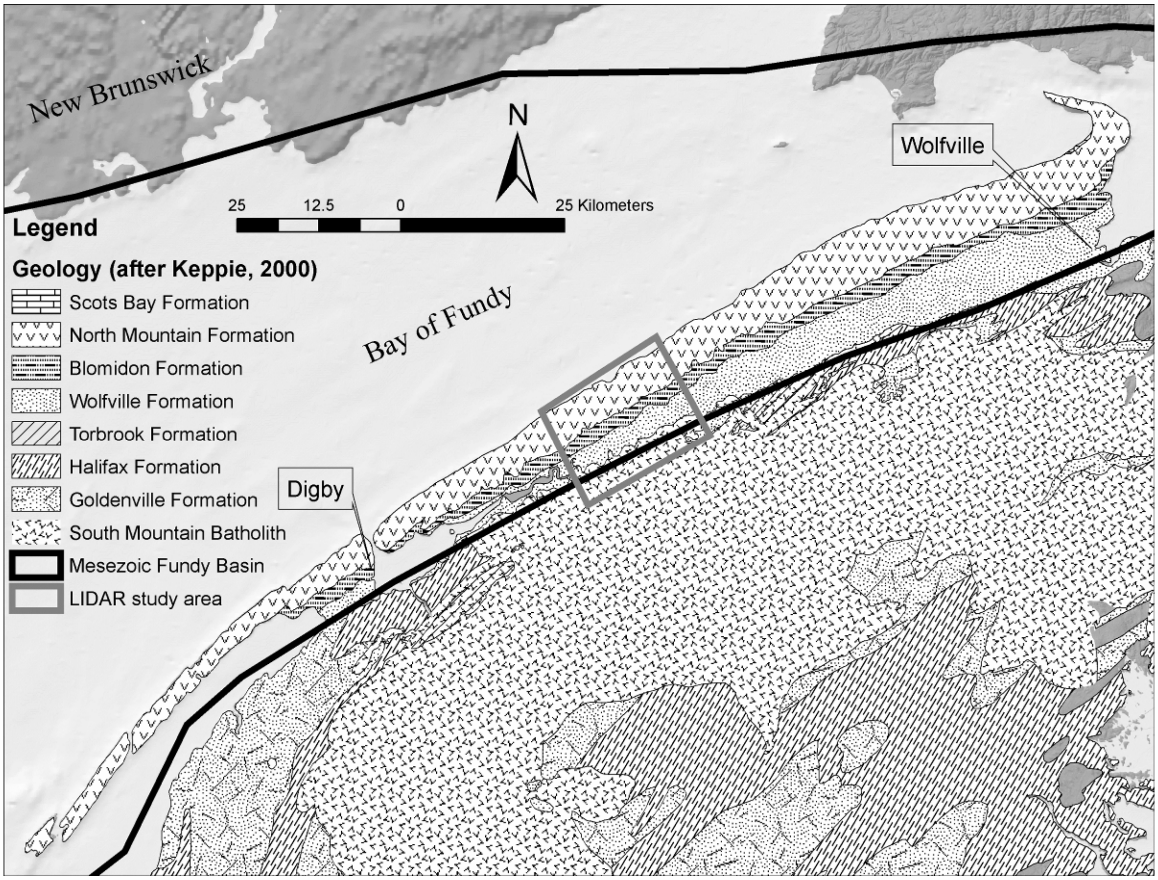

Figure 4.2 Extent of the Fundy Basin (heavy black line) and the regional geology for southwest mainland Nova Scotia (Keppie, 2000). The Jurassic sedimentary rocks of the Wolfville and Blomidon formations in the Annapolis Valley separate the North Mountain Basalt from the South Mountain Batholith to the south. The North Mountain forms a cuesta for the valley (see Figure 4.1).

The MFU conformably overlies the lower flow unit (LFU) that forms the cuesta of the valley and consists of a thick (40 - 150 m) massive single flow (Figure 4.3). There is no evidence of pillows within any of the flow units. The differences in grain size and structure of the flow units produce differential erosion and a topographic expression that has been observed both in the field and on regional elevation models (Kontak, 2001). Geochemical and isotopic data indicate that the basalts have an “oceanic” tholeiitic affinity and their trace elements reveal abundant evidence for crustal contamination, an interpretation consistent with emplacement in the early stages of rifting to form the Atlantic Ocean (e.g. Wark and Clarke, 1980; Dostal and Dupuy, 1984; Papezik et al., 1988; Jones and Mossman 1988; Pe-Piper et al. 1992; Greenough 1995; Kontak et al. 2002). Papezik et al. (1988) and Jones and Mossman (1988) emphasized the elemental and isotopic uniformity in the LFU and UFU along a 170 km strike length.

Based on variations in phenocrysts and flow thickness of the LFU and UFU, Papezik et al. (1988) proposed emplacement of the NMB along a NE-SW fissure with a source near the town of Digby. Dostal and Greenough (1992) proposed that the NMB mafic magma rose to upper crustal levels near Digby, and then intruded toward the northeast along feeder-dike systems before being extruded from a fissure. Kontak et al. (2002) described the LFU and UFU as being dominantly holocrystalline with subhedral to euhedral clinopyroxene and plagioclase, subhedral to anhedral opaque grains. They found mesostatis and interstitial glass present in the UFU (<30%) that were not observed in the LFU. The MFU is distinguished from the LFU and UFU by its coarse to fine grained groundmass and the abundance and nature of the mesostatis (<50%) (Kontak et al., 2002). The variation in grain size and mesostatis is related to the sample’s position in the flow, with coarser grained textures occurring in the interior of the flows. Although they did not find evidence of mesostasis in the LFU, Kontak et al. (2002) did report the presence of mafic pegmatites in the upper part of the massive UFU and LFU and interpreted them to indicate liquid immiscibility developed during extreme fractionation. Although Kontak (2001) and Kontak et al. (2002) confirmed the subdivision of the NMB into three flow units (UFU) based on additional field observations and petrology, the flow boundaries and origin of the circular structures in the LFU proposed earlier have never been verified.

4.4. METHODS

4.4.1. LIDAR TECHNOLOGY

LIDAR is a remote sensing technique used to derive very precise elevation measurements of the earth's surface (Flood and Gutelius, 1997; Wehr and Lohr, 1999). An overview of the components of the LIDAR system used in this study is described in Webster and Dias (in press) and the details of the data specifications are described in Webster (in press). LIDAR systems consist of three components: the Global Positioning System (GPS), an Inertial Measurement Unit (IMU), and the laser ranging system. The GPS is used to map the aircraft trajectory precisely (at cm level) and the IMU is used to measure the attitude of the aircraft (roll, pitch, and yaw or heading). The laser ranging system is used to emit a pulse of coherent radiation, near-infrared in the case of terrestrial

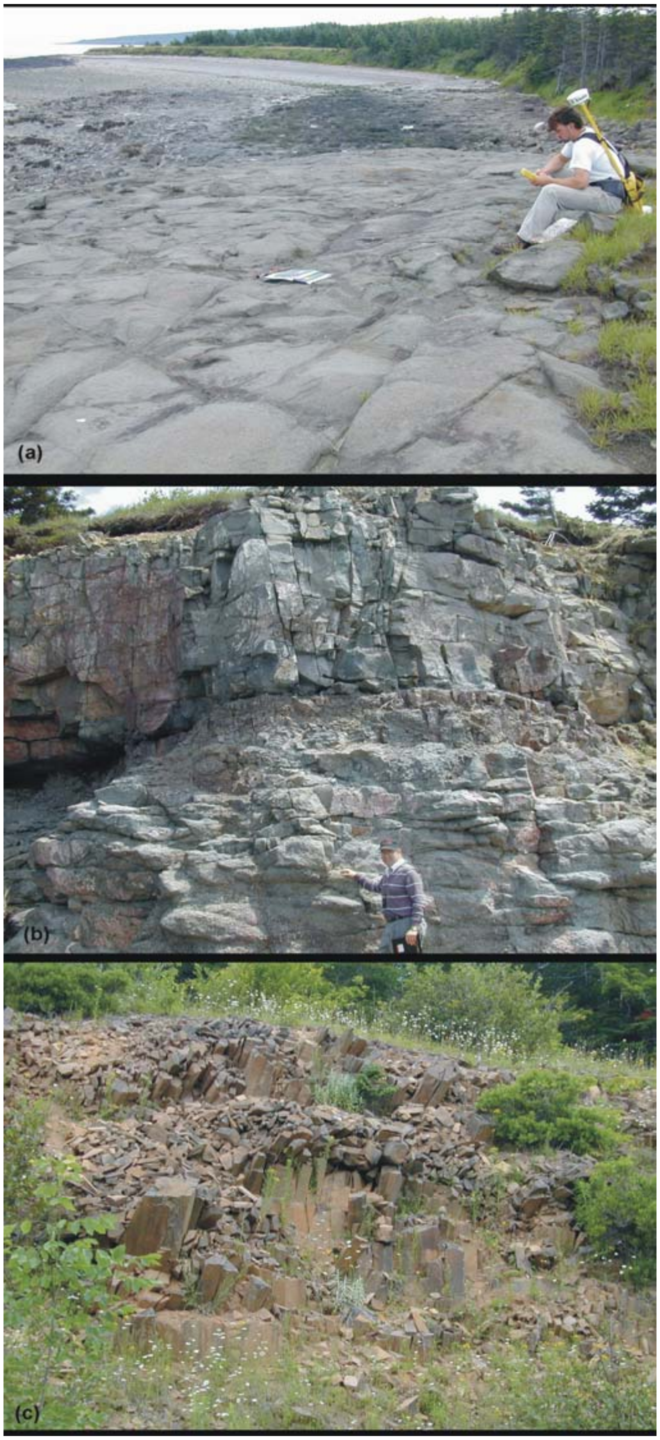

Figure 4.3 Field photographs of the three flow units of the North Mountain Basalt. (A) Upper Flow Unit (UFU) that is comprised of 1-2 massive flows and outcrops along the shore. (B) Middle Flow Unit (MFU) comprised of several amygdaloidal thin flows. (C) Lower Flow Unit (LFU) comprised of a single massive flow with well developed columnar jointing.

LIDAR, toward the earth's surface and measures the travel time of the transmitted and reflected pulse. The Time Interval Meter (TIM) records the laser pulse travel time and converts it into a range based on the speed of light. This range is then adjusted for scan angle and aircraft attitude in combination with the position of the aircraft derived by GPS. The resultant three-dimensional position of each reflected LIDAR pulse is based on the GPS coordinate system (latitude, longitude, and ellipsoidal height using the WGS84 reference ellipsoid). The horizontal coordinate system of the LIDAR points is often transformed into a standard map projection system (e.g. UTM) and the vertical reference is often transformed into orthometric heights above mean sea level. Although the LIDAR survey was conducted during the summer with maximum foliage conditions, the laser system had a narrow beam divergence, resulting in a ground laser footprint diameter of 25 cm, and recorded the last-returning laser pulse, thus increasing the likelihood of getting a range measurement from the ground.

4.4.2. GIS LIDAR PROCESSING

The original LIDAR point cloud, which represents the reflected laser pulses as a cluster of points, was classified into individual points representing measurements of 'ground' features and 'non-ground' features, typically vegetation or buildings. The LIDAR data were analyzed and used to construct surface models in a GIS (see Webster in press for details). All of the LIDAR returns ('ground' and 'non-ground') were used to construct a Digital Surface Model (DSM) of the study area. As the North Mountain is covered with dense forest, the vegetation obscures the morphology of the ground and only gross relief features are visible in the DSM model (Figure 4.4, A, B). However, a "bald earth" DEM can be constructed by interpolating only the 'ground' LIDAR points (Figure 4.4, C). The ability of the laser shots to penetrate the vegetation canopy reveals several subtle geomorphic features compared to that of the traditional 20 m DEM derived from 1:10,000 mass points and contours (Figure 4.4, C, D).

A grey-scale shaded relief map was constructed by illuminating the DEM from the northwest at a zenith angle of 45 degrees and a 5 times vertical exaggeration (Figure 4.5). This map reveals two distinct morphological characteristics of the NMB in this region. The terrain in the western half of the North Mountain study area is characterized by rough topography with abrupt ridges and narrowly incised streams, while the eastern area is characterized by smooth topography with broadly incised streams. This reflects differences in glacial history; areas to the west consist of glacially scoured bedrock with a thin till veneer (TV), and the area to the east has a thick glacial till blanket (TB) (Stea and Kennedy, 1998) (Figure 4.5).

4.4.3. FIELD MAPPING OF NMB FLOW UNITS

As the contacts between the flow units are not exposed everywhere in the study area, previous mapping could not precisely locate them, and so the positions of the contacts were interpolated between outcrops. The relationship between apparent flow unit contacts visible on the LIDAR-derived DEM and the contacts defined by previous mappers (e.g. Hudgins, 1960; Kontak, 2001) was investigated in the field. The topographic features identified by the LIDAR-derived DEM lie in close proximity to the mapped contacts,

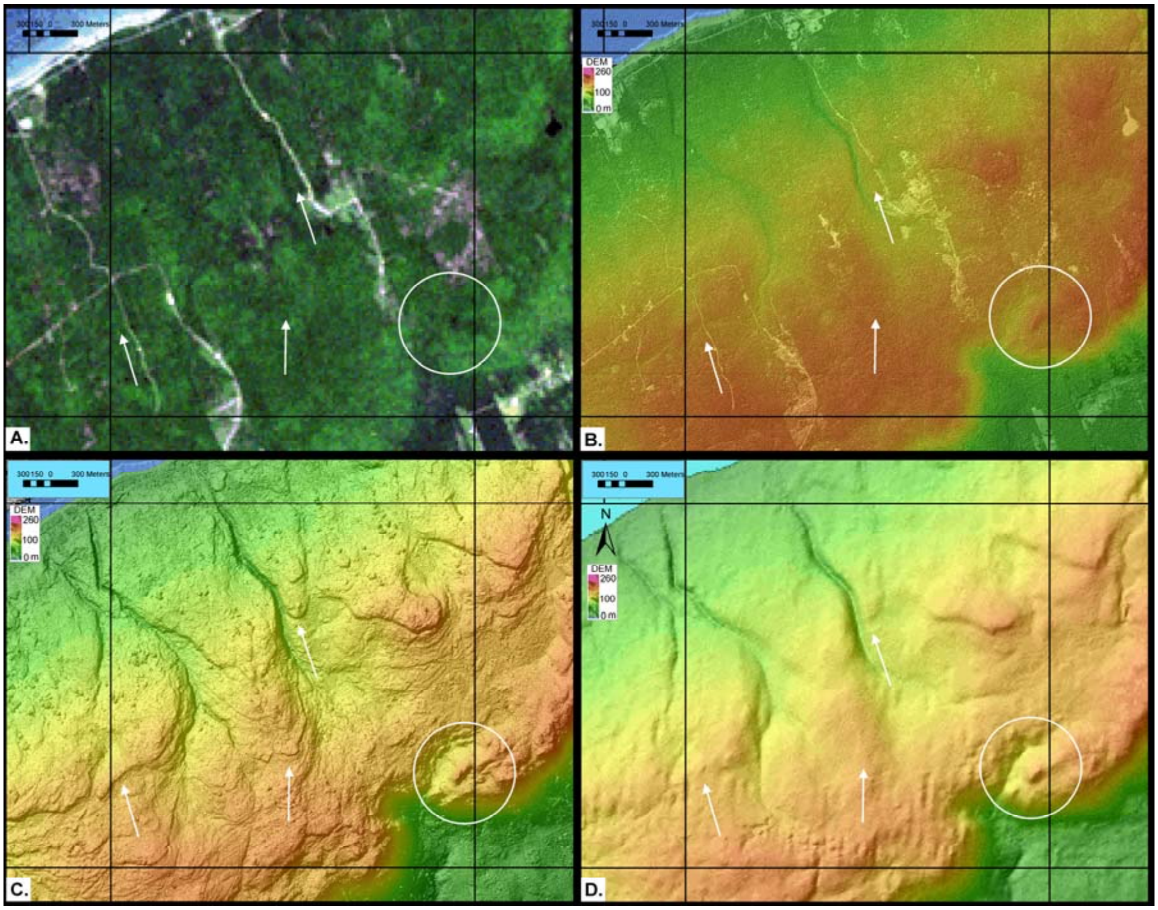

Figure 4.4 Land cover and surfaces constructed from LIDAR data for a 4 km by 4 km tile compared to a regional 20 m DEM. (A) Landsat true colour composite, July 2000 (produced by projecting the reflected Landsat visible wavelength bands through the respective wavelengths for colours red, green, and blue). (B) Digital Surface Model (DSM) interpolated from all LIDAR. (C) "Bald earth" DEM constructed from LIDAR 'ground' points that have penetrated the vegetation canopy; (D) 20 m DEM derived from 1:10,000 mass points and contours. The LIDAR survey was conducted in mid July 2000 with full "leaf-on" conditions. The regional 20 m DEM was produced by the Nova Scotia Geomatics Center, Service Nova Scotia & Municipal Relations. Circled area shows the location of a probable ring structure and arrows denote subtle topographic features associated with the contact between flow units that is only visible in the LIDAR-derived DEM. Ridging artifacts are visible near the lower section of the 4 km by 4 km tiles on the 20 m DEM (D).

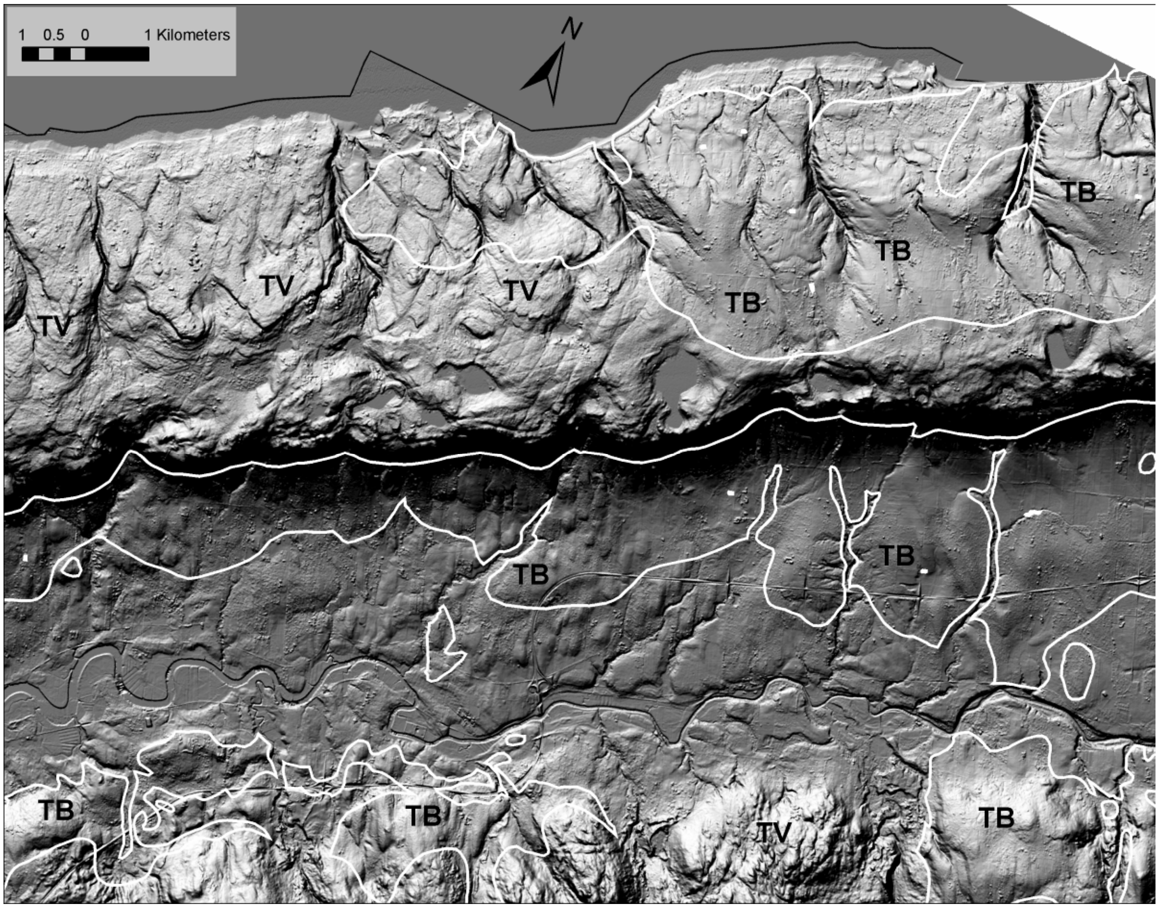

Figure 4.5 LIDAR DEM shaded relief map. The DEM was illuminated from the northwest direction with a 5 times vertical exaggeration and a zenith angle of 45^{o}. The white lines represent the Lawrencetown till unit surficial geology boundary after Stea and Kennedy (1998). TV – thin till veneer, TB – thick till blanket. The terrain has a rougher texture for the TV areas of the North Mountain compared to the smoother texture for the TB areas in the east.

suggesting that the contacts of the MFU with LFU and UFU have distinct topographic signatures that are clearly visible on the LIDAR-derived DEM (Figure 4.6). The data further suggest that the thin amygdaloidal flows of the MFU are less resistant to erosion than either the LFU or UFU.

4.4.4. DEM COMPARISONS OF TOPOGRAPHICALLY DERIVED BASALT CONTACTS

Contacts between flow units (based on the standard 3-point problem from selected outcrop locations) were extracted from the LIDAR-derived DEM and the 1:10,000 scale 20-m DEM. For each DEM, the contact position has been interpreted by combining data from outcrops with (i) manual interpretation of the grey-scale and colour shaded relief images and, (ii) by constructing planes in a GIS environment that represent the contacts between the flow units (based on a regional dip of approximately 6^{o} NW). The mapped outcrops, shaded relief elevation model, and flow unit contact planes were visualized in perspective view to determine where the contact planes intersect the surface.

In order to quantify the relief associated with the contact between the UFU and the MFU, and to compare the sensitivity of the DEMs, detailed GPS transects were measured across the contact at three locations (Figure 4.6). The 20 m resolution DEM derived from the 1:10,000 Nova Scotia Topographic Database (NSTDB) has a vertical accuracy of 2.5 m (Nova Scotia's Geographic Information Standards, HTTP://WWW.GOV.NS.CA/SNSMR/LAND/PROGRAMS/POST/MANUAL/DEFAULT.ASP). This DEM suffers from many artifacts including "ridging" (e.g. Brown and Bara, 1994) and erroneously labeled contour lines (which have been corrected in the study area by re-interpolation of correctly coded contours). The ridging artifacts, however have not been addressed, as they are too numerous.

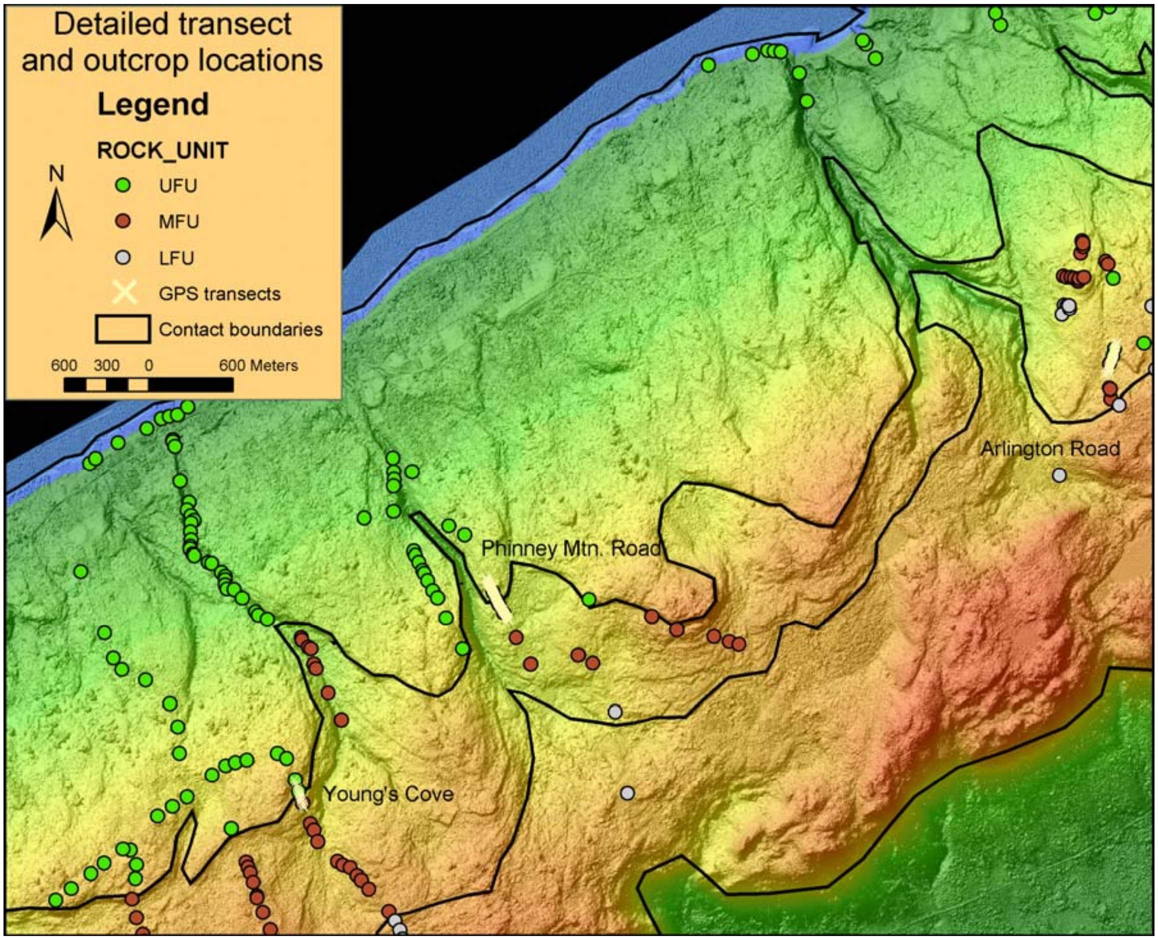

Figure 4.6 Location map of three detailed high precision GPS transects (white crosses) to quantify the relief of the contact between the UFU and MFU. Outcrop locations are colour-coded by flow unit type based on field observations. The background map is the colour shade relief LIDAR DEM. The geological boundaries (black lines) between the flow units are interpreted from field observations and the LIDAR DEM.

For the latitude of the study area (45^o north), the Canadian Digital Elevation Data (CDED) DEMs derived from 1:50,000 and 1:250,000 topographic maps (Natural Resources Canada, http://www.cits.nrcan.gc.ca) have a grid size of 0.75 and 3 arc seconds respectively. Each CDED DEM was converted into the UTM map projection using NAD83 and resampled to a square cell of 20 m and 80 m for the 1:50,000 and 1:250,000 scales respectively. The vertical accuracy reported for these two DEMs is 20 m and 100 m for 90% of the data respectively (http://www.cits.nrcan.gc.ca/cit/servlet/CIT/site_id=01&page_id=1-005-002-002.html).

A high precision GPS topographic survey of the contact between the UFU and MFU was conducted to quantify the relief at three locations: Young's Cove Road, Phinney Mountain Road, and Arlington Road (Figure 4.6). A Leica real-time kinematic GPS system was used to survey transects across the contact boundary. The precision (1σ) of the GPS height measurements was better than 5 cm. The GPS points were brought into the GIS environment and compared to the LIDAR-derived DEM, the provincial 20-m DEM, and the CDED 1:50,000 and 1:250,000 data.

4.4.5. CHARACTERIZATION AND SAMPLING OF THE BASALTIC "RING STRUCTURES"

Hudgins (1960) and Stevens (1980) speculated that circular structures identified along the shoreline in the UFU might represent source vents for the NMB. In this study, several additional ring structures were identified in the LFU based on the LIDAR-derived DEM. Two transects across two of these structures were sampled in order to compare the rocks in the vicinity of these structures with the typical features that characterize the flow units. Rock samples were collected, examined petrographically, and analyzed for major and selected trace elements by X-Ray Fluorescence at the Nova Scotia Regional Geochemical Centre at St. Mary's University. Analytical methods are given in Greenough and Dostal (1992). Representative minerals were analyzed with an electron microprobe at Dalhousie University using a JOEL 733 Superprobe. Topographic profiles were generated across the structures from the LIDAR-derived DEM re-sampled to 4 m resolution. The 4 m DEM reduced disk space requirements and improved processing speed without a significant reduction in detail and quality.

As similar ring structures have been observed in the Columbia River Basalts in Washington State near Odessa (see McKee and Stradling, 1970; Hodges, 1978), a 30 m DEM and a 2 m black and white orthophoto was obtained for the Odessa area in order to compare the morphologies of the ring structures there to those on the NMB. Such a comparison is particularly appropriate because like the NMB, the Columbia River basalts are tholeiitic, and were emplaced into a continental environment undergoing active rifting (Macdougall, 1988; Martin, 1989; Hooper, 1997).

4.5. RESULTS

4.5.1. DEM SENSITIVITY OF FLOW UNIT CONTACTS

The boundaries of the three flow units of the NMB are visible on the LIDAR-derived DEM (Figure 4.6), and their locations were confirmed with field observations along key sections. The relief of the contact between the UFU and MFU is on the order of 2-3 m, consistent with field observations. A ridge characterizes the contact between these flow units, suggesting the UFU has a higher resistance to erosion. The results of the comparison of the GPS survey to elevations obtained from the LIDAR-derived DEM and conventional DEMs clearly demonstrate that only the LIDAR-derived DEM has the precision required to capture this subtle topographic feature that characterizes the geological contact (Figure 4.7). The topographic profile in Figure 4.7A represents a transect along Arlington Road (Figure 4.6) which crosses the contact between UFU and MFU. The relief of the contact is ca. 3 m and the LIDAR-derived DEM matches the GPS data very well, whereas the 1:10,000 20-m DEM does not capture the details of the contact location, and the profiles from the CDED 1:50,000 and 1:250,000 scale maps poorly represent the ridge. The topographic profile (Figure 4.7, B) represents a transect across the UFU-MFU contact along Phinney Mountain Road (Figure 4.6). The relief of the contact is ca. 7 m and again the LIDAR-derived DEM closely matches the GPS data. The 1:10,000 20-m DEM profile shows variable relief of about 2 m spread over twice the horizontal distance of the contact slope. Profiles from the CDED 1:50,000 and 1:250,000 scale maps show a steady increase in elevation along the transect and neither capture the slope of the contact accurately. These results highlight the subtle relief associated with the contact between the UFU and MFU and the ability of the LIDAR-derived DEM to represent it.

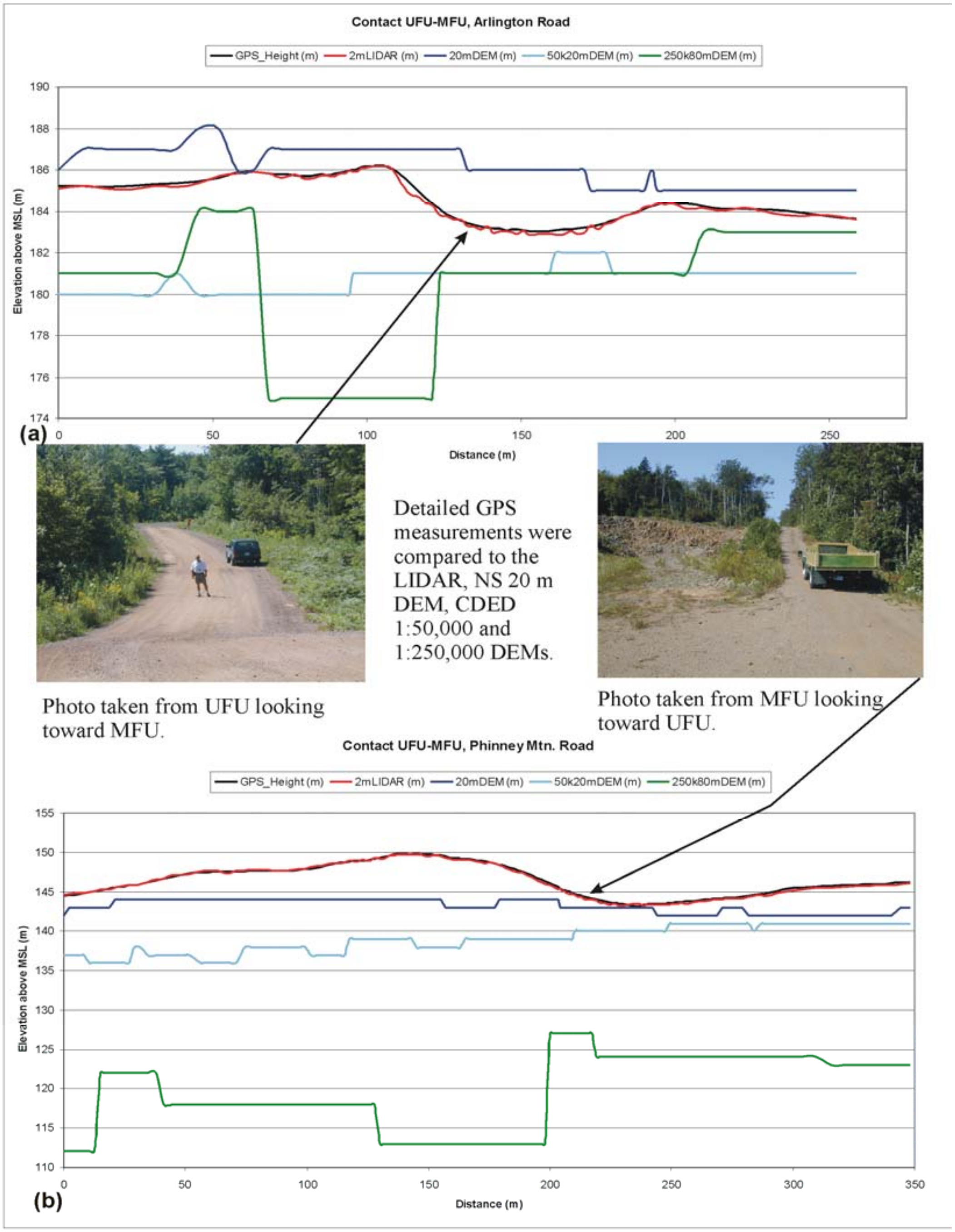

Detailed GPS measurements were compared to the LIDAR, NS 20 m DEM, CDED 1:50,000 and 1:250,000 DEMs.

Photo taken from UFU looking toward MFU.

Photo taken from MFU looking toward UFU.

Figure 4.7 (A) Detailed GPS transects of the contact between the UFU and MFU for Arlington Road. (B) Detailed GPS transects of the contact between the UFU and MFU for Phinney Mountain Road (see Figure 4.6 for location). The topographic profiles consist of GPS points (solid black), LIDAR-derived DEM (red), regional 1:10,000 20 m DEM (dark blue), CDED 1:50,000 20 m DEM (light blue), and CDED 1:250,000 80m DEM (green). The photo insets depict the subtle relief associated with the contact between the UFU and MFU in the field.

The LIDAR-derived DEM and 20-m provincial DEM were combined with data from key outcrops to automatically extract the contact between the flow units along the entire NMB. Although both DEMs produced similar results (with local variations), because of the influence of the till blanket on the local topography, the algorithm tends to fit the contact correctly in one area (the till veneer), but incorrectly in other areas (such as the till blanket area). Therefore a combined approach using the field observations, contact morphologies visible on the LIDAR-derived DEM, and the projected flow unit contact planes were used to define the boundaries between flow units.

The boundary between the UFU and MFU is readily defined and individual flows within the MFU are visible as a series of steps on the LIDAR-derived DEM in the till veneer area to the west. The contact between the MFU and LFU is less well defined, probably because it is located near the headwaters of the drainage systems, and so has suffered less erosion. Distinctions in the field between the two flow units (MFU and LFU) were primarily based on the amount of vesicles and amygdules present in the outcrop (Kontak, 1999, 2002).

The boundary between the three flow units is obscured by the till blanket to the east (Figure 4.5). Well-constrained locations of the contacts between the flow units were used to construct contact planes between the units dipping at ca. 6^{o} toward the northwest. These planes were projected onto the terrain surface along with the outcrop locations colour-coded by flow unit type (Figure 4.8). This type of data visualization quickly allows an assessment of the complexity and consistency of the geological structures across the study area. In this case, the projections of contact planes are consistent with the mapped outcrops and the simple geological structure of the region. The intersection of the contact planes with the terrain was used to assist in defining the contact location, especially in the eastern area where the topography was affected by the till blanket. A new bedrock geology map of the three flow units of the NMB was constructed using this technique.

4.5.2. BASALT RING STRUCTURES IN THE LFU

The location of the largest ring structures observed by Hudgins (1960) on aerial photographs is several kilometres away from rings identified in the georeferenced LIDAR DEM and there is no topographic evidence for such a structure at the location he mapped. We attribute this discrepancy to the limited georeferencing control of those photographs and the difficulty of finding the shallow depression in the forest. A sequence of craters has now been identified on the LIDAR-derived DEM shaded relief maps within the LFU (Figure 4.9). The ring structures are positive relief features characterized by outer elevated ridges and a lower interior that sometimes has a higher central core. Two ring structures identified on the LIDAR-derived DEM were investigated in detail (Figure 4.9). The western most ring is the largest in the study area (left white circle, Figure 4.9, C) and the smaller ring structure at Mt. Rose (right white circle, Figure 4.9, C) were studied in detail.

Petrographic examination of samples collected along transects across each ring structure (Figure 4.9) indicate that several contain abundant mesostasis and glass, interpreted by Kontak et al. (2002) to represent a quenched residual melt (Figure 4.10). For example sample 303 across the large ring structure (Figure 4.10, A-C), and three of the samples collected near the smaller ring at Mt. Rose (mr12, mr13 and mr14) (Figure 4.10, D-G) display mesostasis and glass textures. The occurrence of mesostasis and glass has not been observed elsewhere in the LFU (see Kontak et al., 2002), and appears to be restricted to the ring structures.

Although the NMB exhibits remarkably fresh minerals and is uniform in texture and chemistry (e.g. Papezik et al., 1988; Greenough, 1995), in the vicinity of the ring structures secondary minerals typically replace the primary mineralogy and blur primary magmatic trends. Microprobe analysis revealed the presence of epidote indicating low temperature alteration. Altered basalts in the vicinity of the ring structures have lower and more variable SiO_2, Al_2O_3, Na_2O, K_2O and higher CaO (Table 4.1) compared to the restricted range in these elements in the fresh basalts. The effect of alteration on the geochemistry of the basalts is also clearly visible on the geochemical plots (Figure 4.11). Papezik et al. (1988) drew special attention to the elemental ratios in high field strength elements which “remain amazingly constant” over a wide area in the fresh basalts. In the vicinity of the ring structures, however, basalts have higher ratios of Zr/Nb and Nb/Y (Figure 4.11, B) (Table 4.2), consistent with the petrographic evidence that basalts in the vicinity of the ring structures are more altered than the surrounding LFU.

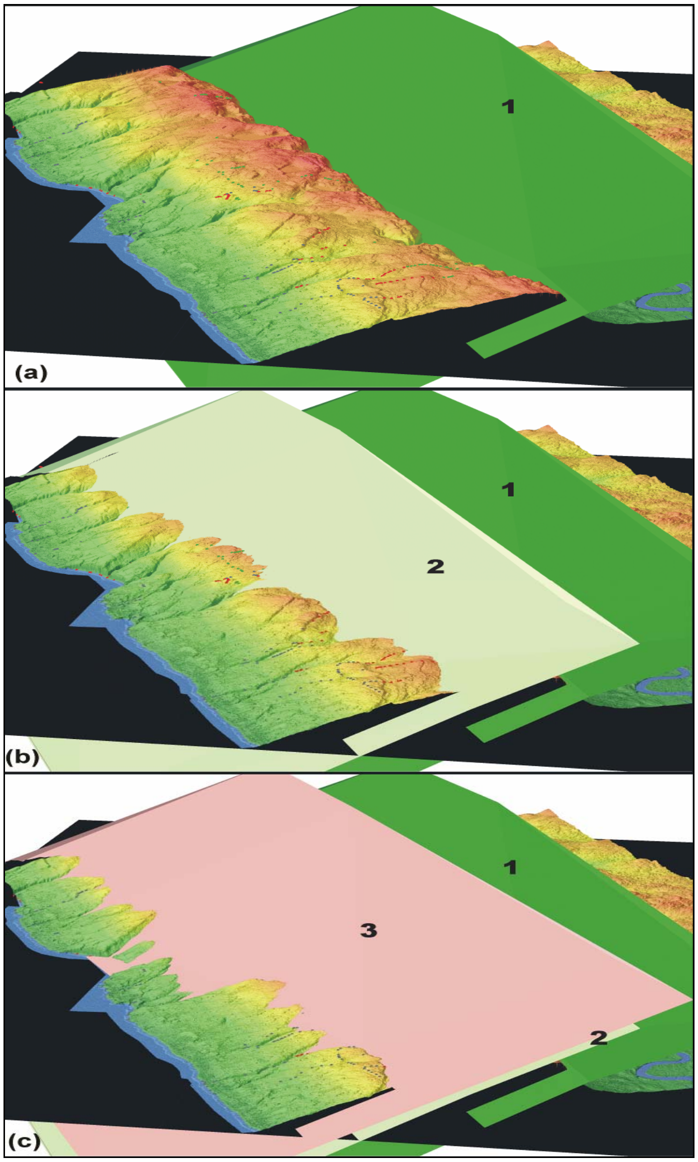

Figure 4.8 Perspective view looking northeast with the contact planes between the flow units projected through the LIDAR-derived DEM surface along with colour-coded outcrop locations of the three flow units (UFU grey points, MFU red points, and LFU green points). The contact planes dip of ca 6^{o} to the northwest and have been constrained by contacts observed in the field. (A) Boundary (1, dark green plane) between the LFU and the Blomidon Formation. (B) The lower contact (1, dark green plane) of the LFU and the upper contact with the MFU (2, light green plane). (C) The upper contact of the MFU (2, light green plane) with the UFU (3, pink plane). Numbers denote the base of flow units: 1 – base of LFU; 2 base of MFU; and 3 – base of UFU. The upper contact of the UFU does not outcrop in this area and is thus unconstrained.

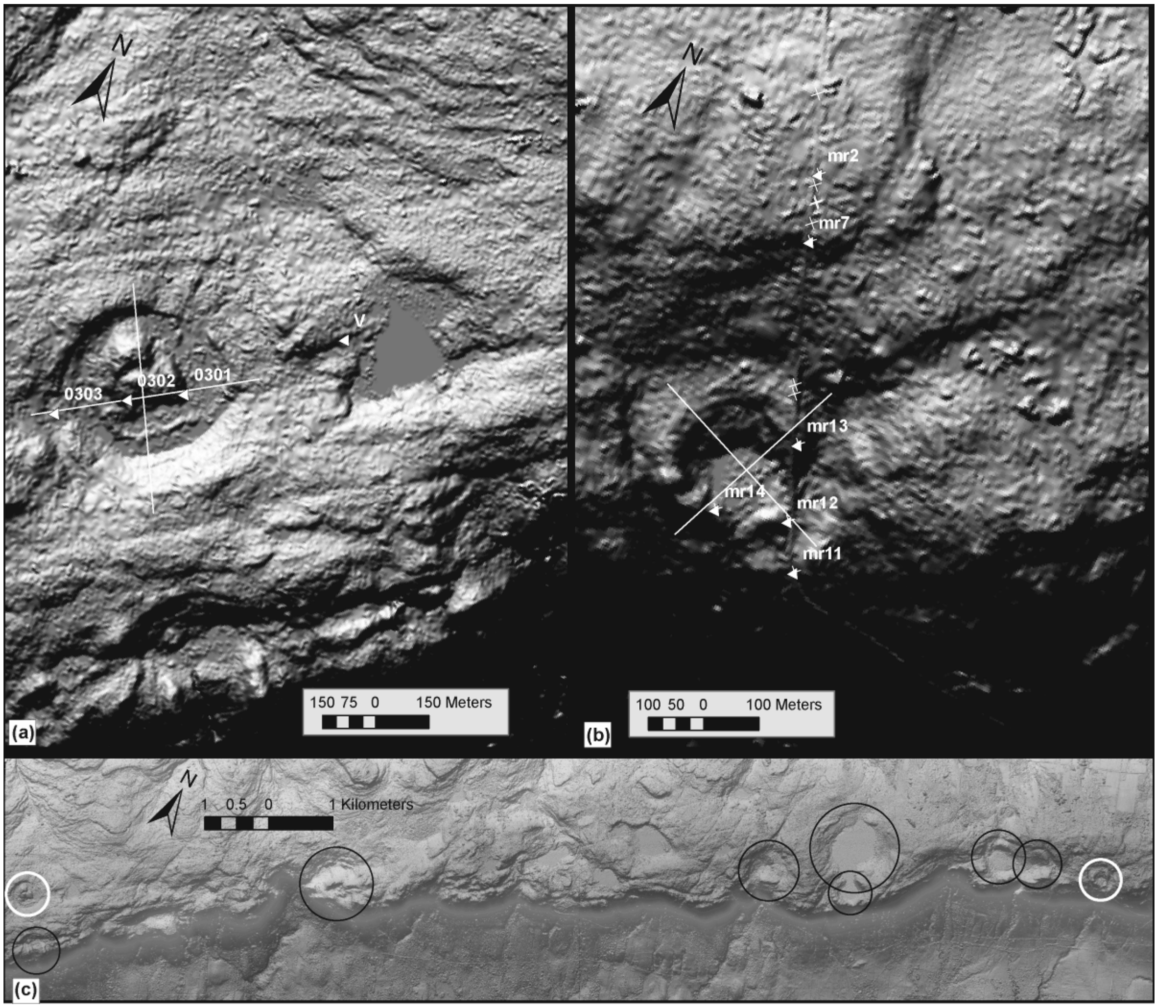

Figure 4.9 Ring structures identified on the LIDAR-derived DEM maps. (A) Shaded relief image showing the large western ring structure, profile locations, and samples 0301, 0302, 0302 and V have been analyzed. (B) Shaded relief image showing the smaller eastern ring structure, profile locations, and samples mr2, mr7, mr11, mr12, mr13, and mr14 have been analyzed. (C) Shaded relief of LIDAR DEM with black circles denoting the linear sequence of ring structures and white circles highlighting ring structures where rock samples have been analyzed (A and B).

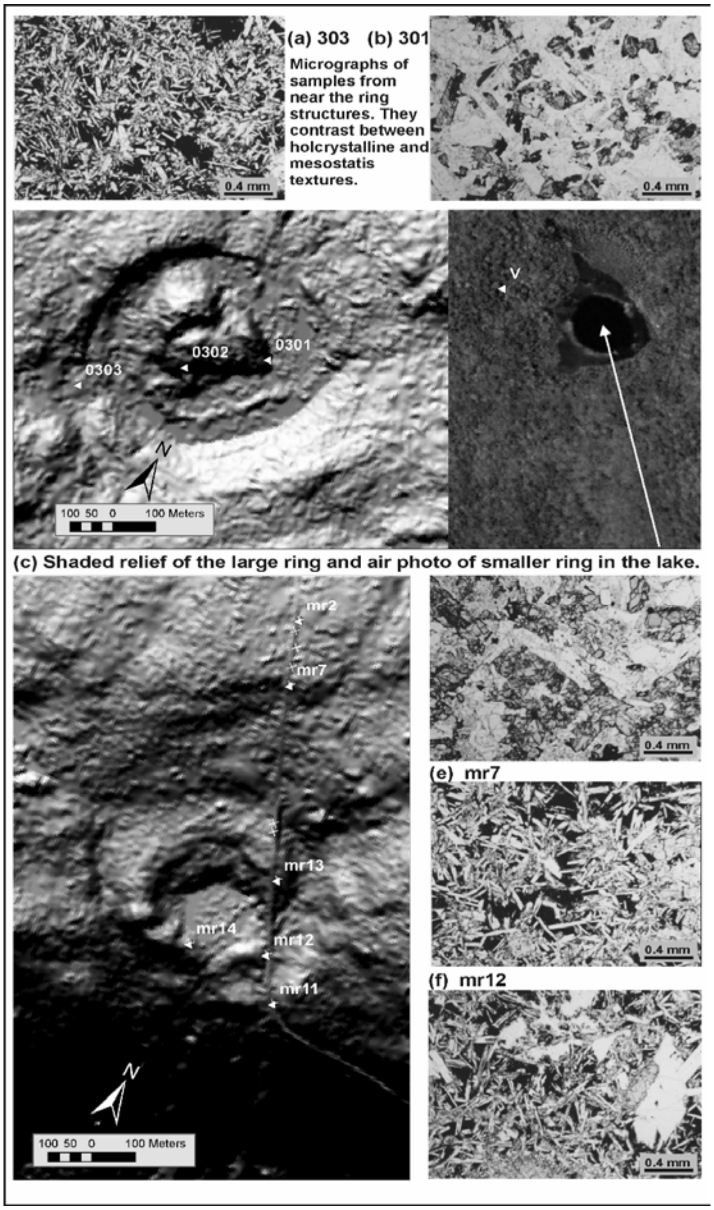

Figure 4.10 Petrographic analyses of samples collected near the ring structures of the NMB. (A) Sample 303 (plane polarized light, PPL) micrograph with abundant mesostasis resulting from a quenched residual melt. (B) Sample 301 (PPL) with holocrystalline mineral phases and subhedral opaque minerals. (C) Shaded relief image of LIDAR-derived DEM (left side) and air photo (right side) of the large ring area with sample locations. Note the smaller circular ring structure that is visible on the air photo (arrow). (D) Shaded relief image of LIDAR-derived DEM of the smaller ring structure near Mt. Rose with sample locations. (E) Sample mr7 (PPL) with holocrystalline mineral phases and subhedral opaque minerals. (F) Sample mr12 (PPL) with abundant mesostasis and opaque minerals. (G) Sample mr14 (PPL) with abundant mesostasis resulting and opaque minerals.

Table 4.1 Major element composition for samples near the ring structures and average composition of the LFU (taken from Greenough, 1995). Sample number and petrographic texture listed from this study. Note Fe2O3 computed from FeO + 1.1 x Fe2O3 as taken from Greenough (1995). LOI column for samples from this study also denotes the number of samples used to calculate the averages taken from Greenough (1995).

SAMPLE	L.O.I. % and number of samples	SiO2 %	TiO2 %	Al2O3 %	Fe2O3 %	MnO %	MgO %	CaO %	Na2O %	K2O %	P2O5 %	Totals
MR-2 holocrystalline	0.90	52.85	1.014	12.84	11.08	0.17	8.27	10.37	1.78	0.65	0.12	100.05
MR-7 holocrystalline	0.80	52.24	1.010	12.87	10.85	0.17	8.22	10.39	1.80	0.68	0.12	99.16
MR-11holocrystalline	0.40	52.05	0.956	12.46	10.41	0.16	8.93	11.26	1.67	0.55	0.11	98.96
MR-12 mesostatis	0.60	52.66	1.075	12.78	10.88	0.16	8.35	11.20	1.76	0.54	0.12	100.14
MR-13 mesostatis	1.00	52.02	1.133	12.84	10.89	0.18	7.94	10.68	1.82	0.70	0.13	99.34
MR-14 mesostatis	0.80	51.95	1.019	13.13	10.30	0.18	8.35	11.34	1.82	0.39	0.12	99.41
301 holocrystalline	1.59	52.24	1.319	14.16	11.64	0.15	5.41	9.39	2.26	0.97	0.15	99.29
302 holocrystalline	1.30	51.77	1.081	12.66	11.14	0.21	7.62	10.38	2	0.86	0.12	99.16
303 mesostatis	1.30	52.02	1.282	14.05	11.54	0.18	6.11	9.16	2.37	1.03	0.15	99.20
V holocrystalline	3.11	52.00	1.190	13.71	11.54	0.17	6.69	9.80	1.97	0.73	0.13	101.05
Avg.LFU_Digby (Greenough 1995)	n=6	53.72	1.080	13.77	10.02	0.16	8.08	10.36	2.06	0.81	0.09	
Avg.LFU_Wolville (Greenough 1995)	n=8	52.96	1.270	15.07	10.49	0.17	7.08	9.93	2.35	0.68	0.13	

Table 4.2 Trace elements for samples near the ring structures and average values or the LFU taken from Greenough (1995).

SAMPLE	V	Cr	Co	Zr	Ba	La	Nd	Ni	Cu	Zn	Ga	Rb	Sr	Y	Nb	Pb	Th	U
	ppm	ppm	ppm	ppm	ppm	ppm	ppm	ppm	ppm	ppm	ppm	ppm	ppm	ppm	ppm	ppm	ppm	ppm
MR-2 holocrystalline	220	276	46	92	176	26	28	63	122	76	15	24	157	21	7	6	4	1
MR-7 holocrystalline	230	312	47	92	146	22	25	75	101	76	16	23	159	21	7	<3	5	1
MR-11 holocrystalline	227	567	46	82	123	28	28	87	97	64	14	19	151	20	6	18	5	1
MR-12 mesostatis	254	512	44	96	143	22	24	85	75	56	15	15	160	22	7	<3	2	<1
MR-13 mesostatis	249	416	47	97	151	19	21	73	98	71	16	19	161	23	8	<3	8	1
MR-14 mesostatis	229	458	48	88	162	9	16	74	111	74	14	19	162	21	8	3	3	<1
301 holocrystalline	265	104	48	118	203	17	21	44	112	70	17	33	175	25	10	<3	4	<1
302 holocrystalline	251	294	49	92	179	29	28	73	<4	82	15	32	151	22	7	<3	2	1
303 mesostatis	276	114	49	114	204	15	17	55	287	99	16	30	172	23	11	<3	5	<1
V holocrystalline	249	124	45	106	151	18	22	57	128	77	16	26	168	23	9	<3	5	1
Avg.LFU_Digby (Greenough 1995)	244	225		96	216			64	100	63	15	24	169	26	9			
Avg.LFU_Wolville (Greenough 1995)	268	178		107	163			60	129	108		16	202	27	12			

4.5.3. COMPARISON TO RING STRUCTURES ELSEWHERE

Ring structures similar to those identified on the NMB (Figure 4.9) occur in the Cenozoic Columbia River Basalts (CRB) of western North America. The CRB craters, with diameters of 50 to 500 m, are characterized by the occurrence of autointrusive basalt dikes that have intruded the sag structures and dip outward away from the center and form circular segments. The CRB basalt dikes are mineralogically and chemically indistinguishable from the surrounding basalt, except for the glassy selvage along the dyke margin. The structures are recognized in aerial photographs near Odessa, Washington State and in cross-section along cliffs where most of the evidence for dike emplacement has been observed (McKee and Stradling, 1970). The late Pleistocene floods from Lake Missoula may have accentuated the arcuate topographic highs produced by the dykes. The craters occur in a flow unit approximately 70-100 m thick, about twice the usual thickness of this flow unit elsewhere (McKee and Stradling, 1970; Hodges, 1978), comparable to the 50 – 60 m in thickness for the LFU of the NMB. The orthophoto for Odessa (Figure 4.12) was merged with a USGS 30-m DEM in order to compare morphologies and scale of the ring structures of the CRB and NMB. The SW-NE profile of the Mt. Rose ring structure of the NMB is comparable in scale to profile number one (Figure 4.12) from the CRB (Figure 4.13, A). The SW-NE profile of the largest ring structure of the NMB is comparable in scale to profile five (Figure 4.12) from the CRB (Figure 4.13, B). The size of the craters is comparable between the two sites at 300 m and 500 m; the relief of the structures is also similar at around 25 m respectively (Figure 4.13).

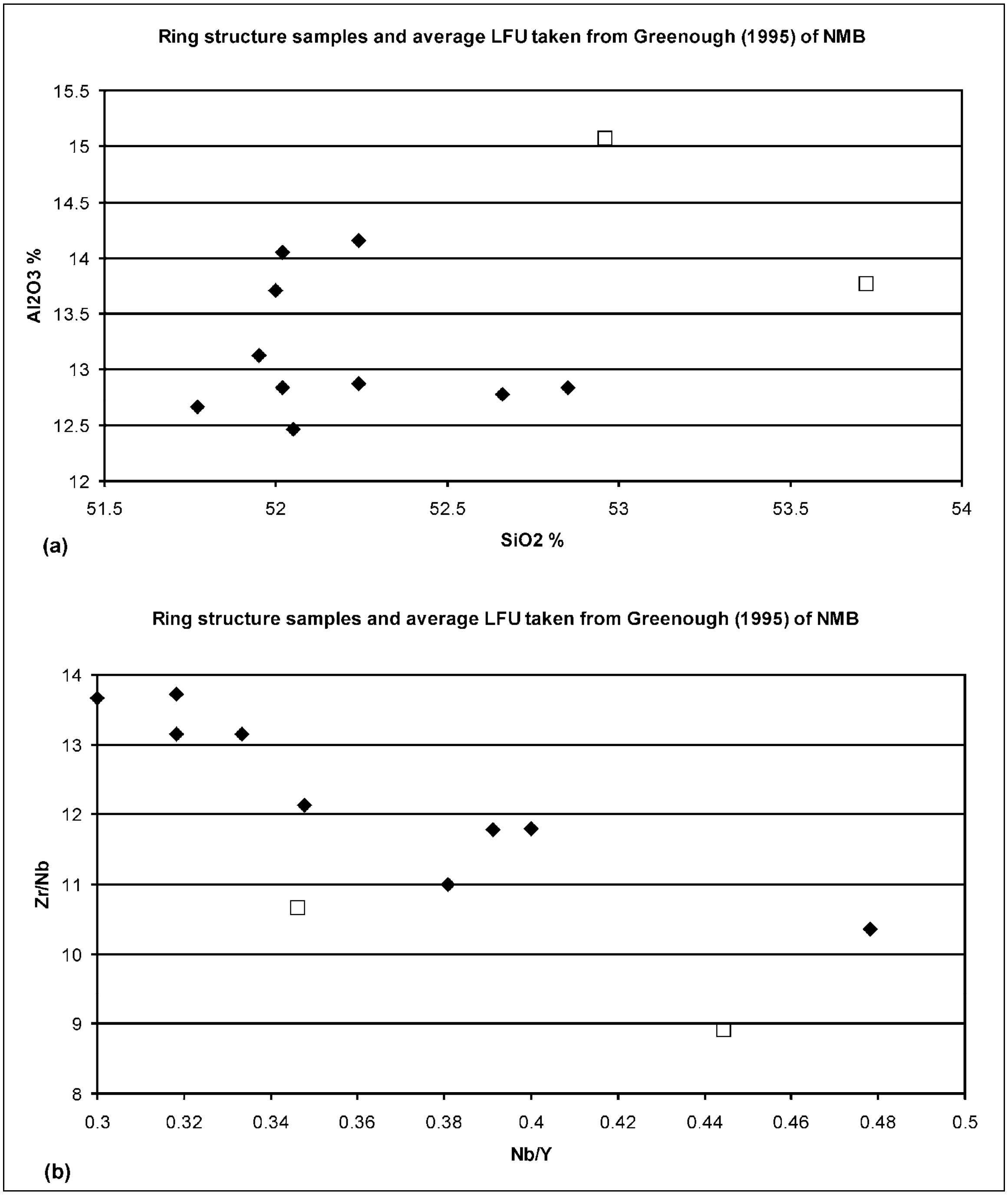

Figure 4.11 Geochemical plots of samples in the vicinity of the ring structures (solid diamonds) compared to those of average fresh samples of the LFU of the NMB (open squares) (taken from Greenough, 1995). (A) Major element scatter plot of weight percent SiO_2 and Al_2O_3. (B) Trace element ratios Zr/Nb and Nb/Y.

4.6. DISCUSSION

4.6.1. ORIGIN OF THE RING STRUCTURES

McKee and Stradling (1970) interpreted the CRB ring structures as sag flowout generated by collapse in a partly solidified flow, in which the sag flowout represents the upward escape of lava from a point source. The top of the flow would sag around the point source, due to loading and withdrawal of support, forming additional fractures that would allow dyke emplacement. They concluded that the flow thickness might be a limiting factor for the formation of these structures and questioned why these types of structures are not more common within the Columbia River flows and in other flows. Hodges (1978) proposed that the CRB ring structures were formed by the interaction of water and partially solidified lava in which a raised water table that intersected the molten lava caused explosive venting, doming and cracking of the partially solidified flow crust. Subsidence of the crust after venting would permit the emplacement of dykes along the concentric fractures.

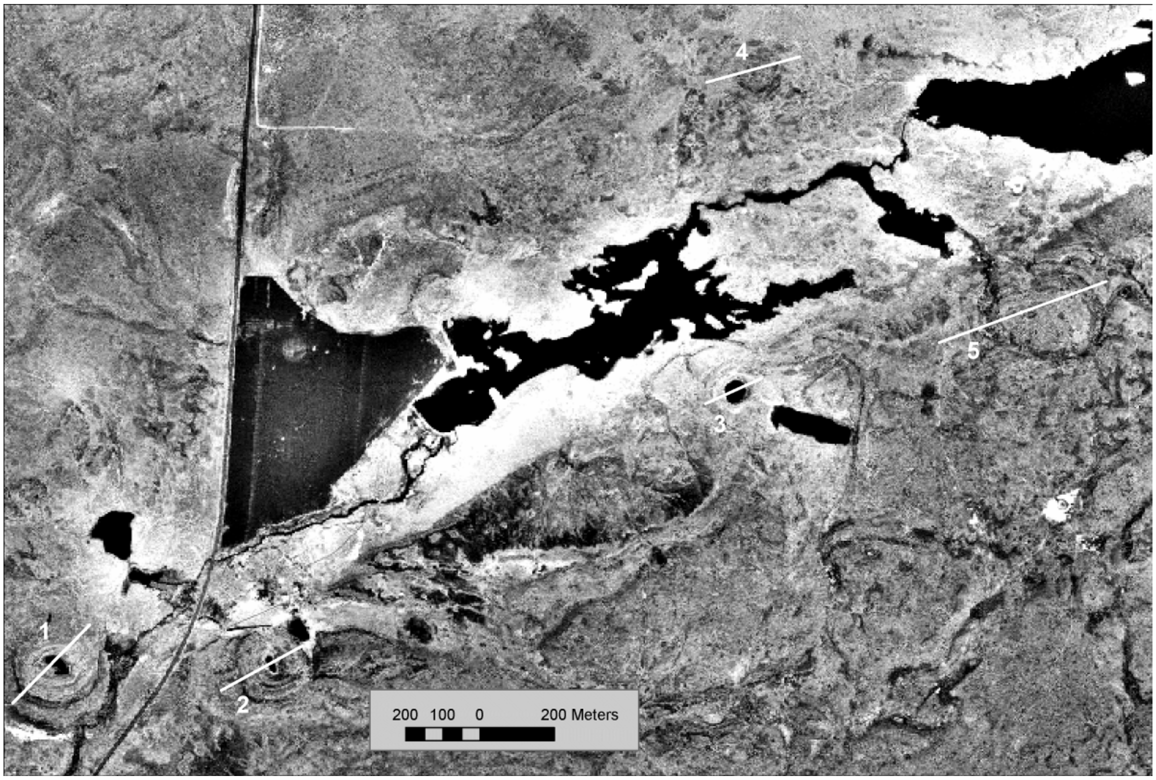

Figure 4.12 Orthophoto of ring structures within the Roza Member of the Columbia River Basalts (CRB) near Odessa, Washington identified by McKee and Stradling (1970) and Hodges (1978). Topographic profiles (white lines and numbers on the map) have been extracted for the ring structures and compared to those obtained for the NMB (see Figure 4.13). Grid north is at the top of the image.

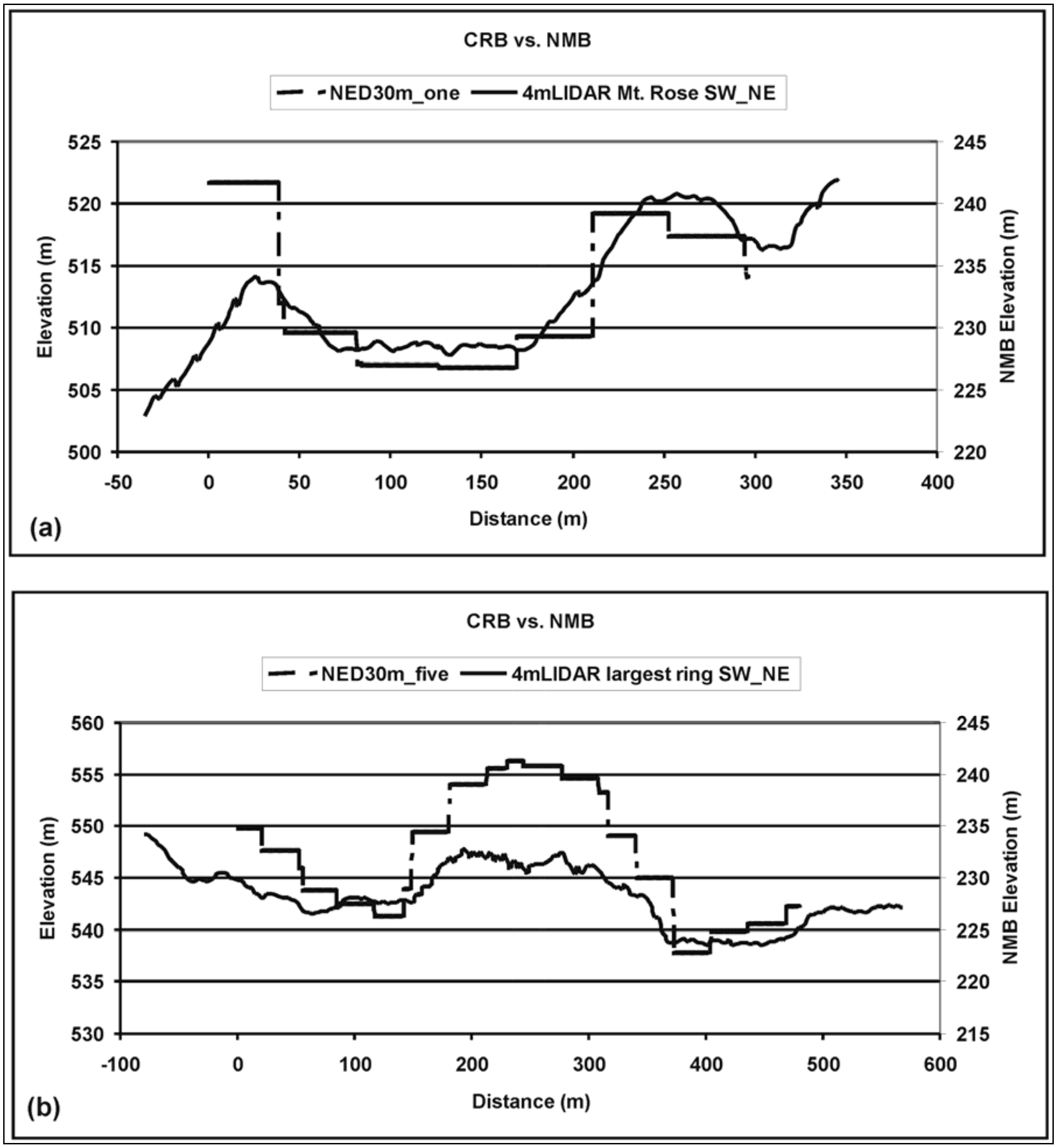

Figure 4.13 Topographic profile comparison between ring structures found in the NMB and the CRB (NED30m profiles). (A) Topographic profile comparison between the smaller eastern ring of the NMB and ring 1 of the CRB (see Figures 4.9 and 4.12 for locations). (B) Topographic profile between the larger western ring of the NMB and ring 5 of the CRB. The CRB elevations are based on a 30 m DEM from the National Elevation Database (NED) obtained from the USGS. The rings from the CRB and NMB are similar in morphology and scale.

Possible modern analogues to these ring structures are the “rootless cones” (also know as “pseudocraters”) that occur in many of the basaltic lava flows in the Myvatn District of Iceland (Thorarinsson, 1953; Fagents et al., 2002) and in Death Valley (Crowe and Fisher, 1973). The Myvatin District cones have basal diameters up to ca. 320 m. The bedding characteristics are consistent with multiple explosive pulses on stationary lava since the cones are not rafted or deformed by subsequent flow motion (Fagents et al., 2002). The rootless cones occur where lava has flowed over surface water, marshy ground, stream sediments, or outwash plains (Thorarinsson, 1953). Vaporization of the water leads to explosive excavation of the flow and the formation of the rootless cone. These cones consist of scoria, spatter and to a lesser extent lithic material from the substrate. Summit craters in the Alftaver District of Iceland, have diameters from a few meters to > 80 m with a modal diameter between 10-20 m (Greeley and Fragents, 2001).

4.6.2. EVOLUTION OF THE NMB RING STRUCTURES

A conceptual model for the formation of the NMB ring structures is presented in Figure 4.14. Prior to the deposition of the NMB, the Blomidon Formation was deposited in a lake environment with a wet climate as envisaged by Klein (1962) and others (Nadon and Middleton, 1985; Wade et al., 1996) (Figure 4.14, A, B). The LFU of the NMB was then erupted and ponded in the topographic lows, and in places above surface water (e.g.

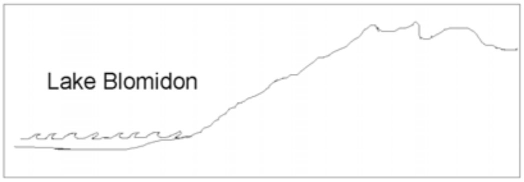

(a) Triassic deposition of fluvial and lake deposits.

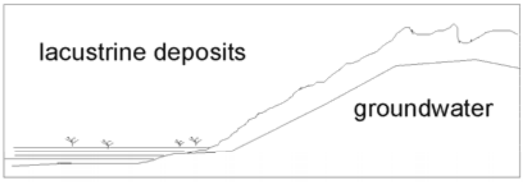

(b) Deposition of lacustrine Blomidon Formation.

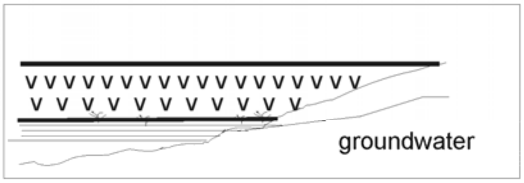

(c) Jurassic North Mountain Basalt eruption.

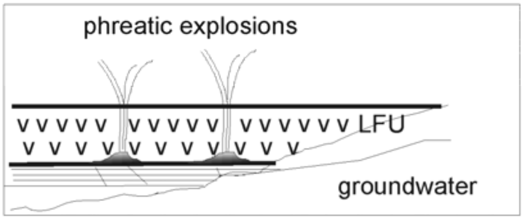

(d) Water saturated ground increases volatiles.

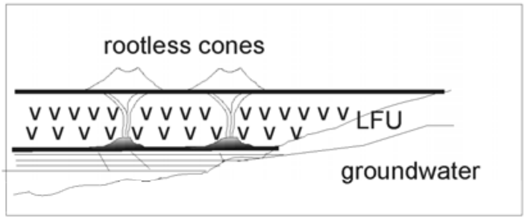

(e) Ejected material builds up the cones and fractures are intruded by residual melt.

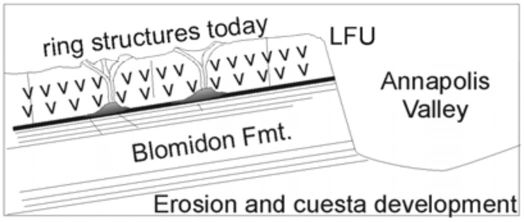

(f) Tilting and erosion removed the overlying units and cone material, leaving the rings today.

Figure 4.14 Model for the development of the NMB ring structures. (A, B) The Triassic Blomidon Formation was deposited in a lake environment with a wet climate. (C) The LFU of the NMB was then erupted and pooled in the topographic lows and in places flowed over surface water or saturated sediments of the Blomidon Formation. (D) As the lava cooled, the water beneath the partially solidified lava flow was heated, increasing volatiles, until explosive venting took place out the top of the cooled lava crust. (E) Rootless cones probably developed as a result of the accumulation of the ejected material. The molten lava within the flow was emplaced as dykes along the radial fracture pattern that resulted from collapse of the crust after the venting and withdrawal of basaltic material. (F) The rocks were then tilted during the formation of the regional syncline and subsequent erosion has removed any overlying material, exposing the resistant dike material that intruded the radial fractures around the cones.

swamps) or saturated sediments of the Blomidon Formation (Figure 4.14, C). Flow directions were generally from the southwest based on flow thickness and mafic phenocrysts (Papezik et al., 1988), however local variations in topography resulted in flow directions from the southeast (Hudgins, 1960). As the lava cooled, the water under the flow was heated and volatilized, until explosive venting took place out the top of the cooled lava crust (Figure 4.14, D). Rootless cones probably developed as a result of the accumulation of the ejected material. Basaltic dykes were then emplaced into the radial fracture pattern that resulted from collapse of the crust after the venting and withdrawal of basaltic lava (Figure 4.14, E). The presence of material representing quenched residual melt and the association with the ring structures is consistent with the observations of Hodges (1978) for the origin of the ring structures in the CRB. The MFU and UFU were subsequently deposited over the LFU, followed by tilting. Subsequent erosion removed overlying Cretaceous sediments and lava, exposing the resistant LFU dike material (Figure 4.14, F) of the ring structures visible on the LIDAR DEM.

This genetic sequence requires a paleo-environment with a shallow water table. Paleocurrent evidence suggests the dominant drainage networks flowed perpendicular to the border faults that parallel the length of the Fundy Basin (Klein, 1962; Nadon and Middleton, 1985; Wade et al., 1996). The rings together define a line oriented parallel to these faults and to the trend of the basin. Although a fault has not been mapped on the northern side of the Annapolis Valley, the trend and straightness of the cuesta suggest a NE-trending fault boundary beneath the NMB that could have provided the conduits for groundwater. The ring structures of the NMB occur at the crest of the mountain, an area that has been repeatedly scoured during the Wisconsinan glaciation (Stea, Conley, and

Brown, 1992; Stea and Kennedy, 1998; Stea et al., 1998), which may have increased the relief of the ring structures.

4.7. CONCLUSIONS

Increased detail and positional accuracy of LIDAR can clearly identify subtle geological structures that conventional aerial photography and derived elevation data cannot. The three flow units of the North Mountain Basalt have variations in chemical and physical properties that result in different resistances to erosion, which are manifest as subtle differences in topographic expression that, although subtle, are nonetheless clearly visible on the LIDAR-derived DEM. Contacts between the flow units interpreted from the LIDAR-DEM occur within corridors constrained by field mapping in the vicinity of those contacts. A sensitivity analysis using DEMs of variable resolution across three contact locations indicate that only the LIDAR-derived DEM had the precision to accurately quantify the relief of the UFU-MFU contact.

A sequence of ring structures was identified on the LIDAR-derived DEM in the LFU. The ability of LIDAR to penetrate the vegetation canopy enables a “bald earth” DEM to be constructed with spatial resolution better than 10 m. Decimetre vertical resolution has facilitated the identification of the new ring structures. As this technology becomes more available, more ring structures in basaltic flows may be identified (see McKee and Stradling, 1970). These ring structures are interpreted to be a result of the interaction between the lava and surface or shallow ground water and have similar scales and morphologies to structures observed in the Roza Member of the Columbia River Basalt

(CRB) (McKee and Stradling, 1970; Hodges, 1978). Dykes along radial fractures are exposed today at both the CRB and the NMB as a result of material being removed by erosion. The petrographic evidence of quenched residual melt associated with dike emplacement of samples near the NMB ring structures supports this interpretation. The modern analogue of such features may occur in Iceland, where they are described as "rootless cones" (Thorarinsson, 1953).

LIDAR technology provides a tool that can facilitate the identification of such subtle features in volcanic terrains that have previously been obscured on aerial photography by vegetation cover or by the limited accuracy and resolution of conventional DEMs. If this technology can accurately constrain geologic contacts between lithologically similar map units, then it may be widely applicable to terrains with more variable bedrock geology.

4.8. ACKNOWLEDGEMENT

We would like to thank Ian Spooner for discussions related to the project and his role as an advisor on TW thesis committee; Dan Kontak and Ralph Stea of the Nova Scotia Department of Natural Resources for field visits and discussions; field assistants to TW (Alex Mosher, Adam Csank, and Daniel Roberts); Patricia Stoffyn and staff for their assistance with the electron-microprobe at Dalhousie University; John Greenough and Jarda Dostal for reprints and advice. Cliff Stanley for access and assistance with the GAV-77 drill at Acadia University. The chemical analysis of the samples for this study was supported by an NSERC Discovery grant to JBM. The LIDAR data was supplied by the Applied Geomatics Research Group (AGRG) of the Nova Scotia Community College

CHAPTER 5. MEDIUM-SCALE (5 KM^2) FLUVIAL MORPHOMETRIC ANALYSIS IN A GLACIATED TERRAIN

Tim L. Webster[12] **and John C. Gosse**[1]

1. Department of Earth Sciences, Dalhousie University

Edsell Castle Circle, Halifax, NS, Canada, B3H 4R2

2. Applied Geomatics Research Group

Centre of Geographic Sciences, Nova Scotia Community College

50 Elliot Rd. Lawrencetown, NS, Canada, B0S 1M0

Ian Spooner
Geology Department, Acadia University

Wolfville, NS, Canada, B4P-2R6

J. Brendan Murphy
Department of Earth Sciences

Saint Francis Xavier University

Antigonish, Nova Scotia, B2G 2W5

5.1. ABSTRACT

Laser altimetry (4-m LIDAR) provides sufficient resolution to examine the impact of till cover and lithological resistance on incision history of similarly sized small (5 km^2) catchments in eastern Canada. The streams along the slope of the North Mountain Basalt draining into the Bay of Fundy are ubiquitously incising faster in a less resistant middle flow unit. Where till cover is thick (> 1 m on the eastern half of North Mountain) the till retards infiltration sufficiently to promote overland flow and accelerate incision relative to areas with thinner till cover. Till cover therefore is expected to impede the achievement of a steady state and may also delay stream power law relationships in larger catchments until till cover has been effectively stripped.

5.2. INTRODUCTION

Understanding the relationship between stream incision and factors related to fluvial erosion such as rock-uplift, climate, base level changes, and bedrock resistance to erosion (e.g. Stock and Montgomery, 1999; Kirby and Whipple, 2001; Stock et al., 2005) is important for the analysis of landscape evolution (e.g. Kooi and Beaumont, 1996; Dietrich et al., 2003; Pazzaglia, 2003). The availability of high resolution (4 m LIDAR) DEMs can facilitate quantitative analysis between incision and basin morphometrics at sufficiently small scales to allow the examination of isolated influences on stream evolution. Previous studies have considered the relationship between the variations in the resistance of bedrock to erosion (Sklar and Dietrich, 2001) and stream or basin morphometry to the fluvial process between regions (Belt and Paxton, 2005). However, the variations of bedrock resistance within a region (< 100 km^2) are less constrained, in part due to the scale of studies (Montgomery and Lopez-Blanco, 2003).

Fluvial processes in glaciated terrain are complex because glaciers and streams sequentially may occupy the same valleys but obey different laws of erosion, making the signatures of glacial and fluvial processes on valley size difficult to distinguish. Brocklehurst and Whipple (2002) and Montgomery (2002) used morphometric analysis including hypsometry and valley cross-sections where alpine glacial processes affected some large catchments and others were affected only by fluvial processes. They concluded that although glaciers widen and deepen valleys, significant relief enhancements are limited to large alpine glaciers. Studies applying the stream power law often use the contributing drainage area as a surrogate parameter for stream discharge which, in addition to the local channel slope, controls the stream's ability to incise the underlying bed (e.g. Snyder et al., 2000). However, few studies examine the local hydrological effects of surface and groundwater interaction on discharge (Tague and Grant, 2004). At this scale, factors such as glacial till cover and the fracture density of bedrock can influence infiltration rates and affect peak annual stream discharge.

We use high-resolution (ca. 4 m) laser altimetry (LIDAR) DEM to examine metrics of similarly-sized catchments that have been modified by glaciation. The Fundy Basin study area was selected because (i) the catchments are developed on three shallowly dipping volcanic flow units of the Jurassic North Mountain Basalt (NMB) (Figure 5.1) which each have uniform resistance to erosion throughout the study area, (ii) the Bay of Fundy provides a uniform base level for all streams, (iii) there is a clear distinction in till cover thickness over the east and west portions of the study area, and (iv) the age of deglaciation and subsequent fluvial erosion is well documented and uniform throughout. We relate stream incision depths to the variability of the flow unit's resistance to erosion and interpret the dominant processes involved for each flow unit (e.g. abrasion, plucking). We test the local effects of the variable till cover on basin morphometry and the interaction of surface and groundwater on net discharge and stream power. Our results demonstrate that till cover is a primary factor in catchment evolution. We suggest that (i) the results may be applicable to larger catchments, (ii) an initial period of disequilibrium on the order of several millennia may occur in areas with thick (> 1 m) till cover, and (iii) stream power laws may not be appropriate for small or previously glaciated catchments where till cover still exists. We also outline our approaches to dealing with anthropogenic influences when analyzing fluvial processes with high-resolution elevation data.

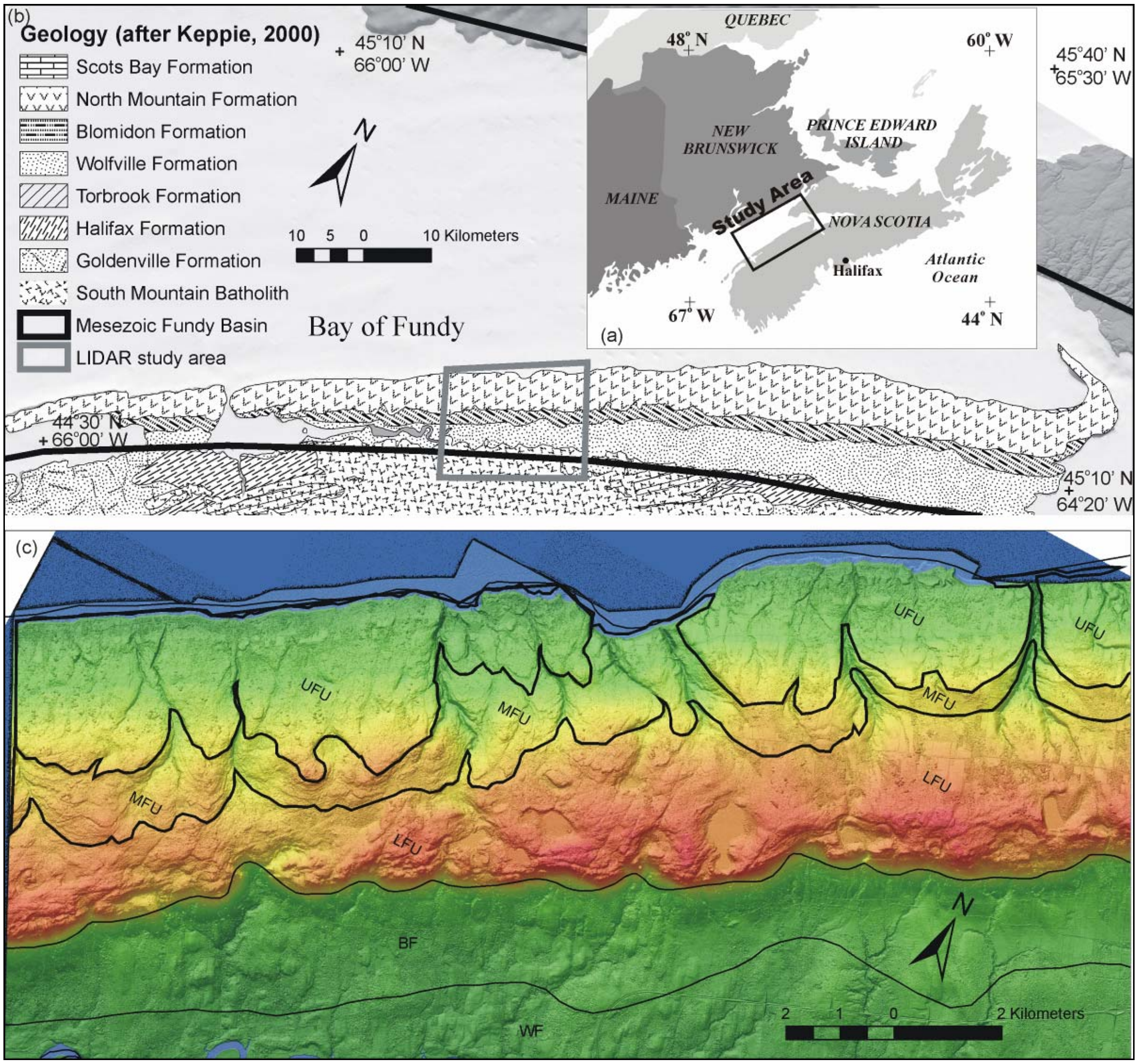

Figure 5.1 (A) Upper right study area location map (black rectangle). (B) Bedrock geology map (after Keppie, 2000) of the Fundy Basin (heavy black rectangle) with LIDAR DEM location (heavy grey line). The North Mountain Formation is not divided into flow units on this map. (C) North Mountain Basalt (NMB) flow unit boundaries overlain on LIDAR DEM (grey outline in A). NMB flow units UFU – Upper Flow Unit, MFU – Middle Flow Unit, LFU – Lower Flow Unit (from Webster et al., in press), BF – Blomidon Formation, WF – Wolfville Formation (after Keppie, 2000).

5.3. PHYSIOGRAPHY AND AGE OF THE LANDSCAPE

The study area is situated along a 20 km section of North Mountain, which comprises the eastern shore of the Bay of Fundy, known for the world's highest semi-diurnal tides. The Mesozoic Fundy Basin in eastern Canada is predominantly underlain by Triassic sedimentary rocks (Blomidon and Wolfville formations), flanked by the Jurassic North Mountain Basalt (NMB) to the north and Paleozoic rocks of the Meguma Terrane to the south (Figure 5.1). The NMB dips gently to the northwest, forms the southeast limb of a regional syncline (Withjack et al., 1995), and is crosscut by north to northeast-trending faults and fractures that exhibit dextral displacement (Olsen and Schlische, 1990; Schlische and Ackermann, 1995). Hudgins (1960) identified several volcanic flows that extend along most of the length of the NMB and Kontak (2001) described the internal stratigraphy and defined three distinct flow units. The lower flow unit (LFU) consists of a thick (40 - 150 m) massive single flow that is columnar jointed (Figure 5.1, C). The middle flow unit (MFU) conformably overlies the LFU, and consists of multiple thin flows that are highly vesicular and amygdaloidal (Figure 5.1, C). Zeolites are most common in the MFU of the NMB where they occur as amygdules and also in veins, pipes and "bubble trains" (Kontak, 1999; Pe-Piper, 2000). The upper flow unit (UFU) conformably overlies the MFU, outcrops along the shore, and consists of 1-2 massive flows (Figure 5.1, C). In a separate study, Webster et al. (in press) mapped the flow units based on their topographic signature from the LIDAR DEM and constrained the contacts by field mapping (Figure 5.1, C).

The maximum relief of the study area is 265 m (elevations ranging from sea level to the top of the North Mountain). The NMB dips approximately 6° to the northwest (i.e. toward the bay) and the land surface also slopes toward the bay at 3° to 5°. The region is characterized as having a modified continental climate, strongly influenced by the adjacent Atlantic Ocean. Meteorological records from Environment Canada indicate an annual mean precipitation of 1127 mm/yr based on records from 1971-2000, and an average daily temperature of 6.8°C. The daily average temperature drops below zero in the month of December, reaches a minimum of -5.6°C for the month of January, and rises above zero in the month of April. Of the annual precipitation, an average of 276 cm occurs as snowfall and 910 mm as rainfall, with the wettest months occurring in September and October when the average rainfall is 97 mm/month (HTTP://WWW.CLIMATE.WEATHEROFFICE.CA/CLIMATE NORMALS/RESULTS_E.HTML). The land cover on the North Mountain is influenced by the occurrence of the till cover; farmland (pastures and hayfields) and mixed forest dominate in the east where the till is thickest, whereas the west has mostly mixed forest cover. There are more roads and anthropogenic influences in the east compared to the west where only one paved road occurs along the coast. The coastline varies between gently sloping bedrock platforms and ca. 25 m cliffs that occur in embayments.

The region was affected by fluctuations in Late Wisconsinan ice dynamics until ca. 12 ka (^{14}C yr) (Stea and Mott, 1998). The earliest ice flows were eastward and southeastward from an Appalachian or Laurentide ice source ca. 75-40 ka (Caledonia ice flow phases 1A and 1B, Stea et al., 1998). The Hartlen Till was deposited as a result of the southeastward ice flow and typically consists of 40% gravel, 40% sand and 20% mud (silt and clay) (Lewis et al., 1998). The second major ice-flow was southward and southwestward from the Escuminac Ice Centre in the Prince Edward Island (PEI) region (Escuminac ice flow phase 2, ca. 22-18 ka, Stea et al., 1998). The subsequent Lawrencetown Till (Stea et al., 1998) is a reddish muddy till unit that has higher clay content than the Hartlen Till due to the incorporation of Carboniferous red bed sediment derived from Prince Edward Island, and typically consists of 20-30% gravel, 30-40% sand, and 30-50% mud (silt and clay) (Lewis et al., 1998). Ice then flowed northwestward and southward from the Scotian Ice divide across the axis of Nova Scotia (Scotian ice flow phase 3, ca. 18-15 ka, Stea et al., 1998). In many localities, the Lawrencetown Till is overlain by a thin (1-4 m) hybrid till related to this event, known as the Beaver River Till, which generally consists of 50% gravel, 40% sand, and 10% mud (silt and clay) (Lewis et al., 1998). Locally ice flowed from the Scotian Divide northwestward over the NMB into the Bay of Fundy. With the late-glacial rise of relative sea level, ice margins calved, and ice flux into the Bay of Fundy increased to merge with southwestward ice streams from New Brunswick (Chignecto ice flow phase 4, ca. 13-12.5 ka, Stea et al., 1998). The study area was ice free by ca. 12 ka and postglacial emergence in the Bay of Fundy is complete (Grant, 1980).

Although the majority of emphasis has been placed on the coastal flank, study of the terrain landward of the North Mountain was necessary to document the variability in till cover. The streams on the Fundy side of NMB have evenly-spaced mainstems (1.5 km), similar catchment areas (ranging from 2 to 8 km^2) and are all consequent dendritic drainages with stream densities ranging from 0.9 to 2.9 km/km^2 (Table 5.1, Figure 5.2). The streambeds are typically 80% bedrock and 20% boulder-covered. Till is present in the streambed of some of the basins, attesting to the youthfulness of these catchments and to the inheritance of some low relief pre-glacial topography. Within the NMB study area, there are similar size basins (2 – 8 km^2) that drain scoured bedrock, and occur in the transition zone with scoured bedrock in their headwaters and glacial till near their outlets, and drain a glacial till blanket covering the basalt. The streams are ephemeral with their peak flows occurring in the spring and fall seasons. Their long profiles are ungraded and have several knick zones.

5.4. METHODS

Although the effect of DEM resolution on measuring different hydrologic and geomorphic properties has been examined (e.g. Wolock and Price, 1994; Zhang and Montgomery, 1994; Goa, 1997; Zang et al., 1999; Walker and Willgoose, 1999), most of these studies have focused on the different effects of grid cell size interpolated from similar source data rather than advances in data acquisition technologies such as laser altimetry. In this study, the high-resolution of the LIDAR (Light Detection and Ranging) DEM allows detailed analysis of basin and stream morphometrics to assess the local effects of variations in bedrock resistance and glacial till cover within a region. LIDAR is a remote sensing technique used to derive precise elevation measurements of the earth's surface (Ritchie, 1995; Flood and Gutelius, 1997; Wehr and Lohr, 1999). It has been used in a limited number of geoscience applications, including the analysis of river networks (Kraus and Pfeifer, 1998; Gomes Pereira and Wicherson, 1999; Stock et al., 2005), the generation of cross-sections across rivers (Charlton et al., 2003), investigation of landslides (McKean and Roering, 2003), and in mapping tectonic fault scarps (Harding, et al., 2000; Haugerud et al., 2003).

5.4.1. LIDAR AND DEM ANALYSIS

Details of the LIDAR data specifications and height validation results for this study are described in Webster (in press). LIDAR data were acquired for the study area with an average ground point spacing of 2-3 m in open areas and 5-8 m in forested areas. Customized automated Arc/Info ™ GIS routines for the validation of the LIDAR point data are available in Webster and Dias (in press). The height validation results indicate that the original LIDAR ground points and the derived DEM are, on average, typically within 15 cm of measured GPS heights and 95% of the data are within 30 cm for open hard surfaces (i.e. roads, parking lots). The LIDAR ground points were used to construct a "bald earth" DEM at a 4 m resolution utilizing the ESRI suite of ArcGIS ™ v. 8 and 9 software. A combination of Rivertools ™ v. 3 and PCI Geomatica ™ v. 9 software was used to extract the morphometric parameters from the drainage basins and stream longitudinal profiles.

A colour-shaded relief (CSR) map was constructed from the DEM based on a shading azimuth angle of 315^{o} (which is perpendicular to the strike of the flow units) (Figure 5.2), and used to extract the contact between the three flow units of the NMB based on their topographic expression and constrained by detailed field mapping (for details see Webster et al., in press) (Figure 5.1, B). Although the CSR DEM was useful for highlighting the contacts between flow units, it was limited in highlighting some of the

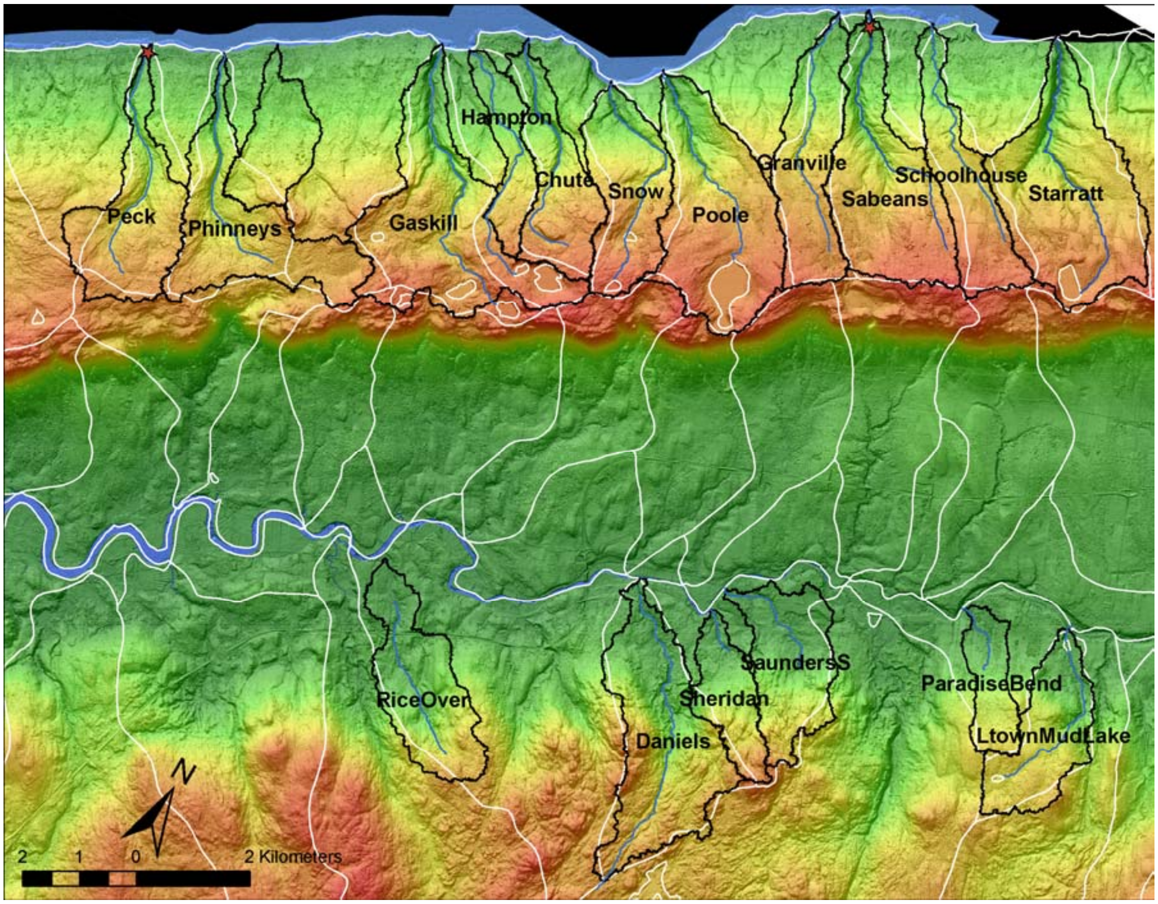

Figure 5.2 Labeled catchment basins (black lines) calculated from the LIDAR DEM for the North and South Mountains. The white lines represent the existing watershed boundaries derived from manual interpretation of 1:50,000 topographic maps (watershed data courtesy of Nova Scotia Department of Environment). The two red stars denote the location of stream discharge and water quality sensors in Peck and Sabeans basins.

subtle lower relief landforms associated with late glacial ice dynamics. A new map was constructed from the DEM with a shading azimuth angle of 225^{o}, to highlight northwest trending landforms, and the elevation colour ramp was repeated to optimize chromostereoscopy (3-D visualization see Toutin and Rivard, 1995). The colour ramp is applied to the elevation range 0-100 m, and repeated for elevations of 101-265 m in order to highlight the low relief landforms (Figure 5.3).

5.4.2. DEM CONDITIONING

Catchment basins are calculated for the main streams draining into the Bay of Fundy and streams draining the South Mountain into the Annapolis River from the LIDAR DEM based on outlet locations identified on 1:10,000 scale topographic maps using Rivertools^{TM}. The location of the outlets and resultant basin metrics are presented in Table 5.1. The standard D-8 algorithm (Jenson and Dominque, 1988; Costa-Cabral and Burges, 1994) is used to determine down-stream flow direction and sinks (depressions within the DEM treated as errors by the algorithm) are filled in the DEM to allow continuous down stream flow. At most resolutions, care must be taken to consider that some landscape metrics are fractal, such as relief and slope (Anhert, 1970; van der Beek and Braun, 1998; Zhang et al., 1999). For this study the emphasis is on stream incision depths on catchments with similar size so we have not chosen a fixed-scale averaging method—this allows us to examine the streams with maximum DEM resolution. However, when dealing with DEMS at high resolution, other considerations must be made. Inspection of the drainage basin boundaries and stream longitudinal profiles indicates that most catchments have sinks. Many of these sinks are adjacent to the raised elevations of a roadbed captured by the high resolution of the LIDAR DEM. As a culvert could not be represented on the DEM, a “notch” was cut across the roadbed and assigned an elevation of the nearest downstream cell to improve the accuracy of the flow direction algorithm and to prevent excessive erroneous sink filling operations in deriving the catchment basins and stream profiles. This modification improved accuracy of the flow direction algorithm, prevented excessive erroneous sink-filling operations in deriving the catchment basins and stream profiles, and allowed the stream to "pass through the roadbed". The overall result is the generation of a more accurate and flow accumulation grid and basin boundary.

Table 5.1 North Mountain basin metrics derived from LIDAR DEM in Rivertools^{TM}. Drainage density* calculated from the stream network on the 1:10,000 topographic map.

Catchment Type SB – scoured bedrock TR – transition TB – till blanket	**X_Out**	**Y_Out**	**Z_Out**	**Area (km^2)**	**Relief (km)**	**Stream Order**	**Drainage Density from DEM streams km/ km^2**	**Drainage Density* from mapped streams km/km^2**	**Source Density from DEM streams streams/ km^2**
Peck (SB)	309527	4972557	0.22	4.52	0.067	9	293.71	1.65	20853.22
Phinneys (SB)	310731	4973065	0.73	5.31	0.095	9	291.87	0.94	21906.91
Gaskill (TR)	313983	4975137	0.29	7.81	0.085	9	292.30	1.38	19107.54
Hampton (TR)	314463	4975253	0.30	2.03	0.049	8	295.86	2.9	21531.11
Chute (TR)	315259	4975973	0.53	3.59	0.084	8	295.85	1.25	20472.35
Snow (TR)	316899	4976037	0.39	4.11	0.095	9	294.91	1.12	19626.51
Poole (TR)	317603	4976673	0.37	7.01	0.091	9	292.08	0.91	20016.68
Granville (TB)	319783	4979105	0.50	4.23	0.053	9	293.01	1.39	22753.39
Sabeans (TB)	320227	4979393	0.22	6.20	0.068	9	295.46	2.2	21405.68
Schoolhouse (TB)	321315	4979753	0.28	3.63	0.056	9	291.89	1.42	23913.17
Starratt (TB)	323323	4980721	0.17	7.66	0.077	9	293.07	1.34	20354.42

5.4.3. CATCHMENT BASINS AND LONGITUDINAL PROFILES

Catchment basins extracted from the DEM include eleven draining the NMB into the Bay of Fundy (Figure 5.2). Table 5.1 presents the results of the extracted basins from Rivertools™ including drainage area, relief, drainage density and source density. The drainage density did not significantly change between the basins, regardless of what stream order was used when calculated in Rivertools™. Therefore drainage densities were calculated based on the 1:10,000 topographic map stream network and showed more variability (Table 5.1). The longest streams from the topographic map are extracted for each basin to facilitate comparison with the trunk streams extracted from the DEM stream network that had the highest stream order (typically 8 or 9, Strahler, 1952). Longitudinal profiles of the two sources of trunk streams are plotted for each basin. In general the trunk streams derived from the DEM are longer than those from the topographic map (i.e. more vertices defining a line) but do not extend as far upstream in the basins. In part this is a result of the fractal nature of stream lengths (Turcotte, 1992), but the greater length of the high resolution DEM-derived stream lines are also a consequence of the grid cell origin of the network compared to the straighter line segments on the topographic map (Webster et al., in review). It was determined that the streams from the topographic map and the longitudinal profiles obtained from the original DEM prior to sinks being filled are the most representative based on field observation and are used for the rest of the analysis. The surface profiles of the drainage divide bordering each basin are averaged and the stream longitudinal profile is subtracted to compute the incision depth along the stream's entire length. The basalt flow units were intersected with the stream longitudinal profiles and the incision depth was summarized for each flow unit. The results are presented in Table 5.2.

5.4.4. BEDROCK RESISTANCE TO EROSION

The variability of the lithological resistance to erosion by abrasion was tested in laboratory experiments on flow unit samples using a shatterbox that consists of a cylindrical container that holds a central disk and an outer ring. Samples were crushed and sieved so material was between 2 and 5 mm in diameter and placed in the shatterbox which was agitated for times ranging from 2-15 minutes for the MFU to 20 to 40 minutes for the UFU and LFU. The samples were weighed prior to loading them into the shatterbox, then were sieved and weighed again after a set time of agitation to measure the change. The results are presented in Table 5.3.

Potential erosion by plucking was quantified by measuring the degree of fracturing in the basalt. Although lineaments can be observed on the shaded relief LIDAR maps and aerial photos, these represent larger scale fractures that do not appear to be controlling erosion in the streambed. Drill core containing the MFU and LFU of the NMB was used to quantify the fracture density at a smaller scale and the distribution of vesicles and zeolite-bearing amygdules. Approximately 210 m of basalt was recovered from drill hole GAV-77-3 located 20 km east of the study area (Comeau, 1978). Distinction between individual flows was based on the degree of oxidization of the flow and the amount of vesicles and amydgules of different sizes and characteristics (i.e. large or small, stratified or bubble pipes). Magnetic susceptibility and rock quality designation (RQD), an engineering property that computes the percentage of cumulative length of segments longer than 10 cm within 1 m of core, and the number of fractures were measured for every metre of core.

5.4.5. VALLEY CROSS-SECTIONS AND HYPSOMETRY

Valley cross-sections between drainage divides are extracted for each of the basins in order to evaluate the incision depth using a method similar to that described in Montgomery (2002). Valley bottoms are aligned for cross-sections midway upstream of each basin in order to facilitate comparison in valley shape between the two basin end-members (the scoured bedrock and till blanket basins). The valley cross-sections are used to compute the volume of material removed as described in Mather et al. (2002) for each basin.

Although Willgoose and Hancock (1998) cautioned that hypsometric curves are non-unique and that the basin geometry strongly influences the shape of the curve, hypsometric curves and integrals have been used to examine the relationship between glaciated and unglaciated drainage basins (Brocklehurst and Whipple, 2004) and fluvial systems that have been overprinted by glacial processes (Baroni et al., 2005). In this study, hypsometric curves are generated in Rivertools^{TM} to quantify the morphometric differences in basins from the scoured bedrock and till blanket end-members. The hypsometric integral (HI), which represents the area under the hypsometric curve, is also estimated for these basins as described in Brocklehurst and Whipple (2004).

The elevations associated with the drainage divides were used to construct a paleosurface of the NMB following a similar method to that described by Brocklehurst and Whipple (2002) and Montgomery and Lopez-Blanco (2003). The LIDAR DEM was then subtracted from this surface in order to quantify the volume of material removed by glacial-fluvial processes and the patterns of erosion for each basin.

Erosion rates are calculated from the stream incision depth curves and sediment flux from the erosion depth map assuming erosion began after deglaciation at 12 ka ± 200 yr (1σ) (Stea and Mott, 1998). The uncertainties associated with the incision and erosion flux measurements are difficult to quantify, however they are controlled in part by the accuracy and resolution of the DEM. The accuracy of the LIDAR DEM has been reported by Webster (in press) and of the LIDAR points by Webster and Dias (in press). However, much of their results are based on comparisons of the LIDAR with GPS measurements in open areas. Since much of the catchments analyzed in this study area occur within forested areas, the LIDAR DEM Δz (Δz = DEM – elevation checkpoints) was compared to forest transects consisting of over 250 measurements. In addition, a stream longitudinal profile was surveyed and compared to the LIDAR DEM values in order to access the accuracy of the stream incision measurements (Webster et al., in review).

5.4.6. SURFACE AND GROUNDWATER INTERACTION

The effect of glacial till cover on surface and groundwater interaction and stream discharge is evaluated by computing hydrographs and measuring water chemistry parameters in two of the catchments with contrasting amounts of till cover. The scoured bedrock thin till cover is represented by the Peck catchment and the thick till blanket is represented by the Sabeans catchment. These catchment basins were selected because they represent basin type end-members (scoured bedrock and thick till cover) of comparable size (Table 5.1) and therefore can be used to test if drainage area is an appropriate surrogate measure for discharge in glaciated terrains. The streams were instrumented to record hourly stream discharge and water chemistry parameters from April to July 2004. Level logger pressure transducers were placed in or near culverts to record stream stage near the outlets of Peck and Sabeans catchments (locations shown in Figure 5.2). Manning's equation was used to calculate flow velocity and convert stream stage to discharge for the two channels (e.g. Rose, 2004). Hydrolab datasondes were also deployed near the outlet of these two basins and recorded water chemistry parameters, temperature, pH, specific conductance, dissolved oxygen, and turbidity. Campbell Scientific meteorological stations deployed throughout the Annapolis Valley and on the North Mountain were used to measure meteorological events which were related to the stream data. The stream discharge, water chemistry and meteorological data were integrated and stream hydrographs constructed for the two basins. The hydrographs were normalized by basin drainage area as reported in Tague and Grant (2004).

5.5. RESULTS

5.5.1. LIDAR AND DEM ANALYSIS

The enhanced spatial resolution of LIDAR and the ability to penetrate the vegetation canopy allow subtle topographic features to be highlighted. The CSR DEM is compared to the surficial geology boundaries and glacial striations (see Stea and Kennedy, 1998) (Figure 5.3, A). The contrast in terrain roughness from west to east on the North Mountain is visible on the DEM. The rough terrain in the western region of the North Mountain correlates with glacially scoured bedrock, and the smoother terrain in the eastern region correlates with the Lawrencetown Till blanket (Stea and Kennedy, 1998) (Figure 5.3, A, B). Two previously unidentified glacial landforms have been mapped in the valley floor based on the CSR DEM (Figure 5.3, C); (i) a set of oval landforms with their long axis trending ca. 335^o is identified in the western region (field observations indicate these subtle topographic highs are composed of Lawrencetown Till material and are draped by glacial marine lacustrine clay); (ii) a set of streamlined landforms composed of Lawrencetown Till material with their long axis trending ca. 310^o is identified in the eastern region. The till blanket on the eastern flank of the North Mountain appears to have some control on the upper reaches of the streams, which flow in a 335^o direction parallel to the streamlined landforms in the valley. These reaches trend in a more northerly flow direction midway to their outlets, similar to the streams in the scoured bedrock catchments to the west (Figures 5.2, 5.3). The streamlined landforms and the alignment of the upper reaches of streams in the till blanket catchments are likely

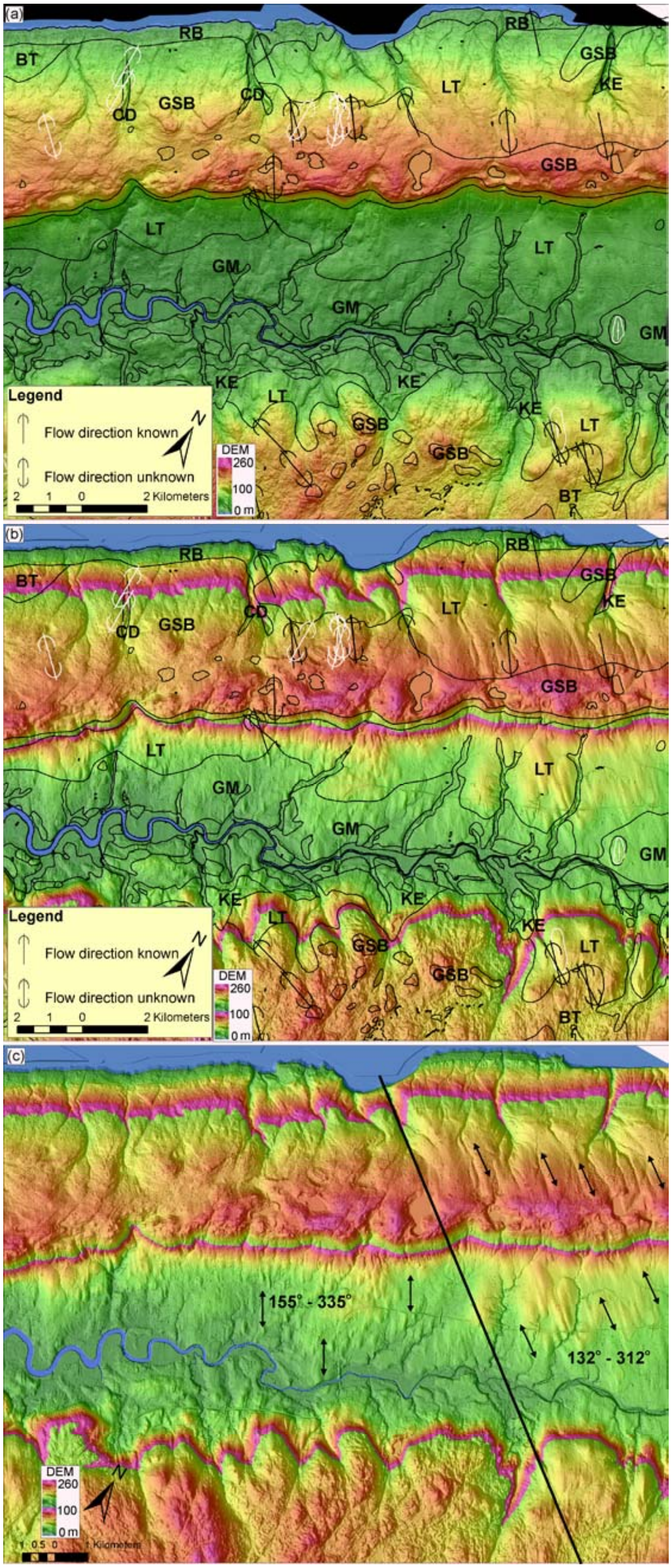
(a)
RB
BT
GSB
CD
LT
KE
GM
Legend
Flow direction known
Flow direction unknown
2 1 0 2 Kilometers
N
DEM
260
100
0 m
(b)
(c)
155° - 335°
132° - 312°
1 0.5 0 1 Kilometers

Figure 5.3 Colour shaded relief DEM maps (A and B) compared with surficial geology boundaries and glacial striations (black symbols from Stea and Kennedy, 1998), white symbol striations from this study). Surficial geology map codes: RB - raised beach deposits, GSB - glacially scoured bedrock, LT - Lawrencetown Till, GM - glaciomarine lacustrine deposits, BT - Beaver River Till. (A) Standard chromostereoscopic colour coding of the DEM to enhance overall terrain features and relief, shading azimuth angle from 315° and zenith angle 45° with a five times vertical exaggeration. (B) Same colour ramp as above except it is scaled from 0-100 m, then repeated in order to enhance the subtle topographic features at lower elevations, shading azimuth angle changed to 225° to enhance northwest-trending glacial landforms. (C) Same image as (B) with the landform trends highlighted by double headed arrows. The field of oval shaped landforms trend 155-335°, and the streamlined landforms in the east trend 130-310°. The terrain on both mountains east of the heavy line is smoother than the terrain to the west of the line.

to be a result of the Scotian ice phase, which appears to have been the last ice advance to affect this area (Stea and Mott, 1998). The streamlined landforms and distribution of till suggests that an ice stream may have flowed from the South Mountain across the valley into the Bay of Fundy (e.g. Stokes and Clarke, 2001).

5.5.2. MORPHOMETRIC ANALYSIS – CATCHMENT BASINS AND LONGITUDINAL STREAM PROFILES

The location of the catchment outlets and basin metrics of the NMB are listed in Table 5.1. The catchment boundaries are compared with existing boundaries derived from the manual interpretation of 1:50,000 topographic maps (Figure 5.2). The longitudinal profiles of the NMB trunk streams do not display the characteristic concave-up shape of streams in equilibrium; rather the profiles show variations in concavity

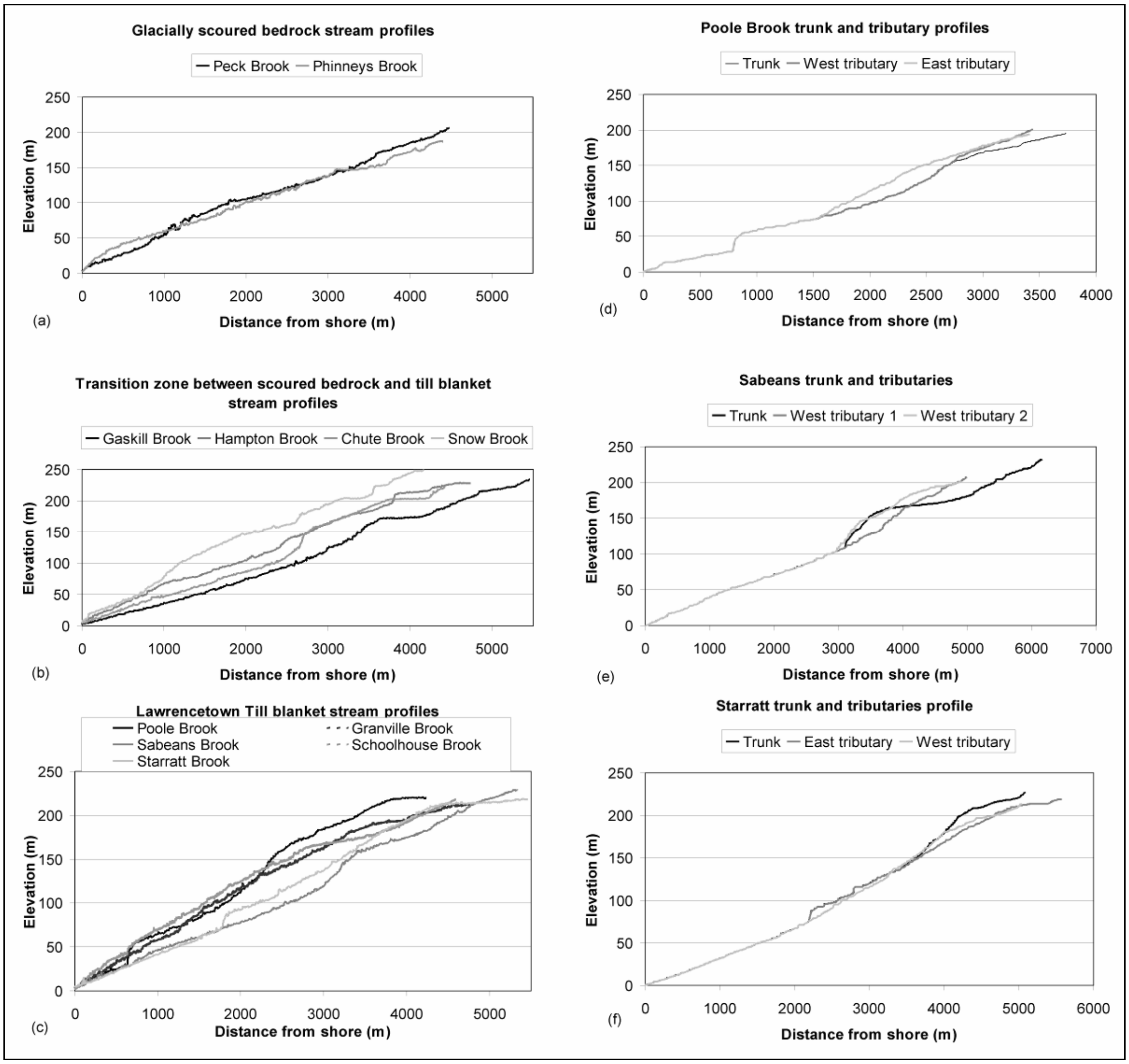

Figure 5.4 Stream longitudinal profiles derived from the LIDAR DEM. (A) Long profiles of streams within the scoured bedrock area. (B) Long profiles for streams within a transition zone that has glacial till deposits in the lower half of their basins and scoured bedrock in their headwaters. (C) Long profiles of streams within the Lawrencetown Till blanket. (D) Long profiles showing the knick zone in the trunk stream and tributaries of Poole Basin. (E) Long profiles showing the knick zone in the trunk stream and tributaries of Sabeans Basin. (F) Long profiles showing the knick zone in the trunk stream and tributaries of Starratt Basin.

ranging from straight sections, to mildly convex (Figure 5.4). Some streams do exhibit concave reaches near knick zones (Figure 5.4, B, C). The longitudinal profiles have been classified into three categories according to the degree of glacial till blanket cover within their catchments.

The profiles of the scoured bedrock catchments have nearly straight slopes with minor curvature (Figure 5.4, A). Profiles for catchments that are in the transition zone with scoured bedrock in their headwaters and the Lawrencetown Till cover near their outlets show a range of concavity characteristics with knick zones uniformly located approximately 1000, 2700 and 3800 m from their outlets to the bay (Figure 5.4, B). Profiles of catchments totally covered by the Lawrencetown Till blanket are generally straight to concave, and have knick zones that occur at 750 m, 1700 m from their outlets and a more subtle zone at 3200 m (Figure 5.4, C). The profiles are slightly concave upward directly upstream of these knick zones, and then display a transition to a convex upward profile as they near the headwaters. The knick zones do not appear to be related to the confluence of tributaries with the trunk streams derived from the DEM stream network (Figure 5.4, D-F), although the waterfall at Starratt Brook 2200 m from the outlet resembles a hanging valley in the field and in profile (MacGregor et al., 2000).

The reach of Starratt Brook that forms the knick zone (2200 m from the outlet) enters the trunk stream from an orientation of 320°, again parallel with the streamlined landforms associated with the last movement of ice across the study area. The other knick zones that occur along trunk streams may represent a wave of incision associated with changes in base level (Seidl et al., 1994; Seidl et al., 1997; Weissel and Seidl, 1998; Pazzaglia et al., 1998) in combination with the variable resistant to erosion of the flow units.

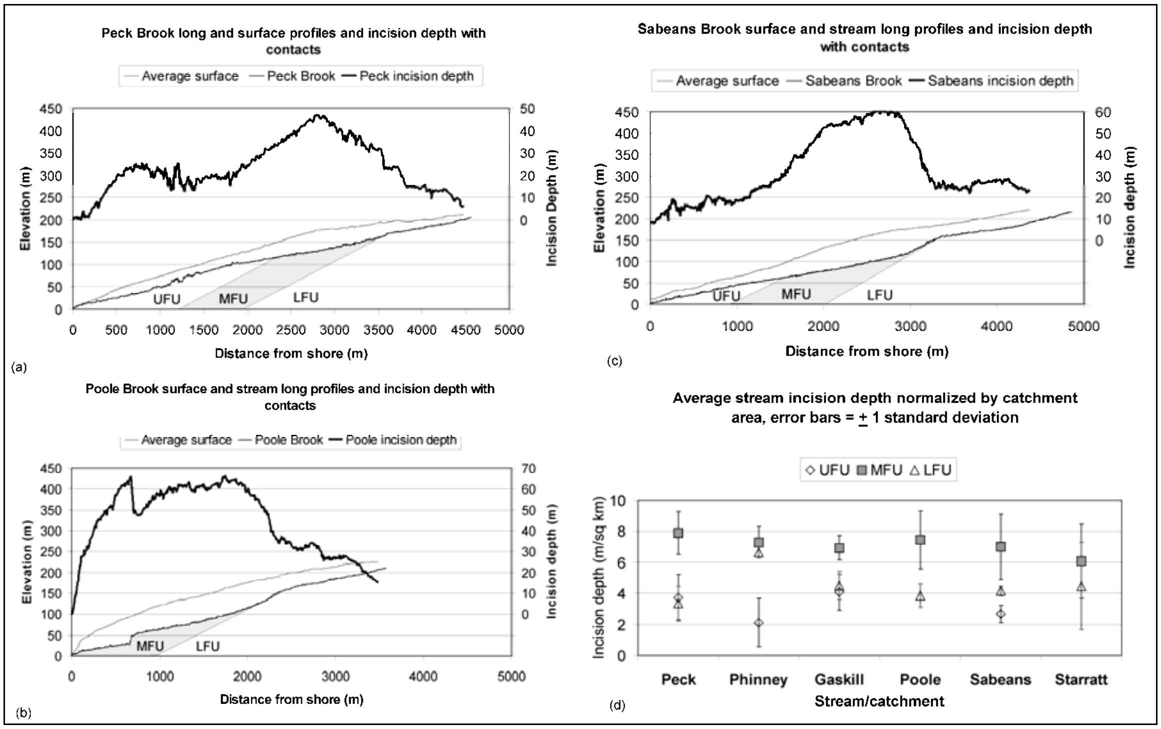

Figure 5.5 Stream incision depth diagrams for the main drainage basins along the North Mountain. The surface profiles associated with the drainage divides and the stream long profile are plotted along with the depth of incision (difference between surface and stream profiles). The NMB flow unit (UFU, MFU, LFU) contacts have also been projected to intersection the streambed and related to the depth of incision. (A) Peck Brook profiles and incision. (B) Poole Brook profiles and incision. (C) Sabeans Brook profiles and incision. (D) Average incision depth for each flow unit of the NMB normalized by the drainage area for each basin and error bars indicates ± 1σ.

The stream profiles and incision depths were overlain on the flow unit map of the NMB (Figure 5.1) in order to relate the incision depth to the basalt flow units. The flow units dip approximately 6^{o} to the northwest and have been projected on to the stream profiles (Figure 5.5). In general the stream incision depth reaches a maximum within the middle flow unit (MFU) (Figure 5.5, A-D). Many knick zones occur either within the MFU or upstream of the contact between the MFU and lower flow unit (LFU). Incision in the upper flow unit (UFU) and LFU is similar in 3 of the 4 basins studied where both units outcrop in the streambed (Figure 5.5, D). The average incision depth for the MFU is 45 m compared to 29 and 19 m for the LFU and UFU, respectively (Table 5.2). The area percentage of each flow unit per basin and the length percentage of each flow unit per stream suggest that the percentage of flow unit per basin is a better indicator of stream incision depth than the percentage of stream length within a flow unit. The average incision depth is lowest in the catchments where the till cover is thinnest (Table 5.2) However, the highest incision depths are associated with the catchments in the transition zone between the thin and thick till blanket areas (Table 5.2).

Table 5.2 Basalt flow unit percentage per catchment, average stream incision depths for each flow unit per catchment, overall average incision depth per catchment, and incision rate per catchment assuming a start time at 12 ka.

Catchment	**% Drainage area LFU**	**Incision depth (m) LFU**	**% Drainage area MFU**	**Incision depth (m) MFU**	**% Drainage area UFU**	**Incision depth (m) UFU**	**Average incision depth (m)**	**Maximum incision rate (km/Ma)**
Peck	38.4	15.2	39.3	35.7	22.4	16.8	23.4	2.0
Phinney	62.5	35.4	17.4	38.8	20.1	11.3	28.5	2.4
Gaskill	54.0	35.2	27.4	54.2	18.6	31.8	42.3	3.5
Poole	68.4	27.1	30.5	52.2	1.2		44.6	3.7
Sabeans	45.5	25.8	21.1	43.5	33.1	16.6	32.4	2.7
Starratt	53.8	34.2	42.8	46.5	3.4		37.9	3.2
Average incision depth (m) per flow unit		28.8		45.2		19.1		

The results of comparing the Δ z between the LIDAR DEM and the ground elevation measurements under the forest canopy indicate a mean difference of -0.38 m and a standard deviation of 0.37 m, thus the elevations of the drainage divides are considered accurate to within ± 0.73 m (2σ). However, the accuracy could be worse depending on the local relief within the 4 m by 4 m area of a cell. The summary statistics of the stream longitudinal survey indicate a mean Δ *z* of -0.94 m, with a standard deviation of 1.26 m, and a RMS error of 1.57 m (Webster et al., in review; Chapter 6). The survey data matches the DEM within 0.5 m in many places; however it is too high by a few metres in other places where there is dense overhanging vegetation. These results indicate that the stream profiles in forested areas are considered accurate to within ± 2.52 m (2σ). Because the incision depths are calculated from the drainage divides and the stream profile, they are considered to be accurate to within ± 3.25 m (2σ).

5.5.3. BEDROCK RESISTANCE TO EROSION

As indicated by experimental results (Table 5.3), the MFU is much more susceptible to erosion by abrasion than the UFU and LFU. The resistance of the MFU is variable depending on the density of vesicles and amygdules. For example, after 10 min. of abrasion, MFU sample BT17 had over 50% of the sample greater than 2 mm in diameter, whereas MFU sample PC49 only had 32% greater than 2 mm in diameter after 2 min. of abrasion (Table 5.3). With the exception of UFU sample PG1, the UFU and LFU broke down at similar rates and are significantly more resistant to abrasion than the MFU. PG1 was taken from an outcrop along the Bay of Fundy and may be more susceptible to abrasion because of the influence of prolonged exposure to salt water, and so is not considered to be representative of the UFU eroded in the streambed. Drill core analysis shows that the highly vesicular and amygdaloidal MFU has a higher rock quality designation (RQD) than the LFU, indicating a higher percentage of rock segments longer than 10 cm (Figure 5.6). The LFU has a greater number of fractures per metre than the MFU and a lower RQD indicating fewer segments greater than 10 cm in length per metre. The UFU does not occur in the drill core, however field observations indicate that secondary minerals have sealed fractures in this unit and that erosion by plucking is less prevalent in this unit than in the MFU or LFU.

The variation in stream incision depths appears to be related to several characteristics of the bedrock lithologies including the resistance to abrasion, and the degree and spacing of fractures. Based on observations of plucking in the streambed, the high fracture density of the LFU controls erosion in the streambed for this unit. Erosion of the MFU is controlled by fractures and its susceptibility to abrasion that is variable based on the concentration of vesicles and zeolite-filled amydgules as observed in the drill core.

Table 5.3 Shatterbox experiment for the NMB flow units results. Upper flow unit UFU, middle flow unit MFU, lower flow unit LFU, and weight percent of original sample for each sieve size.

Time (min)	>2 mm	>1mm	>0.5mm	>0.25mm	>0.125mm	>0.0623mm	<0.0623mm	Sample	Rock_type
1	32.64	22.33	10.94	8.77	8.38	7.37	9.56	PG1	UFU
2	0.00	4.80	9.25	16.76	21.14	29.60	18.46	PG1	UFU
5	0.00	3.56	3.45	13.72	22.54	41.03	15.69	PG1	UFU
5	58.06	12.10	5.78	4.49	4.80	6.40	8.37	PC48	UFU
10	66.87	8.65	5.17	4.39	4.32	4.43	6.17	AR5	UFU
20	0.00	0.00	0.00	8.58	25.32	30.30	35.80	AR5	UFU
2	63.65	10.20	5.50	4.90	4.84	4.87	6.04	BT17	MFU
5	53.60	14.45	6.68	5.43	5.34	5.74	8.76	BT17	MFU
10	53.20	14.91	6.58	5.22	7.63	3.76	8.70	BT17	MFU
15	0.00	0.00	0.00	9.43	62.68	6.67	21.22	BT17	MFU
2	31.80	21.25	10.76	7.77	7.39	7.08	13.95	PC49	MFU
3	6.56	6.62	9.90	14.35	14.91	17.29	30.38	PC49	MFU
5	54.69	14.67	6.59	4.90	4.60	4.83	9.71	PC52	LFU
10	3.55	6.17	10.44	15.35	12.95	23.07	28.47	PC52	LFU
15	73.19	7.75	4.24	3.61	4.44	2.86	3.92	AR3	LFU
25	71.57	8.57	4.44	3.84	3.68	3.74	4.15	AR3	LFU
40	55.42	12.24	7.43	6.48	6.28	6.71	5.44	AR3	LFU

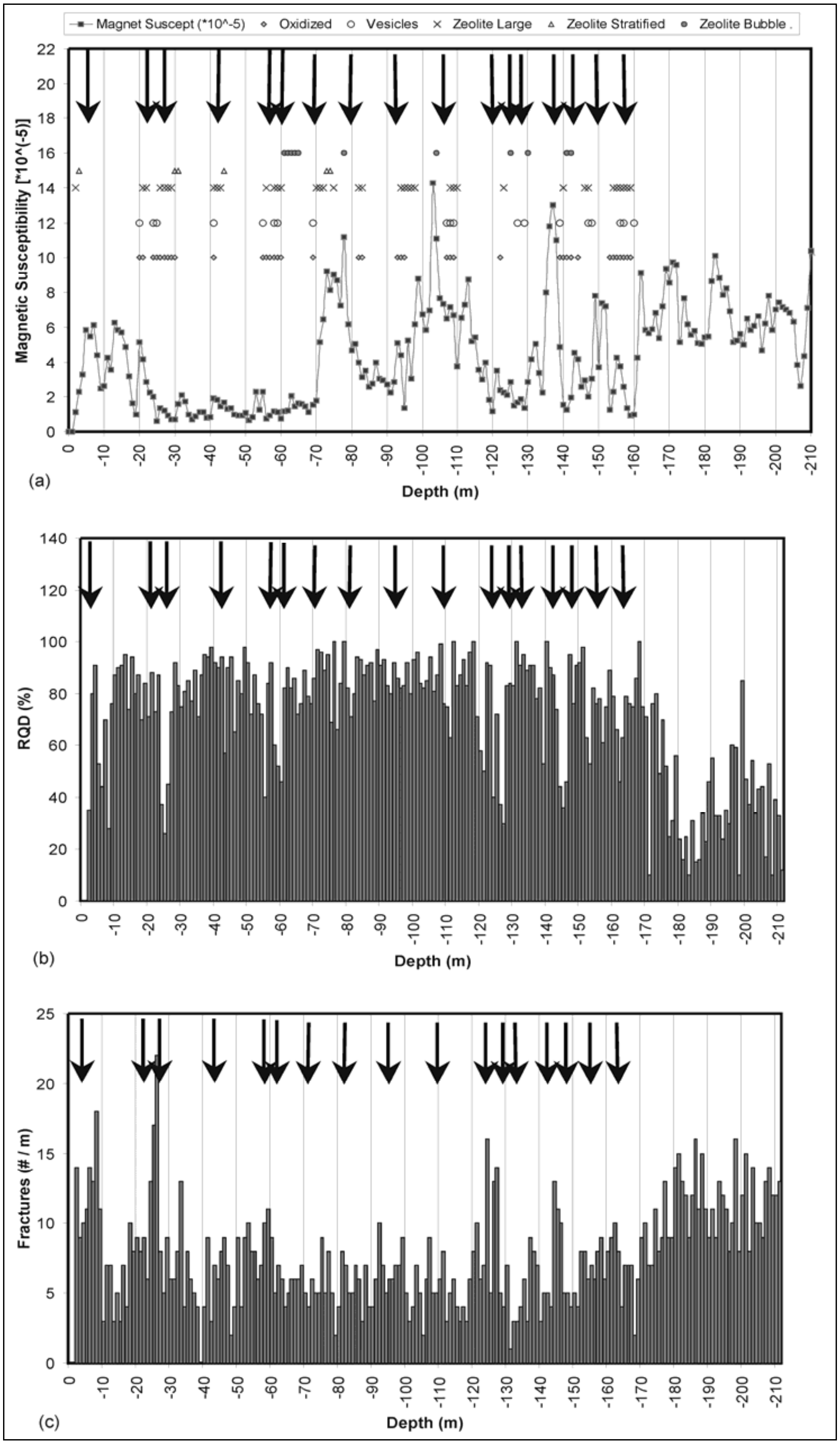
Magnet Suscept (*10^-5)
Oxidized
Vesicles
Zeolite Large
Zeolite Stratified
Zeolite Bubble .
Magnetic Susceptibility [*10^(-5)]
0
2
4
6
8
10
12
14
16
18
20
22
0
-10
-20
-30
-40
-50
-60
-70
-80
-90
-100
-110
-120
-130
-140
-150
-160
-170
-180
-190
-200
-210
(a)
Depth (m)
RQD (%)
0
20
40
60
80
100
120
140
(b)
Depth (m)
Fractures (# / m)
0
5
10
15
20
25
(c)
Depth (m)

Figure 5.6 Plots of drill core logs of hole GAV77-3 for the NMB. (A) Magnetic susceptibility and the distribution of oxidized basalt interpreted to represent flow tops and the distribution of vesicles and amygdules. The arrows denote individual flows within the MFU. The boundary between the MFU and LFU occurs at depth 162 m. (B) Rock Quality Designator (RQD) %, which is the cumulative percentage of the number of pieces of core that are larger than 10 cm over a distance of 1 m. (C) Number of fractures per metre length of core.

5.5.4. MORPHOMETRIC ANALYSIS – VALLEY CROSS-SECTIONS AND HYPSOMETRY

The scoured bedrock basin cross-sections generally have narrow steep valley sides with flat bottom valley floors, whereas the till blanket basins have lower valley slopes and wider valley bottoms (Figure 5.7, A, B). The scoured bedrock basin valleys have broad gentle slopes in their headwaters and narrow steep valleys closer to their outlets where incision into the more resistant LFU occurs (Figure 5.7, A). The till blanket basins have lower slopes and wider valley bottoms along their entire length (Figure 5.7, B). Representative cross-sections midway upstream of each basin show the narrower valleys associated with the scoured bedrock basins compared to the broader valleys and gentler hill slopes associated with the till blanket basins (Figure 5.7, C). The hypsometric curves and integrals of the scoured bedrock and the till blanket end-member basins show subtle differences from one another (Figure 5.8). The scoured bedrock basins have higher proportions of lower elevations compared to the till blanket basins and have the largest range of proportion of higher elevations. The scoured bedrock basins have HI = 0.71-0.74, and the till blanket basins have HI = 0.63-0.72, with those farthest east in the till blanket area having a HI = 0.65 – 0.68 (Figure 5.8). Brocklehurst and Whipple (2004)

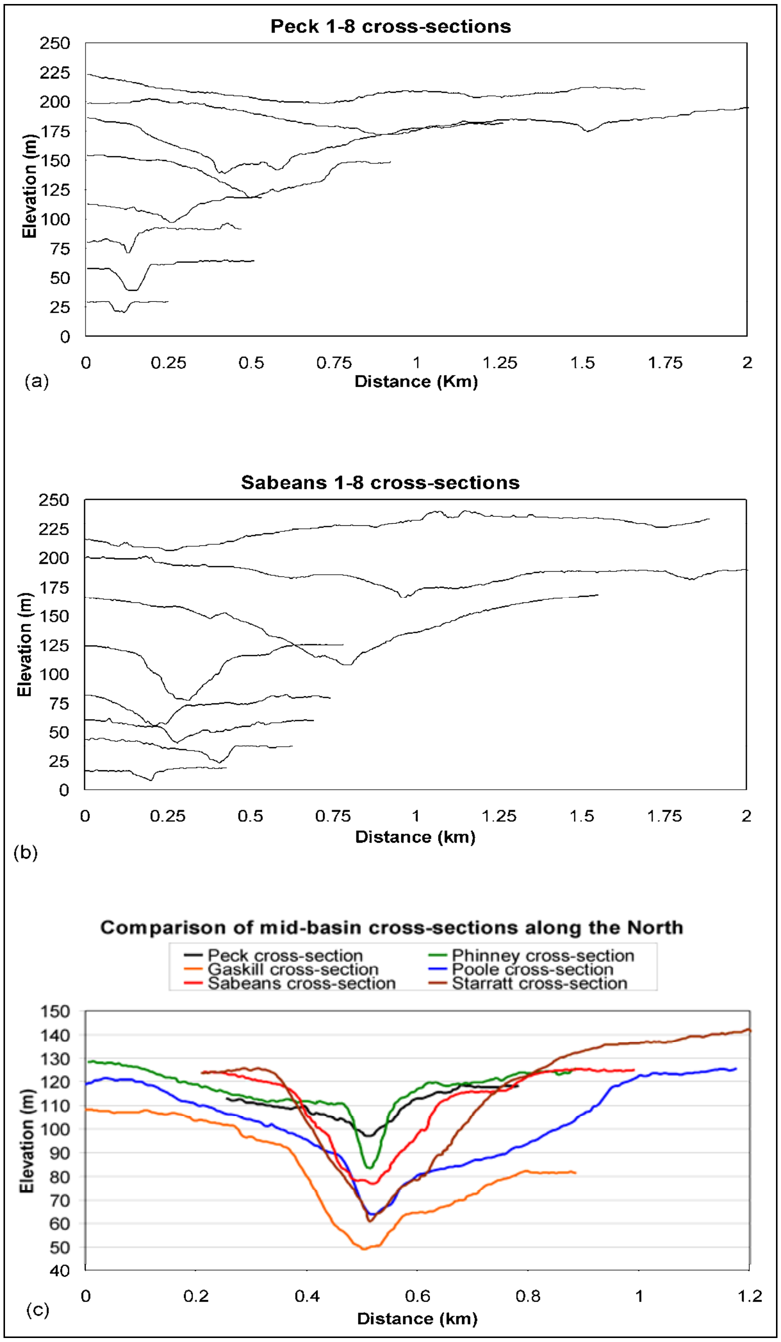

Figure 5.7 Representative stream valley ridge-to-ridge cross-sections for basin end-members. Cross-section locations evenly distributed across the basin, from the outlet to near the headwaters. (A) Valley cross-sections 1-8 for Peck Basin in the scoured bedrock area. (B) Valley cross-sections 1-8 for Sabeans Basin in the till blanket area. (C) Mid-basin cross-sections for all the basins on the North Mountain (black lines – basins in scoured bedrock area, grey lines – till blanket areas). Cross-sections have been offset to facilitate comparison of form.

state the HI for fluvial systems falls between 0.3-0.6, and full alpine glaciated systems have HI = 0.625. The variations in the hypsometric curves are consistent with the valley cross-section shapes and are attributed to the effects of over-deepening from glaciation and the subsequent fluvial incision into the glacial till blanket.

The erosion map highlights the differences in morphometry between the scoured bedrock and till blanket basins (Figure 5.9). The scoured bedrock basins have narrow incised valleys along their entire length and consist of only one main reach. The till blanket basins have broader valleys with more contributions from larger tributaries. This map highlights the spatial pattern of incision into the different bedrock lithologies (white lines on Figure 5.9) over the entire basin rather than just along the stream incision profiles (Figure 5.5). Statistics associated with the erosion depth map include the areal extent of each erosion depth and the volume of material removed for each depth (Figure 5.10). The erosion depth area and volume graphs show differences in the distribution of removed material from the scoured bedrock basin end-members (Peck and Phinney catchments) to the till blanket basins end-members (Figure 5.10, A, B). Calculations of the total area and volume of material eroded indicate that the transition zone and till blanket basins have the largest eroded volume compared to the scoured bedrock basins (Figure 5.10, C) (Table 5.4). The most sediment removed is associated with the Starratt catchment that is covered by the thick till blanket (Table 5.4). The volume of sediment removed for the rest of the catchments follow a similar trend as the incision depths, with the catchments within the transition zone having the most sediment removed and the least

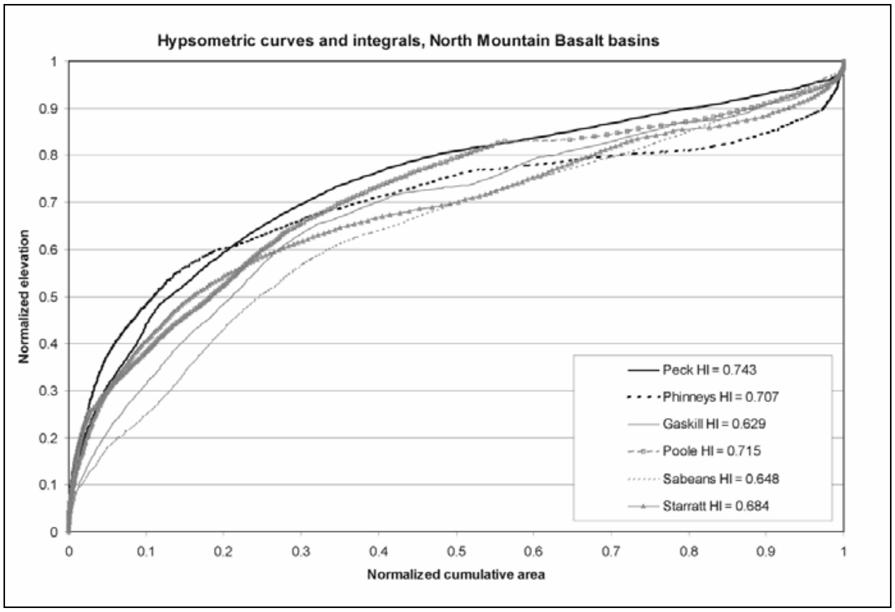

Figure 5.8 North Mountain basins hypsometric curves and integrals (HI). Scoured bedrock basins (black lines) and the till blanket basins (grey lines).

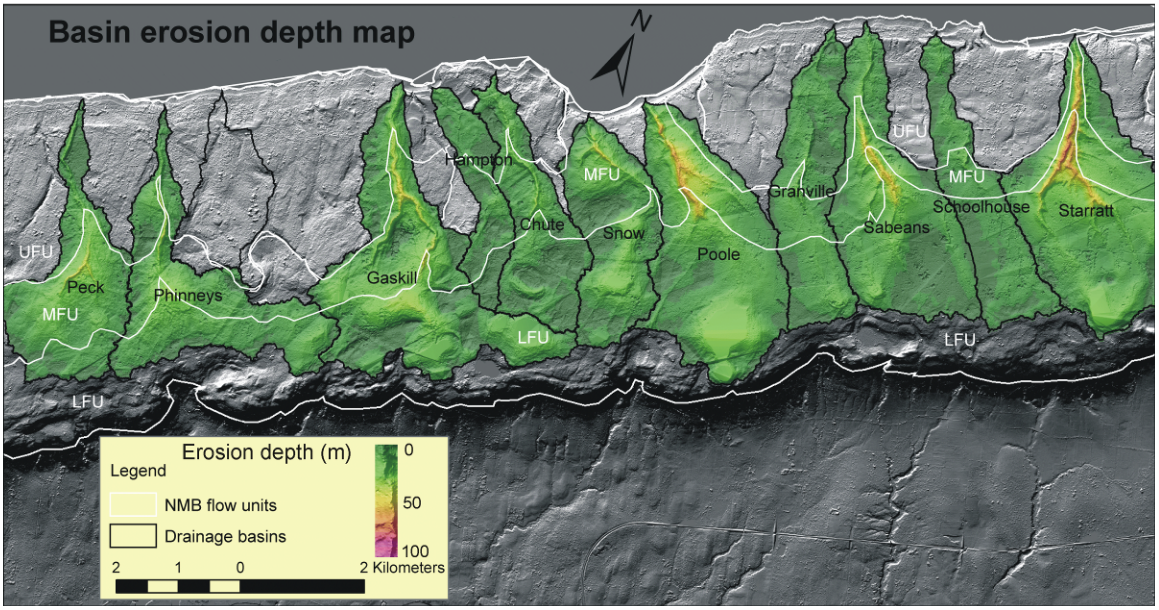

Figure 5.9 North Mountain drainage basin erosion depth map with basalt flow unit boundaries. The western basins have incision depth maximums of approximately 50 m and the central and eastern basins have maximum incision depths approaching 100 m.

sediment removed in the thin till cover catchments (Table 5.4). Although the ratio of eroded volume to area is highest in the scoured bedrock basins. Figure 5.9 shows the spatial variability of the volume of sediment removed increasing from west to east basins with increasing till cover as indicated by the deeper level of erosion.

Table 5.4 Catchments grouped by the amount of till cover and sediment volume removed. Maximum sediment flux per catchment.

Catchment	**Till cover**	**Volume of sediment removed km^3**	**Maximum sediment flux (km^3/ka) assuming erosion started at 12 ka.**
Peck	Thin veneer	38.3	3.2
Phinney	Thin veneer	37.4	3.1
Gaskill	Transition zone	81.8	6.8
Poole	Transition zone	91.7	7.6
Sabeans	Thick blanket	47.3	3.9
Starratt	Thick blanket	98.3	8.2

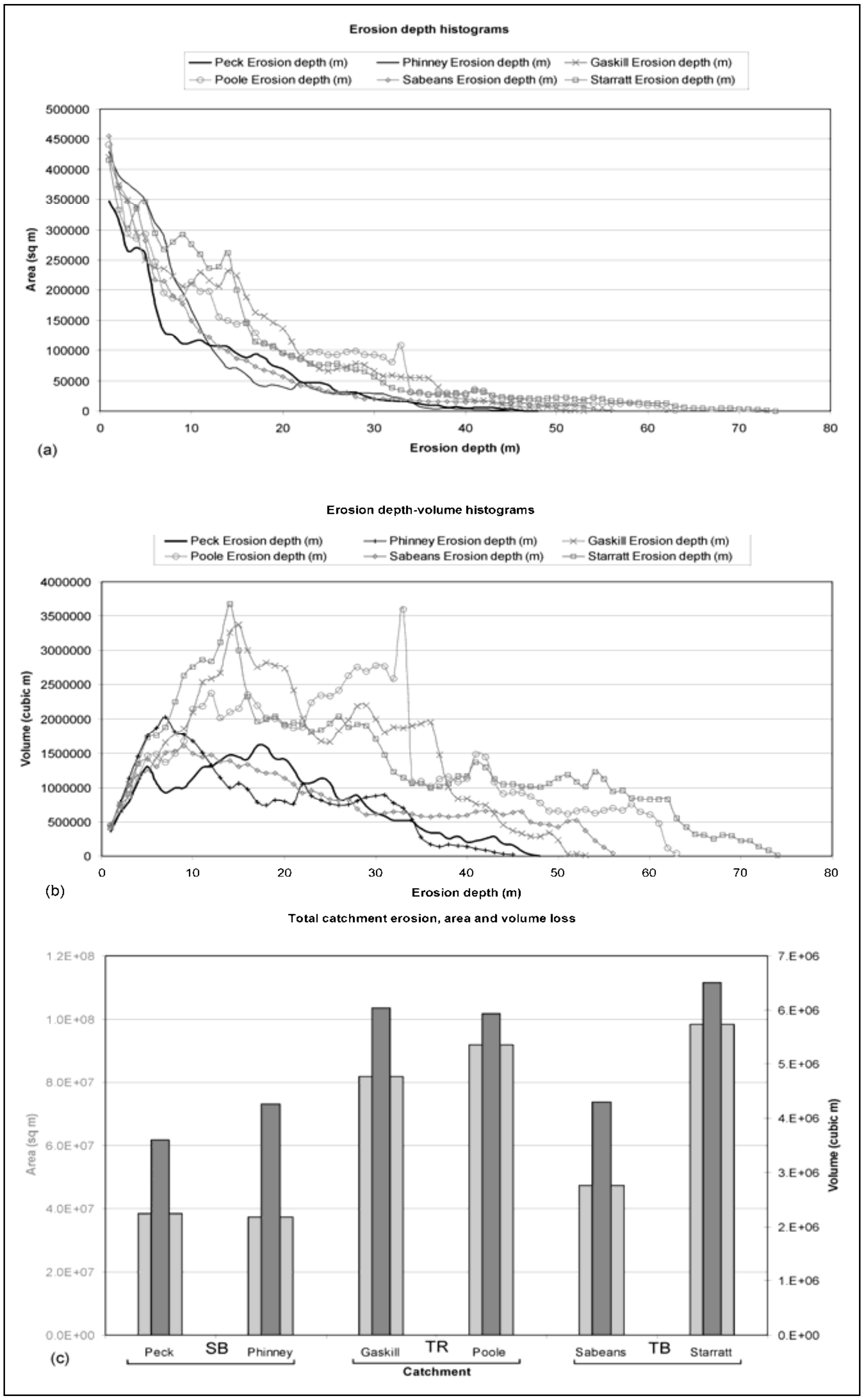

Figure 5.10 Graphs of area and volume of erosion for each basin along the NMB. (A) The area of different erosion depths. The till blanket basins have more area eroded at deeper depths. (B) Erosion volume removed for each depth of the basins. (C) Total area and volume of eroded material for each basin. The thicker light grey bars represent total area (left axis) of material removed per basin and the thinner dark grey bars represent the total volume (right axis) of each basin.

5.5.5. EROSION RATES

Maximum incision rates and sediment flux erosion rates have been calculated for the catchments based on the following assumptions: (1) fluvial incision began after deglaciation, reported to be at 12 ka ± 220 yrs by Stea and Mott (1998), and (2) the till cover was originally flat. The rates are maxima because the tills probably had some relief and incision may have started prior to this time. The rates represent preferential erosion of till relative to bedrock. These rates can vary up to 12.4% based on the accuracy of the methods used to calculate incision depth and the date of deglaciation. The maximum incision rate is highest in the catchments within the transition zone at 3.7 and 3.5 km/Ma, followed by the catchments covered by the thick till blanket at 3.2 – 2.7 km/Ma and lowest for the catchments covered by a thin till veneer at 2.4 – 2 km/Ma (Table 5.3). The maximum sediment flux removed from the catchments follows a similar pattern, except it is highest in the Starratt catchment at a rate of 8.2 km^3/ka followed by the catchments in the transition zone and is lowest in the catchments covered by a thin till veneer (Table 5.4).

Raised beaches along the Bay of Fundy dated between 14 to 12 ka (Stea and Mott, 1998) are present along the coast in the till blanket area (Webster et al., in review). Along with the terraces cut into the till, channels draining into the bay cut across these terraces to the bedrock with incision depths of approximately 8 m. An assumption that these channels began to incise at 12 ka to a depth of 8 m requires an incision rate of 0.7 km/Ma for the till and reworked beach deposits.

5.5.6. SURFACE AND GROUNDWATER INTERACTION

The normalized hydrographs of Peck and Sabeans catchments show a sharp contrast in discharge after a rainfall event, being higher in Sabeans catchment than in Peck catchment (Figure 5.11, A). The response time of the hydrographs between the two catchments is similar. However, the normalized discharge of Sabeans is greater than Peck and may be attributed to different rates of evapotranspiration between the catchments since Peck has more forest cover and less cleared agriculture land than Sabeans. The water in Sabeans Brook is generally more turbid after a rain event than in Peck Brook. However, the specific conductance in Sabeans Brook decreases after a significant rain event, whereas it increases in the Peck Brook after the rain event (Figure 5.11, B). Based on the hydrographs, Sabeans Brook receives more overland flow than Peck Brook after a rain event. The dominant hydrologic process of overland flow for Sabeans catchment and infiltration for Peck catchment is consistent with the results of the water chemistry data (Figure 5.11, B). The higher turbidity in Sabeans Brook compared to Peck Brook is likely to be a result of till material washing into the stream from the bank in Sabeans catchment. The decrease in specific conductance of the water in Sabeans Brook after a rain event is considered to represent dilution, and the increase in Peck Brook is representative of increased base flow of water that has had a longer residence time in contact with the bedrock (Hem, 1985; Winter et al., 1998). The dominant process of overland flow in Sabeans catchment compared to infiltration in Peck catchment is attributed to the low permeability of the Lawrencetown Till blanket that covers the Sabeans catchment area.

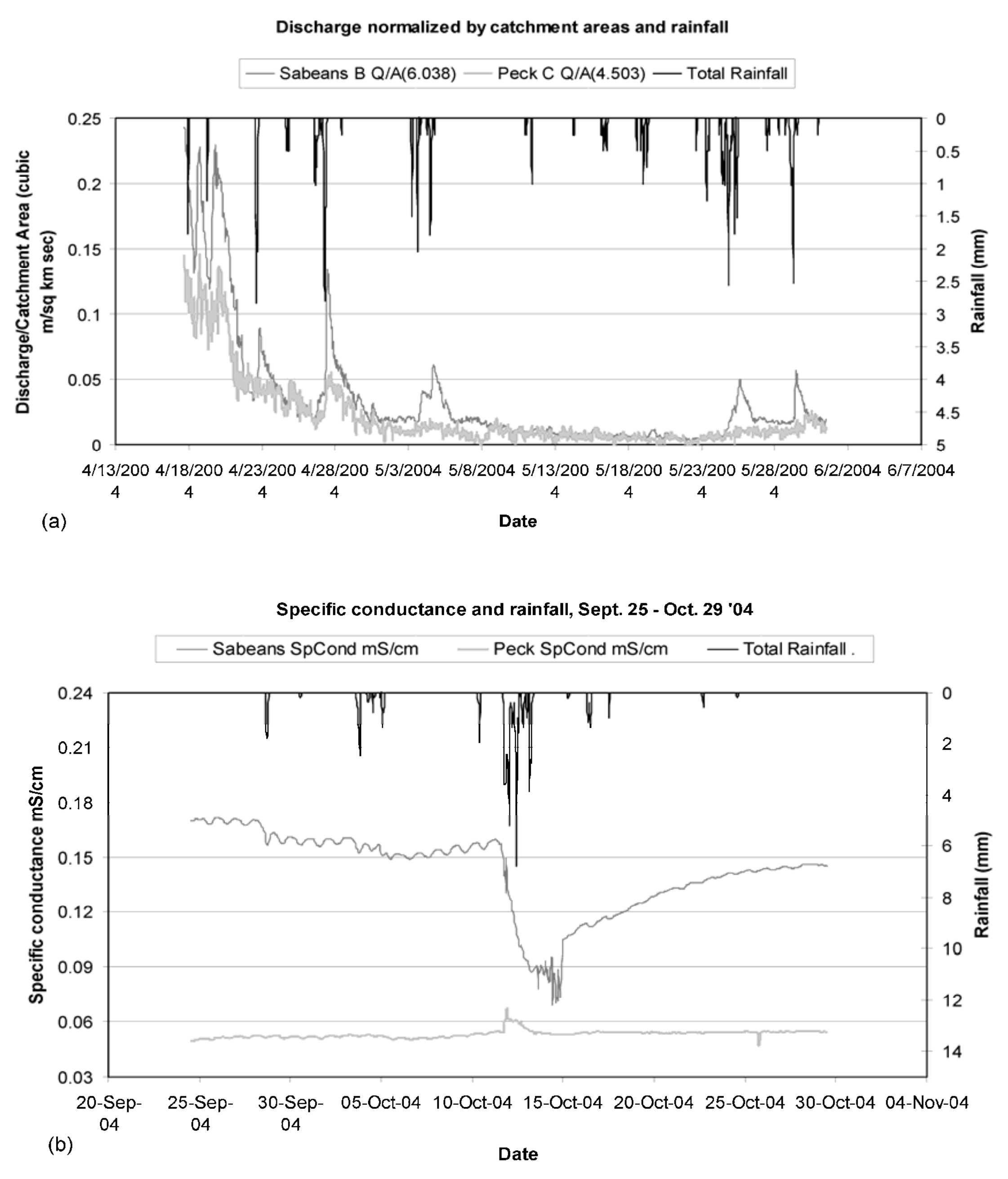

Figure 5.11 Hydrographs and water chemistry plots of representative basins from the till blanket area (Sabeans Basin dark grey) and the scoured bedrock area (Peck Basin light grey). (A) Hydrographs of Sabeans and Peck basins, discharge m^3/sec normalized by basin drainage area (km^2). Rainfall (mm) is plotted in reverse order on the right y-axis. (B) Specific conductance (microseimens per centimetre) and rainfall for Sabeans and Peck brooks.

5.6. DISCUSSION

5.6.1. LANDSCAPE DEVELOPMENT AND STREAM INCISION METRICS

Stream incision depth curves (Figure 5.5) reveal that the bedrock lithology has a significant influence on the stream's ability to incise, with the largest incision depths associated with the MFU, then the LFU and UFU. Sklar and Dietrich (2001) have shown in laboratory experiments that rock erodibility has a significant effect on erosion. Whipple et al. (2000*a, b*) presented qualitative evidence on the relative efficacy of fluvial erosion processes including plucking, abrasion, cavitation, and solution, and confirmed the strong influence of lithology on erosion, and that joint spacing, fractures, and bedding planes exert the most direct control on plucking. This study demonstrates that rock-type plays a critical role and significant variations in stream profiles can occur within a small region depending on the local structural and base level conditions. Based on the shatterbox experiments (Table 5.2) and observations of the fracture density of the flow units in the field and in drill core (Figure 5.11), it is proposed that the MFU erodes by abrasion and plucking, and the LFU erodes by plucking of blocks along fractures. The layering of the thin flows of the MFU also makes it less resistant to erosion than the other flow units. The UFU appears to be the most resistant unit to both processes.

Although the stream longitudinal profiles were presented based on the degree of till cover in each catchment, the dominant control on knick zones appears to be bedrock lithology. Pazzaglia et al. (1998) and Weissel and Seidl (1998) demonstrated that rock-type and structure play an important role in the persistence of knick points over geologic time. The UFU acts as a cap rock along the coast to minimize erosion upstream in the catchments. In basins where the UFU has been breached and the MFU exposed at base level or near the outlet, a cliff is developed at the coast and the erosion depth along the stream is increased for this unit. The most pronounced knick zones occur in the Poole and Starratt brooks long profiles (Figure 5.4). In both of these catchments, the UFU has been breached and the MFU has been eroded to near base-level in the streambed and is surrounded by cliffs at the outlet, and occur in coastal embayments (Figures 5.1, 5.2). The increased erosion associated with the MFU appears to be the dominant process involved in the migration of these knick zones from the coast upstream. Although we propose that bedrock lithology is the dominant control on incision, the most pronounced knick zones occur in the streams of catchments that are associated with the thickest till blanket (including the transition zone), suggesting that the glacial till may enhance fluvial incision rates by providing extra tools in the form of gravel to promote abrasion, as proposed by Sklar and Dietrich (2001). The increased turbidity of Sabeans Brook during rainfall events attests to till material washing into the stream. Thus, it appears that the thickness of glacial till cover may influence a fundamental process such as knick zone development and fluvial incision.

Although the rate at which the knick zones migrate upstream is unconstrained in this study, Seidl et al. (1994) calculated a migration rate of 1000 m/Ma based on geomorphic evidence from 5.2 Ma basalts in Hawaii. Seidl et al. (1997) used cosmogenic dating on the same basalts and calculated a migration rate of 400 m/Ma. Reneau (2000) observed that Holocene incision was variable based on the lithology of 1.22 Ma basalt, and an altered unit was more resistant than a zeolite-rich unit which caused knick points to occur. He proposed that the resistant basalt provided local base-level constraints and isolated the watershed from base-level changes along the Rio Grande. The UFU may act in a similar way to protect the MFU from base-level changes. Base level has changed frequently in our study area with the most recent low stand of –40 m between 12 – 7 ka (Stea and Mott, 1998), and may have aided in the development of sea cliffs and the migration of knick zones. However, it is unlikely that these knick zones developed during this low stand, since migration rates of the knick zones for Poole and Starratt brooks would have to have been 53 and 149 km/Ma respectively. Thus, the knick zones must have developed earlier and began their migration upstream, and were possibly accelerated during this low stand.

The fluvial incision rates calculated in this study are maximum rates as discussed earlier and range from 2 – 3.7 m/Ma, and represent erosion of till and bedrock. The highest fluvial incision depths are associated with the catchments with thicker till cover, however when the depths are normalized by catchment area they are very similar with a mean value of 5.4 m/km^2 and a standard deviation of 0.5 m/km^2. This suggests that the thickness of glacial till does not have a significant effect on fluvial incision rates, or that the streams within the thick till covered catchments have not caught up with those in the thin till cover catchments. This latter possibility is consistent with field observations that indicate streams are presently incising into till in some of the streambeds within the thick till covered catchments. The maximum incision rates we report are 1-2 orders of magnitude less than other studies have shown that have examined basalts in unglaciated terrains that range from 10 – 250 m/Ma (Montgomery and Lopez-Blanco, 2003).

5.6.2. BASIN MORPHOMETRY

The larger catchments are associated with the thicker till cover (Figure 5.9, Table 5.1) and have higher rates of sediment flux calculated (Table 5.4) even after the removed sediment volumes have been normalized by catchment area. The variation in sediment volume removed in these catchments (Table 5.4) is consistent with the variation in morphometry measurements (Figures 5.8, 5.9). Others (Kirkbride and Matthews, 1997; Li et al., 2001) have examined valley cross-sections to show differences in shape between glaciated and non-glaciated valleys. In this study, the glacial processes appear to have over-deepened and widened the catchments in the eastern region of the study area where the till blanket is thickest (Figure 5.7) (Hallet et al., 1996). The basin morphometry appears to be related to different amounts of glacial till cover and its influence on surface and groundwater interaction, which has an effect on fluvial processes. This is consistent with the hypsometries (Figure 5.8) between the catchments.

Strahler (1952) proposed that the hypsometric integral decreases as a landscape matures during post-orogenic decay. Plateaus with steep canyons have HI = 0.68, and fall into the youthful category, whereas S-shaped hypsometric curves with HI close to 0.5 are considered mature (Strahler, 1952). The two end-member basin types in this study have subtle differences in their hypsometry.

The erosion depth map shows the combined effect of variable bedrock lithology on stream incision and the effect of glacial till cover on basin morphometry (Figures 5.8, 5.9). The spatial pattern of the eroded material in the scoured bedrock basins consists of a single dominant channel that is very narrow and deepest within the MFU (Figures 5.5, 5.9). The erosion depth map indicates that the basins in the transition zone and with the thicker till cover are more deeply incised than the scoured bedrock catchments (Figure 5.9). The erosional depth of the till blanket catchments appears to be the greatest and have the most developed drainage systems (Figure 5.9). This is a result of the combined effects of the amount of the MFU exposed in the streambeds and the extra till material deposited on the surface. The till blanket catchments have more tributaries contributing to the main trunk stream than the scoured bedrock catchments (Figure 5.9, Table 5.1). These smaller tributaries are a result of enhanced post-glacial fluvial processes by increasing surface runoff in the thick till blanket catchments eroding the till into the underlying bedrock as observed in the stream discharge and water chemistry results (Figure 5.11).

5.6.3. SURFACE AND GROUNDWATER INTERACTION

Pazzaglia et al. (1998) pointed out that stream power can control the shape of the stream longitudinal profile and that discharge is influenced by the drainage area and infiltration characteristics of the basin. Many studies have used drainage area as a surrogate measure for stream discharge (Sklar and Dietrich, 1998; Snyder et al., 2000; Kirby and Whipple, 2001; Whipple and Tucker, 2002; Mather et al., 2002; Finlayson and Montgomery, 2003; Stock et al., 2005) in estimating stream power. Montgomery (2002) used drainage area as a normalizing parameter to compare metrics of valleys affected by variable degrees of glaciation. Where basins are being compared, the use of drainage area to estimate discharge assumes that hydrologic processes affecting discharge in those basins are similar. Although this assumption may be true at a regional scale (1000 km^2

and larger), our results indicate that there can be significant variations in hydrologic processes between basins within a region (<100 km^2) and that drainage area may not accurately scale to discharge as it relates to stream incision. Monitoring the hydrographs and water chemistry of catchments from two basins with contrasting amounts of glacial till and land cover demonstrate the effects of the glacial till on surface and groundwater interaction and the influence on stream discharge. The differences in the hydrographs are a result of the amount of surface runoff that each catchment area delivers to the stream. The till blanket catchments promote surface runoff because of the low permeability of the till material, whereas the scoured bedrock promotes infiltration and delivers water to the stream by increased base flow. This is consistent with the findings of Tague and Grant (2004) who observed that hydrographs from basins in older volcanic rocks were much flashier than those with younger, more permeable volcanic rocks in the Cascades of Oregon.

The Lawrencetown Till consists of 20-30% gravel, 30-40% sand, and 30-50% mud (silt and clay) and the permeability of the till is < 10^{-6} (cm/sec) makings it suitable for liners in landfill sites and other structures that require low permeable material (Lewis et al., 1998). Although there are no direct permeability measurements for the basalt flow units that we are aware of, the MFU and LFU are highly fractured with densities of 7 and 10 fractures per metre, respectively (Figure 5.6). Haan et al. (1994) reported a range of hydraulic conductivities for fractured basalt to be between 10^{-6} and 10 (m/day) with lava flows up to 10^{4} (m/day) and glacial till to be between 10^{-7} and 1 (m/day) and clay between 10^{-7} and 10^{-3} (m/day). Rose (2004) reported hydraulic conductivities for fractured bedrock to be between 10^{-8} and 10^{-4} (m/sec) and clay to be between 10^{-10} and 10^{-8} (m/sec).

Pump tests from water wells within the basalt aquifer yield an average of 14.4 imperial gallons per minute (10 wells) and are prone to surface contamination where the till cover is thin (D. Fanning personal communications, 2004). These data further support our interpretation that the low permeable till blanket promotes surface runoff and the scoured fractured bedrock promotes infiltration of precipitation. With increased overland flow, more water enters the stream more quickly after rain events and increases the overall discharge and stream power, thus enhancing the stream's ability to erode. This study demonstrates that for glaciated terrains, factors such as a till can affect the hydrologic properties of a catchment and there can be a high degree of variability in surface and groundwater interaction within a small region that can affect stream discharge. This has important implications on issues related to water quality and quantity in glaciated terrains.

5.7. SUMMARY

Landscapes within the study area are typical of those found in the northeastern Appalachians or other ancient mountain belts that have been significantly eroded. The terrain is also representative of many areas in the world that have been eroded by fluvial process for millennia and during the Quaternary by glacial processes. This area is an ideal site to examine factors controlling landscape evolution. The catchments are all generally the same size, are underlain by similar lithologies with relatively simple structures, and have experienced the same changes in base level. This facilitates an examination of the effects of glacial till within a region on moderate scale catchments. Studying the morphometry of catchments at this scale allows us to distinguish factors affecting hydrologic and geomorphic processes that can be used to scale our findings up to larger basins.

Terrestrial LIDAR has been a valuable tool in the analysis of these moderate scale catchments and stream morphometry within a forested region. In addition to basin morphometry, the ability of the laser system to generate high-resolution precise terrain heights in heavily vegetated terrains has facilitated the identification of geologic contacts within the basalt units and the identification of new landforms interpreted to be related to late stage ice dynamics and fluctuations in sea level. The precision of the LIDAR has also allowed for detailed incision depths to be calculated that are controlled by variations in the erodability of the basalt flow units. The thin flows and high concentration of vesicles and amygdules has lowered the middle flow unit's ability to resist erosion from abrasion compared to the UFU and LFU. The LFU is resistant to abrasion as demonstrated in the shatterbox experiments, however it has a high fracture density and plucking is the dominant erosion process removing material from the streambed. The UFU is resistant to abrasion and the fractures in this unit appear to be sealed by secondary minerals. In general the incision depths are the lowest for this unit, and it acts as a cap rock protecting the MFU from erosion and the development and migration of knick zones.

The catchments with the thickest till cover have had the most sediment eroded from them and differ in their morphometry and hypsometries compared to the scoured bedrock catchments. In addition, the catchments in the till blanket area have higher drainage densities and deeper fluvial incision depths. We attribute these differences in catchment morphometries to be a result of the influence of the glacial till on hydrologic and fluvial process and the possible addition of more tools in the streambed to promote erosion by abrasion. The till has a significant effect on the surface and groundwater interaction by promoting overland flow and retarding infiltration. The process of infiltration dominates the scoured bedrock catchments during precipitation events where water is filtered through fractures into the groundwater table and released as base flow into the stream as evident from the hydrographs and water chemistry data. The MFU and LFU are both highly fractured with an average of 7 and 10 fractures per metre respectively allowing infiltration in the thin till catchments. In the catchments with thick till cover, the increased overland flow results in higher discharge and stream power per unit area compared to the thin till covered catchments. This has important implications in glaciated terrain if drainage area is used as an approximate measure of discharge as is commonly the practice.

The results of this study are widely applicable to other glaciated terrains where vegetation cover obscures the topography. The ability of LIDAR to penetrate the vegetation canopy makes it the ideal tool for determining catchment morphometries in such areas.

5.8. ACKNOWLEDGEMENTS

We would like to thank Ralph Stea and Dan Kontak of the Nova Scotia Department of Natural Resources for field visits and discussions; field assistants to TW (Alex Mosher, Adam Csank, and Daniel Roberts). We would like to thank Thomas Duffet of

CHAPTER 6. SUMMARY AND CONCLUSIONS

6.1. INTRODUCTION

This chapter provides an overview of the applications of high-resolution laser altimetry (LIDAR) to geological problems such as bedrock and surficial geology mapping and local surface processes in the Fundy Basin of Nova Scotia. A more detailed synthesis has been submitted to the Canadian Journal of Remote Sensing (CJRS) and is currently under review. Much of the material in this synthesis has been presented in previous chapters and is not repeated here. Some new material, however, involving error analysis of stream longitudinal profiles extracted from LIDAR, the application of principal component analysis to shaded relief maps, and the identification of additional wave-cut terraces along the coast, which is included in the submission to CJRS is presented herein and complements some of the interpretations in the previous chapters. This new material is presented first and is followed by a summary of the main conclusions of the thesis.

6.2. ERROR ANALYSIS OF GRID CELL SIZE AND STREAM PROFILES

Zang et al. (1999) and others have pointed out that the grid cell size affects DEM accuracy. To test this, the GPS points collected along roads (chapters 2 and 3) were overlain on DEMs derived from LIDAR and photogrammetric sources at variable resolutions to determine the effect of grid cell size on error. The relationship between error and grid cell size is an important consideration when dealing with high-resolution datasets. With increased resolution, file size increases and computational processing time also increases.

Stream metrics can be extracted from a DEM using a variety of GIS methods as outlined in chapter 5. These methods range from automatically deriving a stream network from the raster DEM directly, or by extracting elevations from the DEM for an existing stream network. Analysis of stream profiles derived from the different techniques is presented in order to determine which method is best suited for deriving landscape metrics.

In chapter 3, I highlighted the potential problem of misclassification of the LIDAR returns from low vegetation as 'ground' points. As pointed out by Hodgson et al. (2005), the classification of LIDAR points is important for geomorphic analysis, and can affect the accuracy of derived "bald earth" DEMs, especially in forested regions. In order to test how significant this error is when measuring stream metrics, traditional survey methods (total station) were used to measure a stream longitudinal profile and several channel cross-sections and compared to the LIDAR DEM. The magnitude of this error has important implications on surface process studies such as incision depth and derived incision rates (chapter 5, Webster et al., in preparation).

6.2.1. METHODS

To determine the effect on accuracy of different cell sizes, GPS validation points collected along roads were overlain on LIDAR-derived DEMs at variable resolution (2, 4, 10, and 20 m) and on DEMs derived from photogrammetric sources at variable resolutions. Contours with a 5 m height interval derived from 1:10,000 scale mass points have been interpolated to a 5 m DEM.

The 2 m LIDAR DEM was averaged down to a 4 m resolution to reduce disk space requirements and improve processing speed without a significant reduction in detail. This was based on the results of the GPS error analysis of variable grid cell DEMs derived from the LIDAR. A combination of Rivertools ™ and PCI Geomatica ™ software was used to extract the morphometric parameters from the catchment basins and stream longitudinal profiles from the 4 m DEM (chapter 5, Webster et al., in preparation). Catchment basin morphometries were calculated for the main streams draining into the Bay of Fundy from the LIDAR DEM using the standard D-8 algorithm (Jenson and Dominque, 1988; Costa-Cabral and Burges, 1994) in Rivertools™. The sinks (depressions within the DEM treated as errors by the algorithm) were filled in the DEM to allow continuous down stream flow and to compute stream flow direction and catchment basins. Most catchments had significant sinks that represented the upstream channel adjacent to the road network. A “notch” was cut across the roadbed and was assigned an elevation based on the nearest downstream elevation which allowed the generation of a more accurate flow direction and flow accumulation grid along with the basin boundary.

Longitudinal profiles of trunk streams derived from the 4 m LIDAR DEM were compared to profiles of trunk streams available from the 1:10,000 topographic maps that were overlain on the notched DEM prior to filling sinks. The long profiles of the trunk streams extracted from the DEM included elevations from the DEM before and after sinks were filled.

Real Time Kinematic (RTK) GPS checkpoints provided control for a total station survey of stream morphology. In general, the carrier phase real time differential GPS had a height precision of 5 cm or better. The stream longitudinal profile and stream cross section topographic surveys utilized a Leica total station with a precision better than 2 cm. The survey was conducted during leaf-on conditions and when base flow was low and much of the streambed was exposed.

6.2.2. RESULTS

Potential sources of error in LIDAR DEM data are a function of grid cell size and local slope (Zang et al. 1999). To test the variability of Δz with cell size, the GPS points were overlain on LIDAR DEMs of 2, 4, 10, and 20 m resolutions which results in standard deviations of Δz of 0.20, 0.32, 0.29, and 0.64 m respectively (Figure 6.1). These results likely do not reflect the accuracies expected under the canopy in variable relief terrain, as the GPS points were acquired on open road surfaces. The average slope within the catchment basins on the North Mountain is 6.4^{o}, thus at 4 m cells the expected error is ± 0.44 m. To compare similar DEM grid cell sizes derived from LIDAR and photogrammetric sources, the GPS points were overlain on photogrammetric DEMs of 5 and 20 m resolutions from 1:10,000 scale elevations and a 20 DEM from 1:50,000 CDED, which results in standard deviations of Δz of 2.07, 1.96, and 5.32 m respectively (Figure 6.1). This clearly demonstrates that the accuracy of the LIDAR, in open areas, is maintained as DEM resolution increases when compared to other sources. For example, the 20 m DEM derived from LIDAR has a mean Δ *z* of 0.18 m (σ = 0.64 m) compared to the 1:10,000 scale derived 20 m DEM that has a mean Δ *z* of 0.96 m (σ = 1.96 m), and the 1:50,000 scale derived 20 m DEM that has a mean Δ *z* of 1.43 m (σ = 5.32 m) (Figure 6.1). Based on these results and field observations, the 4 m LIDAR DEM was used to extract stream metrics.

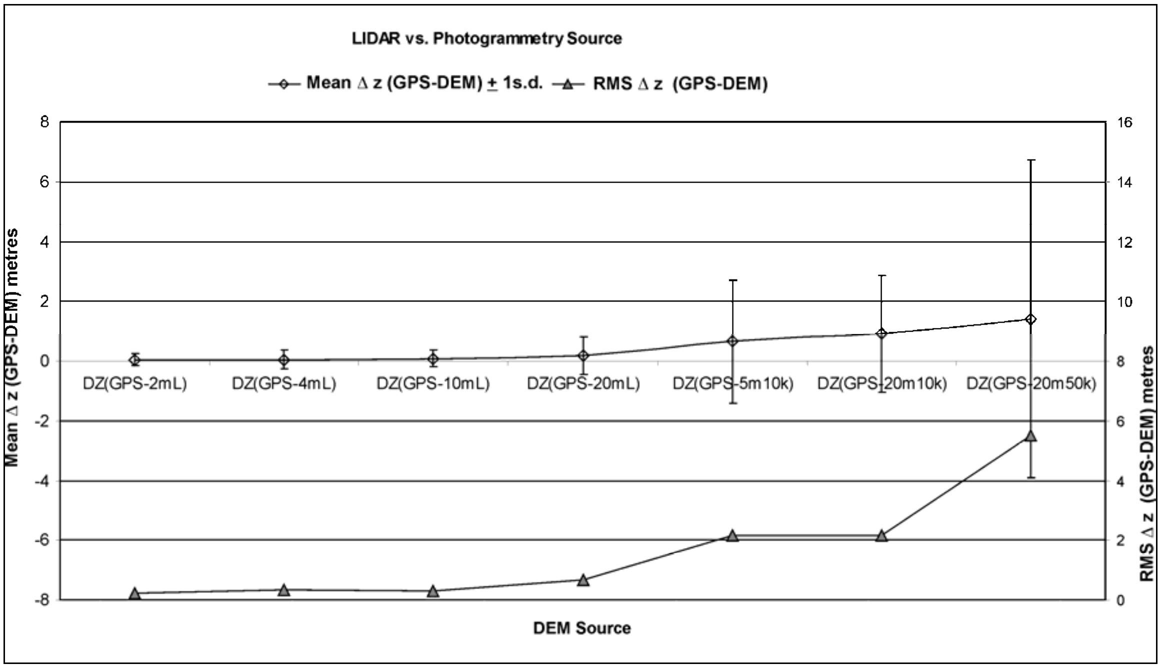

Figure 6.1 Error analysis of GPS points collected in open areas with variable resolution DEMs. LIDAR-derived DEMs of resolution 2, 4, 10, and 20 m are compared DEMs of 5 and 20 m derived from 1:10,000 scale (10k) elevations, and a 20 m DEM derived from 1:50,000 scale (50k) elevation. The mean Δ *z* ± 1σ are plotted on the left y-axis and the root mean square (RMS) error is plotted on the right y-axis.

The trunk streams derived from the 4 m LIDAR DEM are longer (i.e. more vertices defining a line) but do not extend as far upstream in the basins as trunk streams from the topographic map. In part this is a result of the fractal nature of stream lengths (Turcotte, 1992), but the greater lengths of the DEM-derived stream lines is also a consequence of the grid cell origin of the network compared to the straighter line segments on the map. Several flat areas resulting from sinks being filled were observed along the DEM-derived stream long profile even after the culverts were notched in the DEM (Figure 6.2). It was determined that longitudinal profiles obtained by using streams from the topographic map and the notched DEM prior to sinks being filled were the most representative based on field observations and were used for the rest of the analysis (see chapter 5).

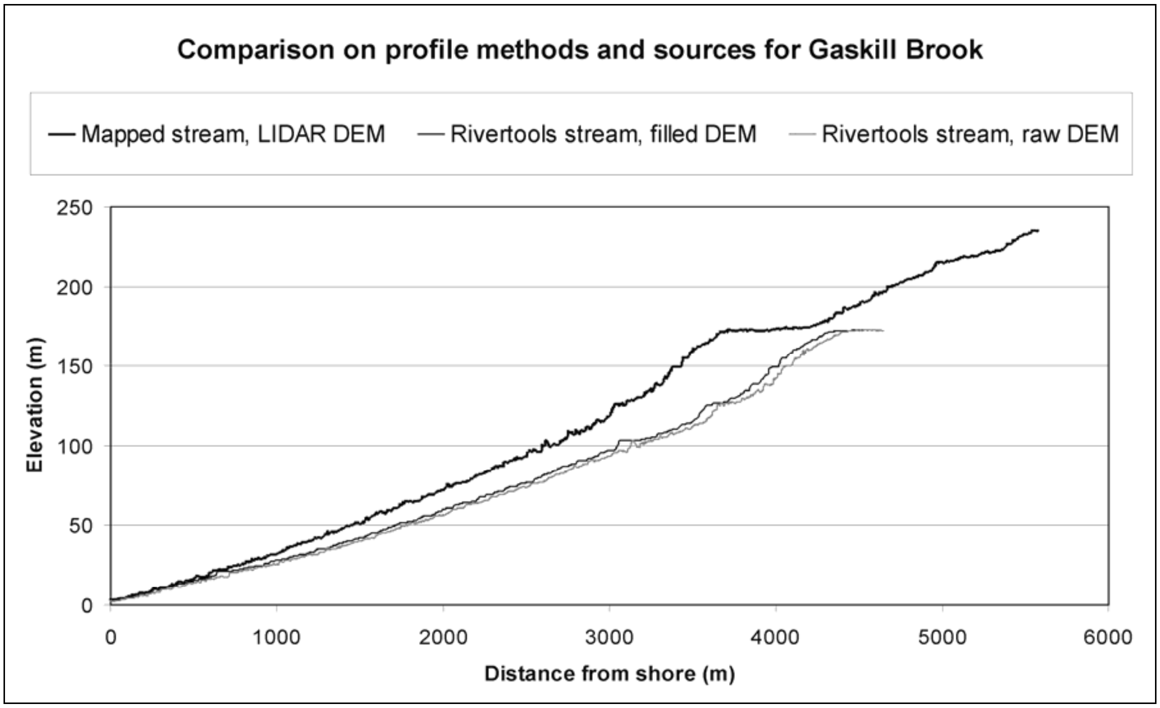

Figure 6.2 Comparison of stream longitudinal profiles for a typical drainage basin acquired by different GIS methods. The mapped stream from the 1:10,000 topographic map was overlain on the LIDAR DEM prior to filling sinks (thick black line). The streams extracted from the flow accumulation grid in Rivertools with the sinks filled in the DEM (thin black line) and the raw DEM prior to filling sinks (thin grey line). The mapped stream profile extends farther upstream into the basin and does not have as many “flat” sections as that of the filled DEM profile. The Rivertools^{TM} generated profiles have more vertices and thus appear ‘longer’ than the topographic mapped stream profile for a given section. This is a result the tendency of the Rivertools^{TM} stream network because of the raster origin (flow accumulation grid).

The results of the total station transect along the longitudinal profile of Sabeans Brook (chapter 5, Figure 5.2) indicates the DEM has several errors (Figure 6.3). The summary statistics indicate a mean Δz of -0.94 m, with a standard deviation of 1.26 m, and a RMS error of 1.57 m. The survey data matches the DEM within 0.5 m in many places, however it is too high by a few metres in other places (Figures 6.3, 6.4, B). When the anomalous sections are removed from the profile (survey points 32-101 and points 206-240), the summary statistics indicate a mean Δz of -0.28 m, with a standard deviation of 0.39 m, and a RMS error of 0.48 m. These results are similar to those observed in the forest transects across the crater structure (chapter 2 and 3). The most significant errors occur at a bend in the stream where the slope of the cut bank is steepest (Figure 6.3). Topographic cross sections are used to determine if the source of the error is related to a horizontal offset of the LIDAR data (Figures 6.3, 6.4). The cross sections extended farther than the survey data that are confined to the immediate banks of the stream channel. Based on cross sections (CS1 and CS3) north and south of the cut bank, it appears there is no significant horizontal shift of the LIDAR data since the channels are generally aligned (Figure 6.4, C, E). At cross section 2, the stream has eroded into the bedrock resulting in a narrower channel at this location (Figure 6.4, D). Field visits confirm that dense deciduous trees overhang the channel at this location (Figure 6.3) and are considered to be the source of the error. In areas of high error, the LIDAR points classified as ‘ground’ appear to be the dense overhanging vegetation (Figure 6.4, A) and no LIDAR returns made it to the streambed.

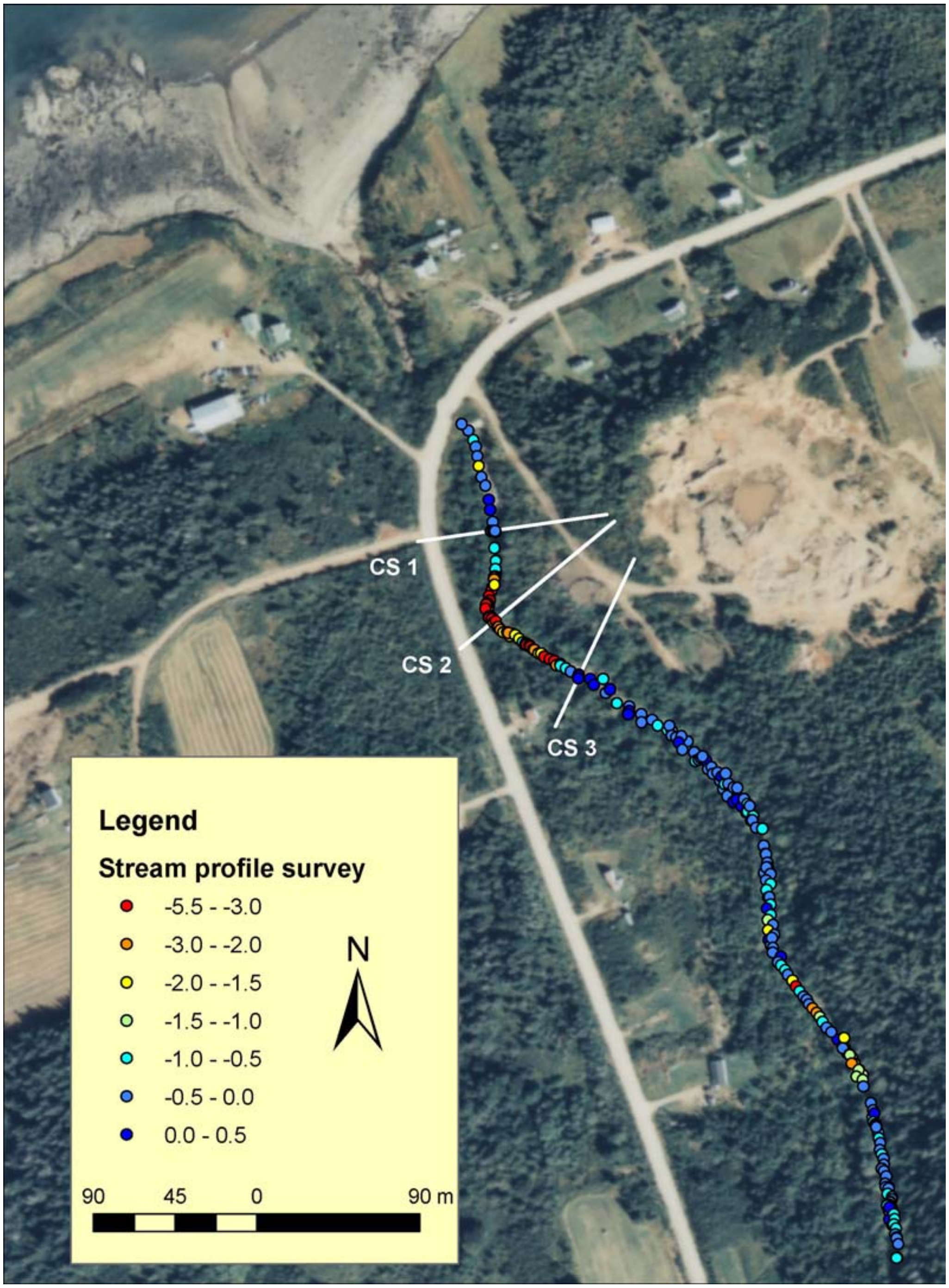

Figure 6.3 Colour orthophoto (1992) of Sabeans Brook near the outlet with total station (TS) survey points colour coded by Δ*z* (TS survey - LIDAR DEM) and cross-section locations (CS1, CS2, and CS3). The largest error in the LIADR DEM occurs at the bend in the stream where the bank is steepest. The large sand deposit east of the stream represents one of the raised beach deposits.

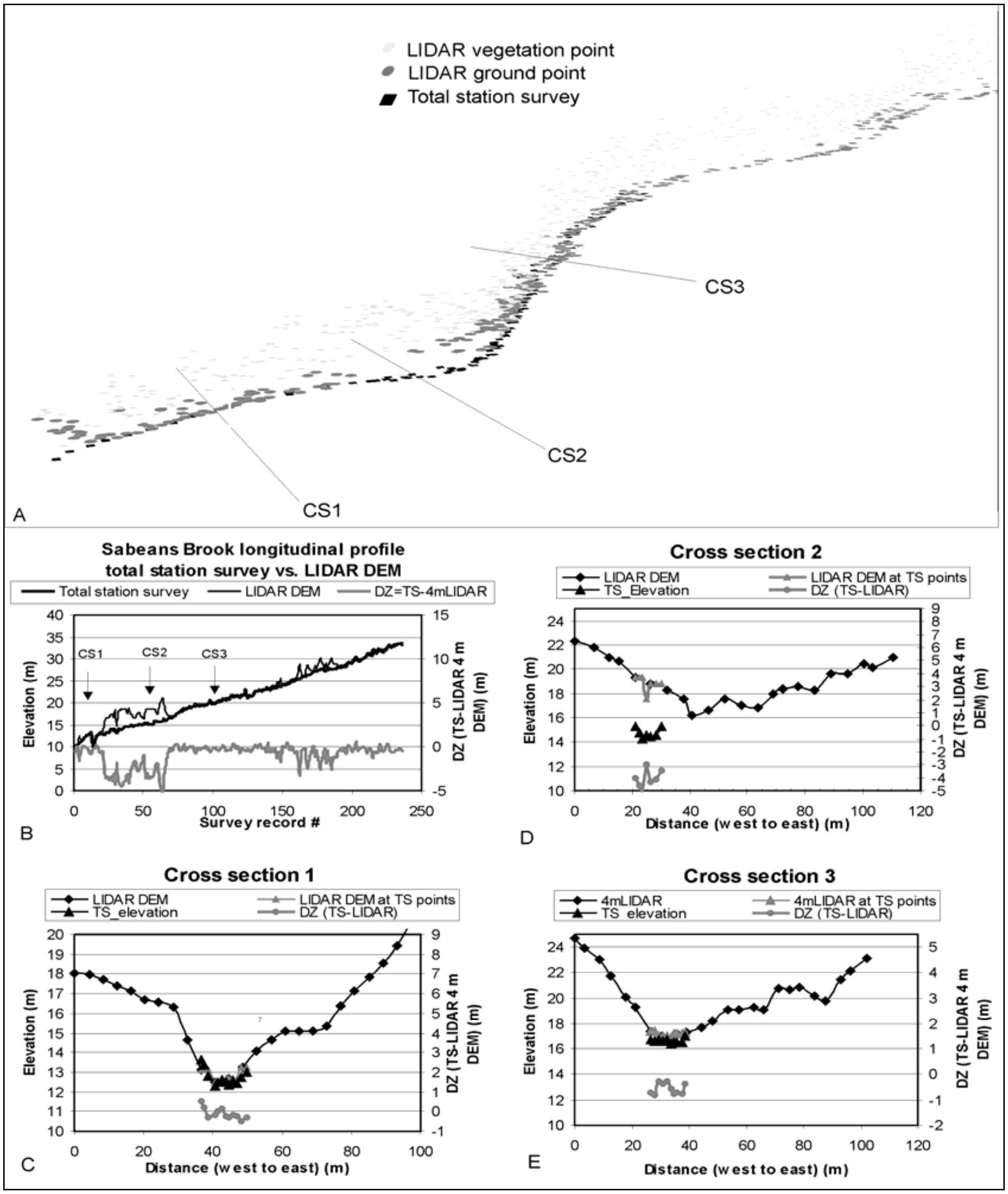

Figure 6.4 (A) Perspective view looking southeast of LIDAR ‘ground’ (dark grey points) and ‘non-ground’ (light grey points) with total station (TS) survey points (black squares) collected for the Sabeans Brook longitudinal profile. (B) Stream profiles derived from the TS survey (heavy black line) and LIDAR DEM (thin black line) and the difference (thin grey line) Δ*z* (TS survey – LIDAR DEM) on the right y-axis, and cross-section locations. C-E represent cross-section 1, and 3 respectively. Note Δ*z* denoted DZ on graph.

Discontinuities identified on the stream profiles similar to those highlighted in Figure 6.4 were investigated and the profiles were smoothed in areas suspected of having erroneous elevations for the streambed. In summary the maximum error related to this “bald earth” correction in the study area is 5 m and depends on the height of the dense canopy layer.

The DEM error in the streambed is the largest error encountered during the LIDAR validation procedure and has important implications for surface process rates (e.g. derived from incision depths). Given the magnitude of different sources of error, the most significant arise from low vegetation being classified as ground and areas of steep slopes.

6.3. APPLICATION OF PRINCIPAL COMPONENT ANALYSIS TO SHADED RELIEF MAPS

The penetration of laser shots through vegetation reveals subtle geomorphic features on high-resolution LIDAR-derived DEMs compared to that of the traditional DEMs derived from photogrammetry. However, visualization of the LIDAR DEM data in previous studies has been limited to grayscale shaded relief maps (chapter 4, Figure 4.5) or by applying colour coding schemes to the elevations and the generation of colour shaded relief maps (chapter 5, Figure 5.3). These methods suffer from the common bias of all shaded relief maps; only features that trend perpendicular to the illumination direction are highlighted. Paganelli et al. (2003) used principal component analysis (PCA) on RADARSAT-1 images (standard beam modes S1 and S7 in ascending and descending orbits) to enhance the interpretability of surface features for geological applications in northern Alberta. The PCA analysis reduced redundancy in the

RADARSAT-1 imagery and created new component images that enabled a structural interpretation of the geology to be conducted. In this study, the PCA technique has been applied to grayscale shaded relief images generated from the LIDAR DEM to enhance subtle topographic features regardless of their orientation.

6.3.1. METHODS

A Delaunay-triangular irregular network (TIN) was constructed from the ‘ground’ LIDAR points and a 2 m resolution “bald earth” DEM was interpolated from the TINs utilizing algorithms available within ArcGIS^{TM}. Colour shaded relief (CSR) maps were constructed in PCI Geomatica^{TM} by illuminating the surfaces from the northwest, perpendicular to the strike of the flow units, at a zenith angle of 45 degrees and a 5 times vertical exaggeration applied. Although the CSR DEM was useful for analyzing the contacts between flow units (Figures 4.4, 4.6), it was limited in highlighting some of the subtle lower relief landforms. A new map was constructed from the DEM with a shading azimuth angle of 225^{o}, to highlight northwest-trending landforms that may parallel one of the dominant ice flow directions in the area (chapter 5, Figure 5.3). The elevation colour ramp was repeated to optimize chromostereoscopy 3-D visualization (see Toutin and Rivard, 1995). The colour ramp is applied to the elevation range 0-100 m, and repeated for elevations 101-265 m in order to highlight the low relief landforms.

In order to overcome this directional bias in CSR maps, 8 grey-scale shaded relief images were generated from the LIDAR DEM with azimuth angles every 45^{o}, utilizing a constant zenith angle of 45^{o}, and 5 times vertical exaggeration. This method facilitates the highlighting of all dominant topographic features regardless of orientation. These relief images were analyzed using principle component analysis (PCA). The use of a PCA minimizes data redundancy inherent in the 8 shaded relief models and constructs new images that are characterized by a linear combination of the input images. The resultant component images are uncorrelated and ordered based on the amount of variance in each component image.

6.3.2. RESULTS

The first three components (PC 1,2,3) contain over 99% of the information (e.g. image variance) and were used to construct a composite image (Figure 6.5). This map highlights all the significant topographic features regardless of their orientation and no features appear lost to shadows or poorly illuminated surfaces. The colours of the composite image are complex to interpret. The output of principal component number 1 (PC1) contains the highest variance and has been projected in red for the composite image (Figure 6.5). The dominant landscape elements of the area are the North and South Mountains which trend northeast and most of the terrain surface faces northwest. As a result these northwest facing (aspect) surfaces dominate PC1 and appear in various shades of red in the composite image (Figure 6.5). Principal component 2 (PC2) contains the next highest degree of variance and is uncorrelated with PC1, and is projected in green in the composite image (Figure 6.5). The northwest trending features in the valley floor dominate this component (Figure 6.5). Principal component 3 contains the next highest degree of variance and is uncorrelated with PC1 and PC2, and is projected in blue in the composite image (Figure 6.5). The southeast facing slopes dominate this component, which are a less frequent element of the landscape (Figure 6.5).

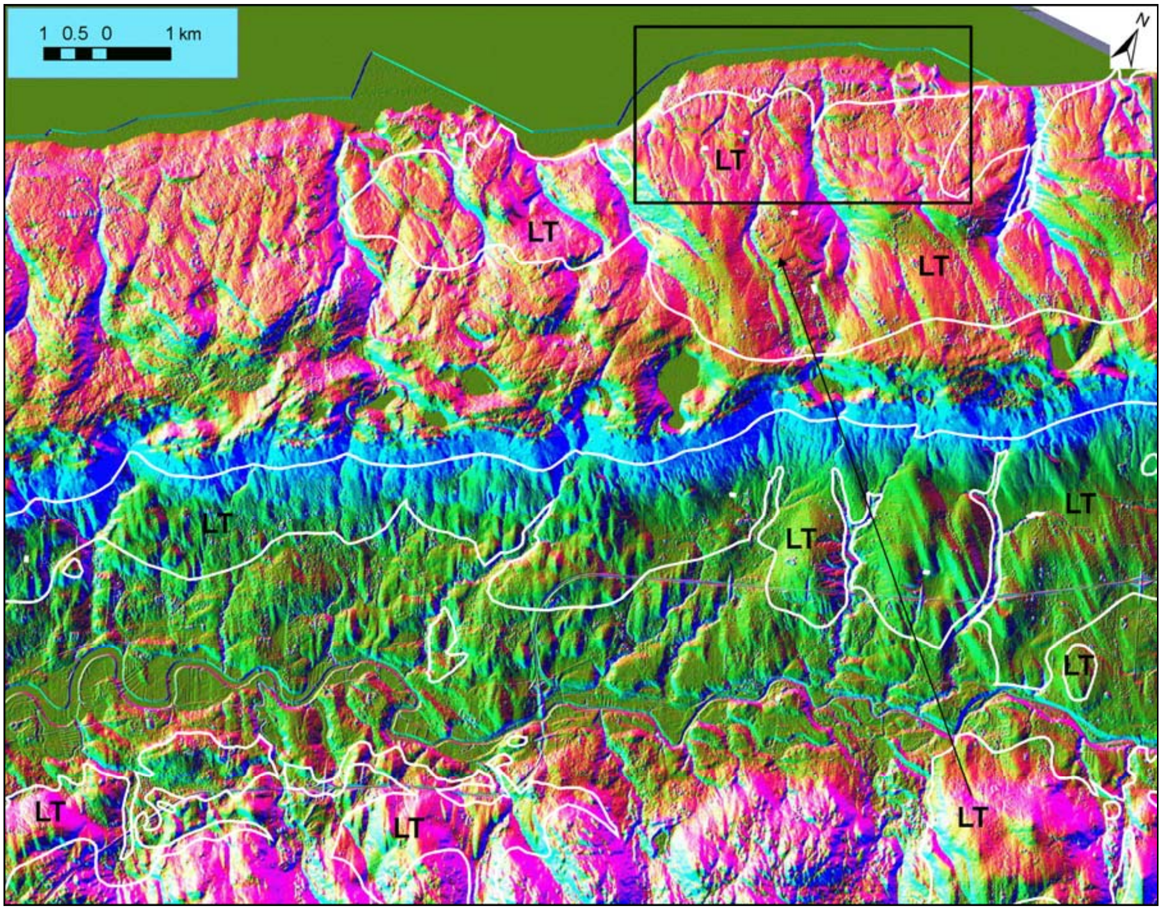

Figure 6.5 Principal component analysis composite image. PC 1, 2, 3 projected in red, green, and blue have been derived from shaded relief maps of the LIDAR DEM at the 8 cardinal directions with azimuth angles of 45^o and 5 time vertical exaggeration applied. Lawrencetown till cover (LT) in white lines from Stea and Kennedy (1998). The black arrow denotes the last movement of ice across the study area. The black rectangle shows the location of wave-cut terraces and Figure 6.6.

Figure 6.5 highlights two distinct morphological characteristics of the North Mountain in this region. The terrain in the western region is characterized by rough topography with abrupt ridges and narrowly incised valleys, whereas the eastern region of the study area is characterized by smooth topography with broadly incised valleys. This reflects differences in glacial history; areas to the west consist of glacially scoured bedrock with a thin till veneer, and to the east of a thicker blanket of Lawrencetown Till (LT); (Stea and Kennedy, 1998). The two previously unidentified glacial landforms described in chapter 5 in the valley floor are clearly visible on the PCA composite image (Figure 6.5). These of oval-shaped landforms have long axes trending ca. 335^o and the set of streamlined landforms have their long axis trending ca. 310^o (chapter 5, Webster et al., in preparation). The boundary between these landforms corresponds with the difference in terrain roughness of the North and South Mountains and the distribution of the till blanket (Figure 6.5). These observations are indicative of the glacial ice dynamics in the region (black arrow, Figure 6.5).

6.4. EXTRACTION OF WAVE-CUT TERRACES

In previous chapters (4 and 5), examples have been presented that show how a “bald earth” LIDAR DEM can be used to discover new meso-scale (ca. 1 km) landforms, improve the resolution of bedrock mapping, and examine surface processes. Raised beaches and deltas dated at 14 to 12 ka occur along the flanks of the bay (Stea and Mott, 1998). The relative sea level (RSL) history of the region is complicated and varies spatially along the Bay of Fundy. The RSL curve reported for the upper Bay of Fundy region by Amos and Zaitlin (1985) has RSL at approximately 40 m above present at 14 ka, followed by a decline to -30 m at 7 ka, then increasing to present levels. Postglacial isostatic adjustments in the form subsidence in the region are ongoing (Grant, 1980).

New results of elevations extracted from the LIDAR DEM of several existing and newly discovered wave-cut terraces along the coast are presented and are compared to previous measurements of Stea and Kennedy (1998).

6.4.1. METHODS

Several new wave-cut terraces have been identified on the LIDAR DEM along the coast in the glacial till blanket area. Surface profiles are extracted from the LIDAR DEM and are compared to previously published elevations by Stea and Kennedy (1998). It is evident that the ability of high-resolution LIDAR to obtain precise elevations of these terraces can lead to an improved understanding of the complex sea level history of this area.

6.4.2. RESULTS

Existing and new wave-cut terraces in the till have been identified along the Bay of Fundy in this study (Figures 6.5, 6.6). The terraces identified on the LIDAR DEM correspond to elevations near 5, 10, 15, 23, 25, and 35 m above MSL (Figure 6.6, B, C, D). The terraces at levels 15, 23, and 35 m are more pronounced than those near 5, 10 and 25 m. The terraces appear to be better preserved in the eastern profiles (Figure 6.6, D) compared to the western profiles (Figure 6.6, B) in this section of the coast (Figure 6.6).

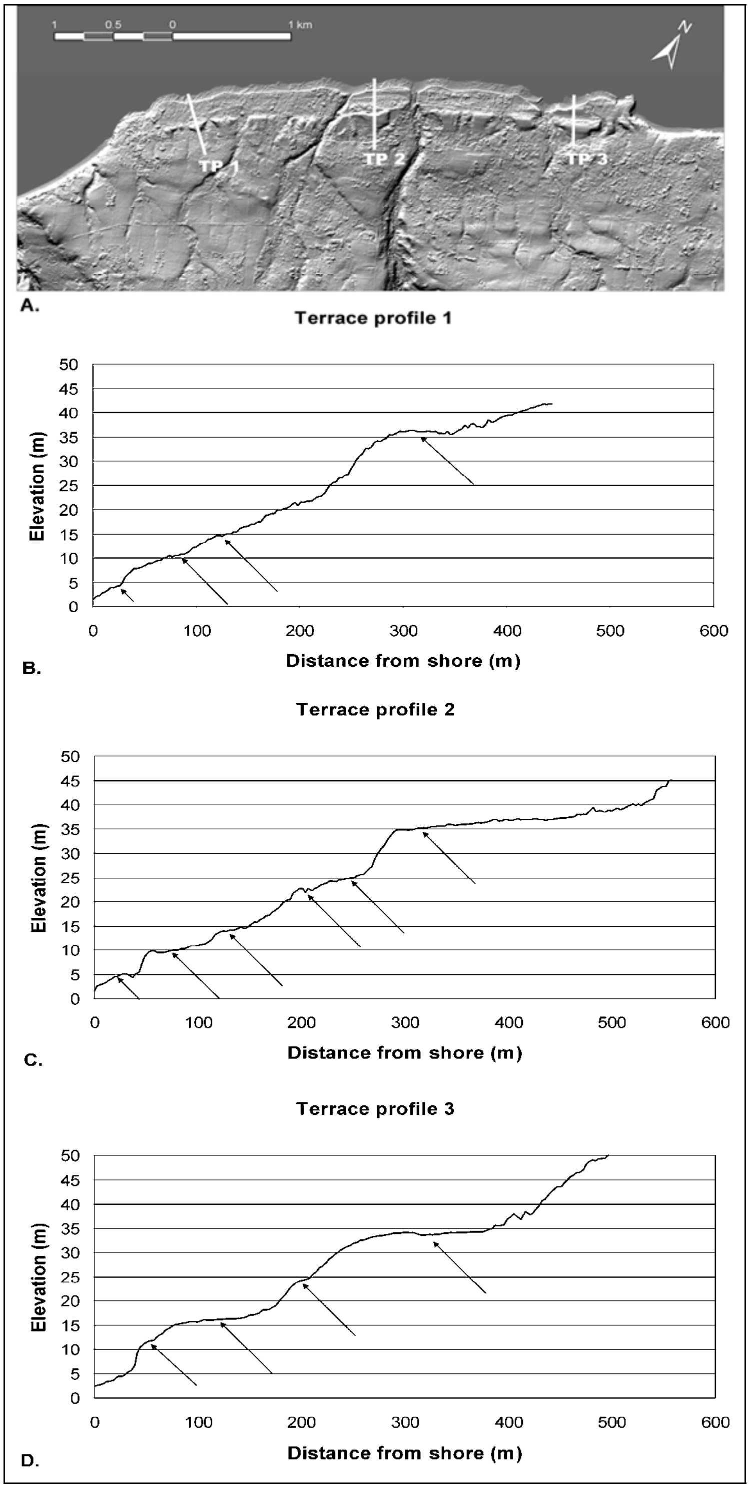

Figure 6.6 Wave-cut terraces along the Bay of Fundy. (A) Grey scale shaded relief map of the LIDAR DEM with surface profile locations (TP 1, 2, 3). (B-D) Terrace profiles with arrows denoting possible terrace locations.

6.5. DISCUSSION

This study has demonstrated that the enhanced precision and resolution of LIDAR, compared to traditional DEMs, can result in considerable changes in the re-interpretation of bedrock geology and surface processes and may lead to discoveries of previously unidentified landforms. The results indicate the LIDAR-derived DEMs are more accurate than photogrammetric derived DEMs of similar cell size (Figure 6.1). Validation was required in order to characterize the error associated with the LIDAR DEMs, especially in forested regions. The results of the LIDAR validation in open areas are similar to those reported in other studies (Huising and Gomes Pereira, 1998; Ahokas et al., 2003; Artuso et al., 2003; Hopkinson et al., 2005). The LIDAR DEM is not as accurate under the forest canopy in areas of dense shrubs as indicated by the crater validation survey (chapters 2 and 3). The DEM error under the forest canopy is –0.12 m ± 0.34 m (1σ) is slightly higher than that report by Hopkinson et al. (2005) which was 0.11 m ± 0.16 m (1σ) for ground elevations under tall shrubs (2 – 5 m), but closer to the error reported by Hodgson and Bresnhan (2005) from 0.06 m ± 0.23 m (1σ).

The highest error found in the DEM of this study was associated with vegetation overhanging the streambed that had been incorrectly classified as 'ground' points (Figures 6.4 and 6.5). When these points are removed from the analysis, the results are similar to those of the previous studies. Accurate classification of the LIDAR point cloud into 'ground' and 'non-ground' points is important for accurate geomorphic analysis. LIDAR data must be critically examined to check for such classification errors. The combination of the two validation techniques, comparing checkpoints to proximal

LIDAR ‘ground’ points and to the DEM, can facilitate the identification of these problems (Webster, in press). However, as it is very time consuming to acquire sub-decimetre level precision height measurements under the forest canopy, it is difficult to constrain this error spatially. The results indicate that the uncertainty of the LIDAR DEM is dependent on the height of the dense canopy layer. This suggests that LIDAR surveys should be conducted during leaf-off conditions to ensure minimum deciduous leaf cover. Of the leaf-off periods available for this region, spring has the added benefit of reduced shrub and under story height as a result of flattening by the winter snow pack.

Principal component analysis (PCA) provides a method where all geological features regardless of orientation can be highlighted on a single map (Figure 6.5). Although complex to interpret, this overcomes the bias of traditional shaded relief maps that only highlight topographic features that trend perpendicular to the illumination direction. The results of this study are consistent with those of Paganelli et al. (2003) who concluded that the PCA of RADARSAT-1 imagery provided an excellent base for structural mapping.

Terraces in the study area at levels of 18, 24, and 42 m above mean sea level (MSL) and interpreted to be associated with the higher sea levels at 12 to 14 ka (Stea and Mott, 1998). These levels are not in direct agreement with the terraces extracted from the LIDAR, that occur at levels 15, 23, and 35 m MSL and a less pronounced set near 5, 10 and 25 m MSL. The additional terrace levels resolved with the high-resolution LIDAR can add to our understanding of the episodic nature of RSL and isostatic adjustments within the region. The variation in terrace heights along the coast suggests that areas to the west may have rebounded more quickly than in the east, consistent with the deglaciation history of the area, where ice left the western region earlier than in the east (Stea and Mott, 1998). The ability of LIDAR to quantify these terrace levels and trace them over large distances can provide more precise constraints on interpretations of the past sea level history of the area.

6.6. CONCLUSIONS OF THIS THESIS

The conclusions of this thesis are grouped into four main themes regarding their contribution to knowledge: (1) optimization of LIDAR survey planning, accuracy assessment, and error characterization; (2) the assessment of high-resolution LIDAR to resolve subtle geological features; (3) anthropogenic affects to landscape drainage and their treatment with the LIDAR DEM; and (4) the application of LIDAR to analyze basins at a sufficiently small scale.

6.6.1. LIDAR SURVEY PLANNING, ACCURACY ASSESSMENT AND ERROR CHARACTERIZATION

When planning a LIDAR survey, familiarity with the terrain and land cover characteristics of the study area is necessary in order to select the most appropriate LIDAR system. In the case of single return systems, a first return only system is suitable for areas of sparse vegetation; whereas a last return system is more appropriate for densely vegetated areas. Beam divergence influences the strength of the returning signal. The higher the laser pulse repetition rate, the more total points there are, thus more points will make it to the ground, although this will increase the LIDAR data volume and processing time.

Geoscience applications are considerably enhanced by the ability of the laser pulses of high-resolution LIDAR to penetrate the forest canopy and measure the ground with high-precision and high spot density. Proper LIDAR sensor calibration procedures must be employed in order to remove systematic errors in raw data. This study demonstrates that insufficient calibration procedures resulted in a range bias, manifested as height differences between flight lines for one of the LIDAR acquisition methods. With a properly calibrated LIDAR system, accurate classification of the LIDAR point cloud into ‘ground’ and ‘non-ground’ points is important for detailed geomorphic analysis. Problems of misclassification were demonstrated with the raised roadbed and vegetation cover near the ground. Independent high precision validation data were collected in order to check the vertical accuracy of the LIDAR data in open and forested areas. The use of GIS and automated validation procedures allow for a voluminous amount of data to be processed that is the case for wide-area studies that are required for geomorphic investigations.

The selection of the season to conduct the survey is important for vegetated terrain and depends on the local climate. The detection of the ground with leaf-on conditions and dense shrub and ground vegetation are problems for LIDAR systems. Validation studies demonstrated the problem of shrub vegetation and overhanging tree cover representing ground elevations under the forest canopy and the stream longitudinal profile. Leaf-off conditions are desirable if a “bald-earth” DEM is to be constructed from the LIDAR data. Winter acquisition presents the problem of variable snow depths due to drifting. Thus the spring and fall time periods present the best alternatives in this region. Of these periods, the spring has the added benefit of reduced shrub and under-story vegetation height as a result of flattening by the winter snow pack.

6.6.2. HIGH-RESOLUTION LIDAR TO RESOLVE SUBTLE GEOLOGICAL FEATURES

The LIDAR-derived “bald earth” DEM was used to map flow units and ring structures in volcanic terrains and two sets of surficial landforms that have previously been obscured on aerial photography by vegetation cover or by the limited accuracy and resolution of conventional DEMs.

Contacts between the flow units interpreted from the LIDAR DEM occur within corridors constrained by field mapping in the vicinity of those contacts. A sensitivity analysis using LIDAR and traditional DEMs derived from photogrammetry of variable resolution across three contact locations indicated that only the LIDAR DEM had the precision to accurately quantify the relief of the UFU-MFU contact. If this technology can accurately constrain geologic contacts between lithologically similar map units that are shallowly dipping, then it may be widely applicable to terrains with more variable bedrock geology with more steeply dipping contacts.

A sequence of ring structures was identified on the LIDAR DEM in the Lower Flow Unit (LFU) of the North Mountain are interpreted to be a result of the interaction between the lava and either surface or shallow ground water. These structures are similar in scale and morphology to structures observed in the Columbia River Basalt (CRB) (McKee and

Stradling 1970; Hodges 1978). As LIDAR technology becomes more available, more ring structures in basaltic flows may be identified (see McKee and Stradling 1970).

Two new sets of glacial landforms were identified using the LIDAR DEM. The streamlined landforms in the valley relate to the till blanket deposits on the South Mountain and North Mountain mapped by Stea and Kennedy (1998) and provide evidence for the last movement of ice to affect the area. Several additional wave-cut terraces evident on the LIDAR DEM assist in understanding the regional sea-level history and isostasy of the area.

6.6.3. ANTHROPOGENIC AFFECTS TO LANDSCAPE DRAINAGE AND THEIR TREATMENT WITH THE LIDAR DEM

When dealing with high-resolution elevation data such as LIDAR, anthropogenic influences have to be dealt with to ensure accurate drainage metrics are derived from the DEM. Such factors not normally considered when utilizing traditional DEMs. In this study, inspection of the drainage basin boundaries and stream longitudinal profiles indicate that most catchments had “sinks”. Many of these “sinks” were adjacent to the raised elevations of a roadbed captured by the high-resolution of the LIDAR DEM. A “notch” was artificially cut across the roadbed and assigned an elevation of the nearest downstream cell. This operation improves the accuracy of the flow direction algorithm and prevents excessive erroneous sink-filling operations when deriving catchments and stream profiles from the DEM. These modifications to the DEM allow the stream to “pass through the roadbed” and the generation of a more accurate flow direction and flow accumulation grid and basin boundary.

6.6.4. APPLICATION OF LIDAR TO ANALYZE BASINS AT A SMALL SCALE

Many factors affect a stream’s ability to incise the bedrock but are difficult to separate and quantify because of the scale and resolution of traditional elevation and geological data. The high-resolution of LIDAR and the ability to provide detailed ground elevation measurements in forested areas allow drainage basins to be analyzed at scales sufficient to separate factors controlling stream incision. This study demonstrates that bedrock lithology has a significant influence on the stream’s ability to erode the bed and incise the terrain. Flow units within a basalt formation have been mapped and related to stream incision depth. The high concentration of vesicles and amygdules of the thin flows has lowered the middle flow unit’s ability to resist erosion from abrasion compared to the UFU and LFU as demonstrated in the shatterbox experiments. The UFU, like the LFU, is resistant to abrasion. The fractures associated with the UFU appear to be sealed by secondary minerals formed by the circulation of hydrothermal fluids. In general the incision depths are the lowest for the UFU, which acts as a cap rock and prevents the development and migration of knick zones within the MFU. Where the UFU outcrops on the coast, the bedrock platform is gently sloping and few knick zones are observed upstream. Where the UFU has been eroded and the MFU is exposed at or near base level, sea cliffs are present and knick zones are prevalent up stream.

REFERENCES

Abdalati, W., and Krabill, W.B. 1999. Calculation of ice velocities in the Jakobshavn Isbrae area using airborne laser altimetry. Remote Sensing of the Environment, **67**: 194-204.

Ackermann, R.V., Schlische, R.W., and Olsen, P.E. 1995. Syn-sedimentary collapse of portions of the lower Blomidon Formation, Fundy rift basin, Nova Scotia, Canada. Canadian Journal of Earth Science, **32**: 1965-1976.

Ahokas, E., Kaartinen, H., Hyyppa, J. 2003. A Quality Assessment of Airborne Laser Scanner Data. *In* 3-D reconstruction from airborne laserscanner and InSAR data. *Edited by* H.-G. Maas, G. Vosselman, G. and A. Streilein. Institute of Photogrammetry and Remote Sensing, GITC, The Netherlands, pp. 1-7.

Amos, C.L. and Zaitlin, B.A. 1985. The Effect of Changes in Tidal Range on a Sublittoral Macrotidal Sequence, Bay of Fundy, Canada. Geo-Marine Letters, **4**: 161-169.

Anhert, F. 1970. Functional Relationships between Denudation, Relief, and Uplift in Large Mid-latitude Drainage Basins. American Journal of Science, **268**: 243-263.

Artuso, R., Bovet, S., Streilen, A. 2003. Practical methods for the verification of Countrywide Terrain and Surface Models. *In* 3-D reconstruction from airborne laserscanner and InSAR data. *Edited by* H.-G. Maas, G. Vosselman, G. and A. Streilein. Institute of Photogrammetry and Remote Sensing, GITC, The Netherlands, pp. 14-19.

Baroni, C., Noti, V., Ciccacci, S., Righini, G. and Salvatore, M.C. 2005. Fluvial origin of the valley system in northern Victoria land (Antarctica) from quantitative geomorphic analysis. Geological Society of America Bulletin, **117**, no. ½: 212-228.

Belt, K. and Paxton, S.T. 2005. GIS as an aid to visualizing and mapping geology and rock properties in regions of subtle topography. Geological Society of America Bulletin, **117**, no. ½: 149-160.

Bretar, F., Pierrot-Deseilligny, M., Roux, M. 2003. Estimating intrinsic accuracy of airborne laser data with local 3-D-Offsets. *In* 3-D reconstruction from airborne laserscanner and InSAR data. *Edited by* H.-G. Maas, G. Vosselman, G. and A. Streilein. Institute of Photogrammetry and Remote Sensing, GITC, The Netherlands, pp. 20-26.

Brock, J.C., Wright, C.W., Sallenger, A.H., Krabill, W.B., Swift, R.N. 2002. Basis and methods of NASA airborne topographic mapper LIDAR surveys for coastal studies. Journal of Coastal Research, **18**: 1-13.

Brocklehurst, S.H. and Whipple, K.X. 2002. Glacial erosion and relief production in the Eastern Sierra Nevada, California. Geomorphology, **42**: 1-24.

Brocklehurst, S.H. and Whipple, K.X. 2004. Hypsometry of Glaciated Landscapes. Earth Surface Processes and Landforms, **29**: 907-926.

Brown, D., and Bara, T. 1994. Recognition and Reduction of Systematic Error in Elevation and Derivative Surfaces from 7 ½-Minute DEMs. Photogrammetric Engineering and Remote Sensing, **60**: 189-194.

Burman, H. 2000. Adjustment of laser scanner data for correction of orientation errors. International Archives of Photogrammetry and Remote Sensing, **33**, no. 3/1: 125-132.

Comeau, R.L. 1978. Uranium, North Kingston, Kings County, Nova Scotia, Getty Mineral Company, Limited. Nova Scotia Department of Natural Resources, Halifax, N.S. Assessment Report 21H/02B 54-K20(1).

Costa-Cabral, M.C. and Burges, S.J. 1994. Digital Elevation Model Networks (DEMON): A model of flow over hill slopes for computation of contributing and dispersal areas. Water Resource Research, **30**, no. 6: 1681-1692.

Charlton, M.E., Large, A.R., and Fuller, I.C. 2003. Application of airborne LIDAR in River Environments: The River Coquet, Northumberland, UK. Earth Surface Processes and Landforms, **28**: 299-306.

Crombaghs, M., Bruelgelmann, R., de Min., E.J. 2000. On the adjustment of overlapping strips of laser altimeter height data. International Archives of Photogrammetric Engineering and Remote Sensing, **33**, no. B3/1: 230-237.

Crowe, B.M., and Fisher, R.V. 1973. Sedimentary structures in base-surge deposits with special reference to cross bedding, Ubehebe Crater, Death Valley, California. Geological Society of America Bulletin, **84**: 663-682.

Dietrich, W.E., Bellugi, D.G., Sklar, L.S., Stock, J.D., Heimsath, A.M., and Roering, J.J. 2003. Geomorphic Transport Laws for Predicting Landscape Form and Dynamics. *In* Prediction in Geomorphology. Geophysical Monograph 135, pp. 1-30.

Dostal, J., and Dupuy, C. 1984. Geochemistry of the North Mountain Basalts (Nova Scotia, Canada). Chemical Geology, **45**: 245-261.

Dostal, J., and Greenough, J.D. 1992. Geochemistry and petrogenesis of the early Mesozoic North Mountain basalts of Nova Scotia, Canada. *In* Eastern North American Mesozoic Magmatism. *Edited by* J.H. Puffer and P.C. Ragland. Geological Society of America Special Paper 268. pp. 149-159.

Elberink, S.O., Brand, G., Brugelmann, R. 2003. Quality Improvement of Laser Altimetry DEM’s. *In* 3-D reconstruction from airborne laserscanner and InSAR data. *Edited by* H.-G. Maas, G. Vosselman, G. and A. Streilein. Institute of Photogrammetry and Remote Sensing, GITC, The Netherlands, pp. 51-58.

Environment Canada web site. HTTP://WWW.CLIMATE.WEATHEROFFICE.CA/CLIMATE_NORMALS/RESULTS_E.HTML [cited 10 may 2005].

Fagents, S.A., Lanagan, P., and Greeley, R. 2002. Rootless cones on Mars: a consequence of lava-ground ice interaction. *In* Volcano-Ice Interactions on Earth and Mars. *Edited by* J.L. Smellie and M.G. Chapman. Geological Society, London, Special Publication, 202. pp. 295-317.

Fanning, D. 2004. Personal communications. Jacques Whitford and Associates Limited, unpublished proprietary well yield data.

Filin, S. 2001. Recovery of Systematic Biases in Laser Altimeters Using Natural Surfaces. *In* Proceedings of the International Society of Photogrammetry and Remote Sensing workshop, Annapolis Maryland. International Archives of Photogrammetry, Remote Sensing and Spatial Information Sciences, Volume XXXIV-3/W4, pp.85-91.

Filin, S. 2003*a*. Analysis and implementation of a laser strip adjustment model. *In* 3-D reconstruction from airborne laserscanner and InSAR data. *Edited by* H.-G. Maas, G. Vosselman, G. and A. Streilein. Institute of Photogrammetry and Remote Sensing, GITC, The Netherlands, pp. 65-70.

Filin, S. 2003*b*. Recovery of Systematic Biases in Laser Altimetry Data Using Natural Surfaces. Photogrammetric Engineering & Remote Sensing, **69**, no. 11: 1235-1242.

Finlayson, D.P. and Montgomery, D.R. 2003. Modeling large-scale fluvial erosion in geographic information systems. Geomorphology. **53**: 147-164.

Flood, M. and Gutelius, B. 1997. Commercial implications of Topographic Terrain Mapping Using Scanning Airborne Laser Radar. Photogrammetric Engineering and Remote Sensing, **4**: 327-366.

Goa, J. 1997. Resolution and accuracy of terrain representation by grid DEMs at micro scale. International Journal of Geographical Information Science, **11**, no. 2: 199-212.

Gomes Pereira, L.M. and Wicherson, R. J. 1999. Suitability of laser data for deriving geographic information - a case study in the context of management of fluvial zones. International Journal of Photogrammetry and Remote Sensing, **54**, no. 2-3: 105-114.

Grant, D.R. 1980. Quaternary sea-level change in Atlantic Canada as an indication of crustal delevlling. *In* Morner, N.A. ed. Earth Rheology, Isostasy and Eustacy. John Wiley and Sons, London.

Grist, A.M., and Zentilli, M. 2003. Post-Paleocene cooling in the southern Canadian Atlantic region: evidence from apatite fission track models. Canadian Journal of Earth Sciences, **40**, no. 9: 1279-1297.

Greeley, R., and Fragents, S.A. 2001. Icelandic pseudo-craters as analogs to some volcanic cones on Mars. Journal of Geophysical Research, **106**: 20527-20546.

Greenough, J.D. 1995. Mesozoic rocks. *In* Geology of the Appalachian-Caledonian Orogen in Canada and Greenland, *Edited by* H. Williams. Geological Survey of Canada, Geology of Canada, no. 6. pp. 567-600 (also Geological Society of America, The Geology of North America, v. F-1).

Greenough, J.D., and Dostal, J. 1992. Cooling history and differentiation of a thick North Mountain Basalt flow (Nova Scotia, Canada). Bulletin of Volcanology, **55**: 63-73.

Greenough, J.D., Jones, L.M., and Mossman, D.J. 1989. Petrochemical and stratigraphic aspects of North Mountain basalt from the north shore of the Bay of Fundy, Nova Scotia, Canada. Canadian Journal of Earth Sciences, **26**: 2710-2717.

Hallet, B., Hunter, L. and Bogen, J. 1996. Rates of Erosion and sediment evacuation by glaciers: A review of field data and their implications. Global and Planetary Change, **12**: 213-235.

Haan, C.T., Barfield, B.J., and Hayes, J.C. 1994. Design Hydrology and Sedimentology for Small Catchments. Academic Press.

Harding, D.L., and Berghoff, G.S. 2000. Fault scarp detection beneath dense vegetation cover: Airborne lidar mapping of the Seatle fault zone, Bainbridge Island, Washington State. *In* Proceedings of the American Society of Photogrammetry and Remote Sensing Annual Conference, Washington, D.C., pp. 9.

Haugerud, R.A., Harding, D.J., Johnson, S.Y., Harless, J.L., Weaver, C.S., and Sherrod, B.L. 2003. High-resolution lidar topography of the Puget Lowland-A bonanza for earth science. Geological Society of America Today, **13**, no. 6: 4-10.

Hem, J. 1985. Study and Interpretation of the Chemical Characteristics of Natural Water. United States Geological Survey Water-Supply Paper 2254. pp. 225.

Hodgson, M.E., Bresnahan, P. 2004. Accuracy of airborne lidar-derived elevation: empirical assessment and error budget. Photogrammetric Engineering and Remote Sensing, **70**, no. 3: 331-339.

Hodgson, M.E., Jensen, J.R., Schmidt, L., Shill, S., Davis, B. 2003. An evaluation of LIDAR and IFSAR derived digital elevation models in leaf-on conditions with USGS Level 1 and Level 2 DEMs. Remote Sensing of the Environment, **84**, no. 2: 295-308.

Hodgson, M.E., Jensen, J., Raber, G., Tullis, J., Davis, B.A., Thompson, G., Schuckman, K. 2005. An evaluation of lidar-derived elevation and terrain slope in leaf-off conditions. Photogrammetric Engineering and Remote Sensing, **71**, no. 7: 817-823.

Hodges, C.A. 1978. Basaltic Ring structures of the Columbia Plateau. Geological Society of America Bulletin, **89**: 1281-1289.

Hodych, J. P., and Dunning, G.R. 1992. Did the Manicouagan impact trigger end-of-Triassic mass extinction? Geology, **20**: 51-54.

Hooper, P.R. 1997. The Columbia River Basalt Province: Current Status. *In* Large Igneous Provinces: Continental, Oceanic, and Planetary Flood Volcanism. Geophysical Monograph 100. pp. 1-34.

Hopkinson, C., Chasmer, L.E., Sass, G., Creed, I.F., Sitar, M., Kalbfleisch, W., Treitz, P. 2005. Vegetation class dependent errors in lidar ground elevation and canopy height estimates in a boreal wetland environment. Canadian Journal of Remote Sensing, **31**, no. 2: 191-206.

Hudgins, A.D. 1960. The Geology of the North Mountain in the map area, Baxters Harbour to Victoria Beach. M.Sc. thesis, Department of Geology, Acadia University, Wolfville, N.S.

Huising, E.J., Gomes Pereira, L.M. 1998. Errors and accuracy estimates of laser data acquired by various laser scanning systems for topographic applications. International Journal of Photogrammetric Engineering and Remote Sensing, **53**, no. 5: 245-261.

Jenson, S.K., and Dominque, J.O. 1988. Extracting Topographic Structure from Digital Elevation Data for Geographic Information Systems Analysis. Photogrammetric Engineering and Remote Sensing, **54**, no. 11: 1593-1600.

Jones, L.M., and Mossman, D.J. 1988. The isoptopic composition of strontium of the Early Jurassic North Mountain Basalts, Nova Scotia. Canadian Journal of Earth Sciences, **26**: 2710-2717.

Katzenbeisser, R. 2003. On the calibration of LIDAR sensors *In* 3-D reconstruction from airborne laserscanner and InSAR data. *Edited by* H.-G. Maas, G. Vosselman, G. and A. Streilein. Institute of Photogrammetry and Remote Sensing, GITC, The Netherlands, pp. 59-64.

Keppie, J.D. 2000. Geological Map of the Province of Nova Scotia. Nova Scotia Department of Natural Resources Minerals and Energy Branch, Halifax, N.S. Map ME 2000-1.

Kilian, J., Haala, N., Englich, M. 1996. Capture and evaluation of airborne laser scanner data. International Archives of Photogrammetric Engineering and Remote Sensing, **31**, no. B3: 383-388.

Kirby, E. and Whipple, K. 2001. Quantifying differential rock-uplift rates via stream profile analysis. Geology, **29**, no. 5: 415-418.

Kirkbride, M. and Matthews, D. 1997. The Role of Fluvial and Glacial Erosion in Landscape Evolution: The Ben Ohau Range, New Zealand. Earth Surface Processes and Landforms. **22**: 317-327.

Kienzle, S. 2004. The effect of DEM raster resolution on first order, second order and compound terrain derivatives. Transactions in GIS, **8**, no. 1: 83-111.

Klein, G.D. 1962. Triassic Sedimentation, Maritime Provinces, Canada. Geological Society of America Bulletin, **73**: 1127-1146.

Kontak, D.J. 1999. Nature of Zeolite Distribution in the North Mountain Basalt, Southern Nova Scotia: Field and Geochemical Studies. Nova Scotia Department of Nature

Resources, Halifax, N.S. Minerals and Energy Branch Report of Activities 1999, pp. 105-123.

Kontak, D.J. 2001. Internal stratigraphy of the Jurassic North Mountain Basalt, Southern Nova Scotia. Nova Scotia Department of Nature Resources, Halifax, N.S. Minerals and Energy Branch Report of Activities 2001, pp. 69-79.

Kontak, D.J., DeYoung, M.Y., and Dostal, Y. 2002. Late-stage Crystallization History of the Jurassic North Mountain Basalt, Nova Scotia, Canada. Textural and Chemical Evidence for pervasive development of silicate-liquid immiscibility. The Canadian Minerologist, **40**: 1287-1311.

Kooi, H. and Beaumont, C. 1996. Large-scale geomorphologt: classical concepts reconciled and integrated with contemporary ideas via a surface-process model. Journal of Geophysical Research, **101**: 3361-3386.

Kornus, W., Ruiz, A., 2003. Strip Adjustment of LIDAR data. *In* 3-D reconstruction from airborne laserscanner and InSAR data. *Edited by* H.-G. Maas, G. Vosselman, G. and A. Streilein. Institute of Photogrammetry and Remote Sensing, GITC, The Netherlands, pp. 47-50.

Krabill, W.B., Thomas, R.H., Martin, C.F., Swift, R.N., and Frederick, E.B. 1995. Accuracy of airborne laser altimetry over the Greenland ice sheet. International Journal of Remote Sensing, **16**: 1211-1222.

Krabill, W., Abdalati, W., Frederick, E., Manizade, S., Martin, C., Sonntag, J., Swift, R., Thomas, R., Wright, W., and Yungel, J. 2000. Greenland Ice Sheet: high-elevation balance and peripheral thinning, Science **289**: 428-430.

Kraus, K. and Pfeifer, N. 1998. Determination of terrain models in wooded areas with airborne laser scanner data, ISPRS Journal of Photogrammetry and Remote Sensing, **53**, no. 4, 193-203.

Lanagan, P.D., McEwen, A.S., Keszthelyi, L.P., and Thordarson, T. 2001. Rootless cones on Mars indicating the presence of shallow equatorial ground ice in recent times. Geophysical Research Letters, **28**, no. 12: 2365-2368.

Latypov, D., Zosse, E. 2002. LIDAR data quality control and system calibration using overlapping flight lines in commercial environment. *In* Proceedings of the American Society of Photogrammetry and Remote Sensing Annual Conference, Washington, D.C., pp 13.

Lewis, C.F.M., Taylor, B.B., Stea, R.R., Fader, G.B.J., Horne, R.J., MacNeill, S.G. and Moore, J.G. 1998. Earth Science and Engineering: Urban Development in the

Metropolitan Halifax Region. *In* Urban Geology of Canadian Cities. *Edited by* P.F. Karrow and O.L. White, O.L. Geological Association of Canada Special Paper 42. pp. 409-444.

Li, Y., Liu, G. and Cui, Z. 2001. Glacial valley cross-profile morphology, Tian Shan Mountains, China. Geomorphology, **38**: 153-166.

Maas, H.G. 2000. Least-Squares Matching with Airborne Laserscanning Data in a TIN Structure. International Archives of Photogrammetric Engineering and Remote Sensing, **33**, no. B3/1: 548-555.

Maas, H.G. 2002. Methods for Measuring Height and Planimetry Discrepancies in Airborne Laserscanner Data. Photogrammetric Engineering and Remote Sensing, **68**, no. 9: 933-940.

MacDonald, M. A. and Ham, J.A. 1994. Geological Map of Bridgetown, South Mountain Batholith Project. Nova Scotia Department of Natural Resources, Halifax N.S. Map 94-08.

Macdougall, J.D. 1988. Continental Flood Basalts and MORB: A Brief Discussion of Similarities and Differences in their Petrogenesis. *In* Continental Flood Basalts, *Edited By* J.D. Macdougall. Kluwer Academic Publishers, pp. 331-341.

MacGregor, K.R., Anderson, R.S., Anderson, S.P. and Waddington, E.D. 2000. Numerical simulations of glacial-valley longitudinal profile evolution. Geology, **28**, no. 11: 1031-1034.

Maclean, G.A., and Krabill, W.B. 1986. Gross-merchantable timber volume estimation using an airborne LIDAR system. Canadian Journal of Remote Sensing, **12**: 7-18.

Martin, B.S. 1989. The Roza Member, Columbia River Basalt Group; Chemical stratigraphy and flow distribution. *In* Volcanism and tectonism in the Columbia River flood-basalt province: Boulder Colorado. *Edited by* S.P. Reidel and P.R. Hooper. Geological Society of America Special Paper 239. pp.85-104.

Marzoli, A., Renne, P.R. Piccirillo, E.M., Ernesto, M., Bellieni, G., and De Min, A. 1999. Extensive 200-million-year-old continental flood basalts of the Central Atlantic Magmatic Province. Science, **284**: 616-618.

Mather, A.E., Stokes, M., and Griffiths, J.S. 2002. Quaternary Landscape Evolution: A Framework for understanding contemporary erosion, southeast Spain. Land Degradation & Development, **13**: 89-109.

Maune, D. F. 2001. Digital Elevation Model Technologies and Applications: The DEM Users Manual. *Edited by* D.F. Maune, American Society of Photogrammetry and Remote Sensing. pp. 1-250.

McKean, J., and Roering, J. 2003. Objective landslide detection and surface morphology mapping using high-resolution airborne laser altimetry. Geomorphology, **1412**: 1-21.

McKee, B., and Stradling, D. 1970. The Sag Flowout: A Newly Described Volcanic Structure. Geological Society of America Bulletin, **27**: 2035-2044.

Mertz, K.A., and Hubert, J.F. 1990. Cycles of sand-flat sandstone and playa-lacustrine mudstone in the Triassic-Jurassic Blomidon redbeds, Fundy rift basin, Nova Scotia: implications for tectonic and climate controls. Canadian Journal of Earth Science, **27**: 442-451.

Montgomery, D.R. 2002. Valley formation by fluvial and glacial erosion. Geology, **30**, no. 11: 1047-1050.

Montgomery, D.R., and Lopez-Blanco, J. 2003. Post-Oligocene river incision, southern Sierra Madre Occidental, Mexico. Geomorphology, **55**: 235-247.

Nadon, G.C., and Middleton, G.V. 1985. The stratigraphy and sedimentology of the Fundy Group (Triassic) of the St. Martins area, New Brunswick. Canadian Journal of Earth Science, **22**: 1183-1203.

Nova Scotia's Geographic Information Standards. Available from HTTP://WWW.GOV.NS.CA/SNSMR/LAND/PROGRAMS/POST/MANUAL/DEFAULT.ASP [cited September, 2003].

Olsen, P. E., and Schlische, R.W. 1990. Transtensional arm of the early Mesozoic Fundy rift basin: Penecontemporaneous faulting and sedimentation. Geology, **18**: 695-698.

O'Reilly, C. 2000. Defining the coastal zone from a hydrographic perspective. Proceedings, Workshop on risk assessment and disaster mitigation: Enhanced use of risk management in integrated coastal management. International Ocean Institute, Bermuda. Backscatter, April 2000: 20-24.

Paganelli, F., Grunsky, E.C., Richards, J.P., and Pryde, R. 2003. Use of RADARSAT-1 principal component imagery for structural mapping. A case study in the Buffalo Head Hills, northern central Alberta, Canada. Canadian Journal of Remote Sensing, **29**, no. 1: 111-140.

Papezik, V.S., Greenough, J.D., Colwell, J.A., and Mallinson, T.J. 1988. North Mountain basalt from Digby, Nova Scotia: models for a fissure eruption from stratigraphiy and petrochemistry. Canadian Journal of Earth Sciences, **25**: 74-83.

Pazzaglia, F.J. Gardner, T.W. and Merritts, D.J. 1998. Bedrock Fluvial Incision and Longitudinal Profile Development Over Geological Time Scales Determined by Fluvial

Terraces. *In* Rivers over rock: fluvial processes in Bedrock channels. *Edited by* K.J. Tinkler, K.J. and E.E. Wohl. Geophysical monograph 107. pp.207-235.

Pazzaglia, F.J. 2003. Landscape evolution models. Developments in Quaternary Science. Vol. 1. pp. 247-274.

Pe-Piper, G. 2000. Mode of occurrence, chemical variation and genesis of Mordenite and associated zeolites from the Morden area, Nova Scotia, Canada. The Canadian Mineralogist, **38**: 1215-1232.

Pe-Piper, G., and Miller, L. 2002. Zeolite minerals from the North Shore of Minas Basin, Nova Scotia. Atlantic Geology, **38**: 11-28.

Pe-Piper, G., Jansa, L.F., and Lambert Richard, St. J. 1992. Early Mesozoic magmatism on the eastern Canadian margin: Petrogenetic and tectonic significance. *In* Eastern North American Mesozoic Magmatism, *Edited by* J.H. Puffer and P.C. Ragland, Geological Society of America Special Paper 268. pp. 13-36.

Randall, A.D., Fancis, R.M., Frimpter, M.H., and Emery, J.M. 1988. Region 19, Northeastern Appalachians. *In* The Geology of North America Vol. O-2 Hydrology. *Edited by* W. Back, J.S. Rosenshein, and Seaber P.R., The Geological Society of America. Boulder, Colorado, pp. 177-187.

Reneau, S.L. 2000. Stream Incision and terrace development in Frijoles Canyon, Bandelier National Monument, New Mexico, and the influence of lithology and climate. Geomorphology, **32**: 171-193.

Ritchie, L.C. 1995. Airborne Laser Altimeter Measurements of Landscape Topography. Remote Sensing of the Environment, **53**, no. 1: 59-79.

Rose, C. 2004. An Introduction to the Environmental Physics of Soil, Water and Watersheds. Cambridge University Press. pp. 226-258.

Sallenger, A.B., Jr., Krabill, W., Brock, J., Swift, R., Jansen, M., Manizade, S., Richmond, B., Hampton, M., Eslinger, D. 1999. Airborne laser study quantifies El Niño-induced coastal change. Eos, Transactions, American Geophysical Union, **80**: 89-92.

Schenk, T, Seo, S, Csatho, B. 2001. Accuracy study of airborne laser altimetry data. *In* Proceedings of the International Society of Photogrammetry and Remote Sensing workshop, Annapolis Maryland. International Archives of Photogrammetry, Remote Sensing and Spatial Information Sciences, Volume XXXIV-3/W4, pp.113-118.

Schlische, R.W., and Ackermann, R.V. 1995. Kinematic significance of sediment-filled fissures in the North Mountain Basalt, Fundy rift basin, Nova Scotia, Canada. Journal of Structural Geology, **17**, no. 7: 987-996.

Schoorl, J.M., Sonneveld, M.P.W., and Veldkamp, A. 2000. Three-dimensional landscape process modeling: the effect of DEM resolution. Earth Surface Processes and Landforms, **25**: 1025-1034.

Schuckman, K. 2003. Announcement of the Proposed ASPRS Binary Lidar Data File Format Standard. Photogrammetric Engineering and Remote Sensing, **69**, no. 1: 13-19.

Seidl, M.A., Dietrich, W.E., and Kirchner, J.W. 1994. Longitudinal Profile Development into Bedrock: An Analysis of Hawaiian Channels. The Journal of Geology. **102**: 457-474.

Seidl, M.A., Finkel, R.C., Caffee, Hudson, B., and Dietrich, W.E. 1997. Cosmogenic Isotope Analysis applied to River Longitudinal Profile Evolution: problems and Interpretations. Earth Surface Processes and Landforms, **22**: 195-209.

Sklar, L.S. and Dietrich, W.E. 1998. River Longitudinal Profiles and Bedrock Incision Models: Stream Power and the Influence of Sediment Supply. *In* Rivers over rock: fluvial processes in Bedrock channels. *Edited by* K.J. Tinkler and E.E. Wohl. Geophysical monograph 107. pp.237-260.

Sklar, L.S. and Dietrich, W.E. 2001. Sediment and rock strength controls on river incision into bedrock. Geology, **29**, no. 12: 1087-1090.

Snyder, N. P., Whipple, K.X., Tucker, G.E., and Merritts, D.J. 2000. Landscape response to tectonic forcing: Digital elevation model analysis of stream profiles in the Mendocino triple junction region, northern California. Geological Society of America Bulletin, **112**, no. 8: 1250-1263.

Spooner, I. S. 1998. Changes in lake-sediment stratigraphy associated with late glacial climate change: examples from western Nova Scotia. Atlantic Geology, **34**: 229-240.

Stea, R.R., Conley, H., and Brown, Y. 1992. Surficial geology of the province of Nova Scotia: Nova Scotia Department of Natural Resources, Mines and Energy Branch, Halifax, N.S. Map 92-3, 1:500,000 scale.

Stea, R.R., and Kennedy, C.M. 1998. Surficial Geology of Bridgetown (NTS sheet 21A/14). Nova Scotia Department of Natural Resources Minerals and Energy Branch, Halifax, N.S. OFM 1998-002.

Stea, R.R. and Mott, R.J. 1998. Deglaciation of Nova Scotia: Stratigraphy and Chronology of Lake Sediment Cores and Buried Organic Sections. Geographie physique et Quaternaire, **50**, no. 1: 3-21.

Stea, R.R., Piper, D.J.W, Fader, G.B.J., and Boyd, R. 1998. Wisconsinan glacial and sea-level history of Maritime Canada and the adjacent continental shelf: A correlation of land and sea events. Geological Society of America Bulletin, **110**, no. 7: 821-845.

Stevens, G. 1980. Trip 8: Mesozoic Volcanism Structure – Northern Bay of Fundy Regions, N.S. *In* Geological Association of Canada and Mineralogical Association of Canada Annual Meeting field guide, Halifax, N.S.

Stock, J.D., Montgomery, D. R, Collins, B.D., Dietrich, W.E., and Sklar, L. 2005. Field measurements on incision rates following bedrock exposure: Implications for process controls on the long profiles of valleys cut by rivers and debris flows. Geological Society of America Bulletin. **117**: 174-194.

Stock, J. and Montgomery, D. R. 1999. Geologic constraints on bedrock river incision using the stream power law. Journal of Geophysical Research, **104**, no. B3: 4983-4993.

Stockdon, H.F., Sallenger, A.H., List, J.H., Holman, R.A., 2002. Estimation of shoreline position and change using airborne topographic LIDAR data. Journal of Coastal Research, **18**, no. 3: 502-513.

Stokes, C.R. and Clark, C.D. 2001. Palaeo-ice streams. Quaternary Science Reviews. **20**: 1437-1457.

Strahler, A.N. 1952. Hypsometric (Area-Altitude) analysis of erosional topography. Geological Society of America Bulletin. **63**: 1117-1141.

Tague, C. and Grant, G.E. 2004. A geological framework for interpreting the low-flow regimes of Cascade streams, Willamette River basin, Oregon. Water resources Research, **40**: W04303.

Thorarinsson, S. 1953. The crater groups in Iceland. Bulletin of Volcanology, **14**: 3-44

Toth, C.K. 2004. Future Trends in LIDAR. *In* Proceedings of American Society of Photogrammetric Engineering and Remote Sensing Annual Conference, Washington, D.C.

Toutin, T, Rivard, B. 1995. A New Tool for Depth Perception of Multi-Source Data. Photogrammetric Engineering & Remote Sensing, **61**, no. 10: 1209-1211.

Turcotte, D. 1992. Fractals and Chaos in geology and geophysics. Cambridge Press, pp. 199.

van der Bleek, P. and Braun, J. 1998. Numerical modelling of landscape evolution on geological time-scales: a parameter analysis and comparison with south-eastern highlands of Australia. Basin research, **10**: 49-68.

Wade, J. A., Brown, D.E., Traverse, A., and Fensome, R.A. 1996. The Triassic-Jurassic Fundy Basin, eastern Canada: regional setting, stratigraphy and hydrocarbon potential. Atlantic Geology, **32**: 189-231.

Walker, J.P., and Willgoose, G.R. 1999. On the effect of digital elevation model accuracy on hydrology and geomorphology. Water Resources Research, **35**, no. 7: 2259-2268.

Wark, J.M., and Clarke, D.B. 1980. Geochemical discriminators and the palaeotectonic environment of the North Mountain basalts, Nova Scotia. Canadian Journal of Earth Sciences, **17**: 1740-1745.

Webster, T.L. in press. LIDAR validation using GIS: A case study comparison between two LIDAR collection methods. Geocarto International.

Webster, T.L., and Dias, G. in press. LIDAR validation using GIS: An automated procedure for comparing GPS and proximal LIDAR ground elevations. Computers & Geosciences.

Webster, T.L., Forbes, D.L., and Dickie, S. 2004*a*. Using topographic lidar to map flood risk from storm-surge events from Charlottetown, Prince Edward Island. Canadian Journal of Remote Sensing, **30**, no. 1: 64-76.

Webster, T.L., Christian, M., Sangster, C. and Kingston, D. 2004*b*. High-Resolution Elevation and Image Data Within the Bay of Fundy Coastal Zone, Nova Scotia, Canada. *In* GIS for Coastal Zone Management. *Edited by* Bartlett, D. and Smith, J., CRC Press. Boca Raton, Florida, pp.195-218.

Webster, T.L., Murphy, J.B., Gosse, J.C., and Spooner, I. in review. Coupling LIDAR-derived Landscape Metrics and Surface Processes: An Example from the Fundy Basin, Nova Scotia, Canada. Canadian Journal of Remote Sensing.

Webster, T.L., Murphy, J.B., and Gosse, J.C. in press. Mapping Subtle Structures with LIDAR: Flow Units and Phreomagmatic Rootless Cones in the North Mountain Basalt, Nova Scotia. Canadian Journal of Earth Sciences.

Wehr, A., and Lohr, U. 1999. Airborne laser scanning—an introduction and overview, ISPRS Journal of Photogrammetry and Remote Sensing, **54**, no. 2-3: 68-82.

Weissel, J.K. and Seidal, M. 1998. Inland Propagation of Erosional Escarpments and River Profile Evolution Across the Southeast Australian Passive Continental Margin. *In* Rivers over rock: fluvial processes in Bedrock channels. *Edited by* K.J. Tinkler and E.E. Wohl. Geophysical monograph 107. pp.189-206.

Whipple, K.X., Hancock, G.S., and Anderson, R.S. 2000*a*. River Incision into bedrock: Mechnaics and relative efficacy of plucking, abrasion, and cavitation. Geological Society of America Bulletin, **112**, no. 3: 490-503.

Whipple, K.X., Snyder, N.P., and Dollenmayer, K. 2000*b*. Rates and processes of bedrock incision by the Upper Ukak River since the 1912 Novarupta ash flow in the Valley of Ten Thousand Smokes, Alaska. Geology, **28**, no. 9: 835-838.

Whipple, K.X. and Tucker, C. E. 2002. Implications of sediment-flux-dependent river incision models for landscape evolution. Journal of Geophysical Research, **107**, no. B2: 3: 1-20.

Willgoose, G. and Hancock, G. 1998. Revisiting the Hypsometric Curve as an indicator of form and process in Transport-limited Catchment. Earth Surface Processes and Landforms, **23**: 611-623.

Winter, T.C., Harvey, J.W., Franke, O.L. and Alley, W.M. 1998. Ground Water and Surface Water A single resource. United States Geological Survey Circular 1139. 79 pp.

Withjack, M. O., Olsen, P.E., and Schlische, R.W. 1995. Tectonic evolution of the Fundy rift basin, Canada: Evidence of extension and shortening during passive margin development. Tectonics, **14**, no. 2: 390-405.

Wolock, D.M. and Price, C.V. 1994. Effects of Digital Elevation Map Scale and Data Resolution on a Topographically Based Watershed Model. Water Resources Research, **30**, no. 11: 3041-52.

Zang, X., Drake, N.A., Wainwright, J., and Mulligan, M. 1999. Comparison of Slope Estimates from Low Resolution DEMs: Scaling Issues and Fractal methods for their Solution. Earth Surface Processes and Landforms, **24**: 763-779.

Zhang, W., and Montgomery, D.R. 1994. Digital elevation model grid size, landscape representation, and hydrological simulations. Water Resources Research, **30**, no. 4: 1019-1028.

APPENDIX . 1. PERMISSION TO INCLUDE COPYRIGHT MATERIAL